IAEA-TECDOC-1409

Ion beam techniques for the analysis of light elements in thin films, including depth profiling

Final report of a co-ordinated research project
2000–2003

IAEA
International Atomic Energy Agency

October 2004

IAEA-TECDOC-1409

Ion beam techniques for the analysis of light elements in thin films, including depth profiling

Final report of a co-ordinated research project
2000–2003

IAEA
International Atomic Energy Agency

October 2004

The originating Section of this publication in the IAEA was:

Physics Section
International Atomic Energy Agency
Wagramer Strasse 5
P.O. Box 100
A-1400 Vienna, Austria

ION BEAM TECHNIQUES FOR THE ANALYSIS OF LIGHT ELEMENTS
IN THIN FILMS, INCLUDING DEPTH PROFILING

IAEA, VIENNA, 2004
IAEA-TECDOC-1409
ISBN 92–0–110404–9
ISSN 1011–4289

Printed by the IAEA in Austria
October 2004

FOREWORD

Light elements play an important role in the properties of modern materials and functional devices. These properties depend, to a large extent, on the composition and distribution of hydrides, borides, carbides, nitrides and oxides in engineered thin films or in the near-surface region of bulk materials. Enhancing the performance of these materials and functional devices requires reliable quantification of these light elements, and knowledge on how to control and manipulate them. The use of accelerator-based, nuclear techniques of analysis has contributed much to materials science, in providing valuable data and knowledge not readily accessible using other techniques of analysis.

To promote and exploit the potential of accelerator based, nuclear techniques of analysis the IAEA established in 2000 a Coordinated Research Project (CRP) on The Use of Ion Beam Techniques for the Analysis of Thin Films, Including Depth Profiling. The objective of this CRP was to develop a coordinated research effort between accelerator laboratories and materials science research groups in the IAEA Member States in order to assist and promote the development of quality assurance methods, to evaluate databases of parameters needed for quantitative analysis and to develop and apply accelerator based nuclear techniques of analysis to selected problems concerning the surface modification of materials and production of thin films.

This publication includes outputs obtained from research undertaken in contracts and agreements under this CRP. The IAEA officer responsible for this publication was N. Dytlewski of the Division of Physical and Chemical Sciences.

EDITORIAL NOTE

The papers in these proceedings are reproduced as submitted to the Publishing Section and have not undergone rigorous editorial review by the IAEA.

The views expressed do not necessarily reflect those of the IAEA, the governments of the nominating Member States or the nominating organizations.

The use of particular designations of countries or territories does not imply any judgement by the publisher, the IAEA, as to the legal status of such countries or territories, of their authorities and institutions or of the delimitation of their boundaries.

The mention of names of specific companies or products (whether or not indicated as registered) does not imply any intention to infringe proprietary rights, nor should it be construed as an endorsement or recommendation on the part of the IAEA.

The authors are responsible for having obtained the necessary permission for the IAEA to reproduce, translate or use material from sources already protected by copyrights.

CONTENTS

SUMMARY

1. INTRODUCTION

Two priority issues in materials science have been identified in Member States that have high economic importance.

1. Enhancing and extending the useful working life of materials. Applications include surface treatments and coatings to improve the corrosion resistance of metals and glasses, reducing the rate of degradation of polymers, and hard coatings for reducing friction and increasing wear resistance.
2. Improved thin film structures and materials for more efficient optoelectronic and electronic devices. Applications include the technologically important silicon compounds such as SiC, Si_3N_4, a-Si:H and their variants.

These issues can be addressed through enhancement of accelerator-based nuclear analytical capacities for the quantitative analysis of light elements in thin films. Accelerator-based methods, so called Ion Beam Analysis (IBA) methods, offer an advantage over other methods due their quick measurement speed, non-destructive measurement, wide range of elements accessible to analysis, quantitative information provided, and all at relatively low cost.

Research activities in this coordinated research project (CRP) have been organized to address these issues, and are grouped into four main areas.

1. Organization of round robin measurements in order to address quality assurance matters.
2. Evaluation of databases of physical parameters needed for the analysis of specific thin films and surfaces.
3. Corrosion and related problems.
4. The role of hydrogen, carbon, nitrogen and oxygen in electrical and structural properties of semiconductors and other materials.

The following sections summarize the achievements in these four areas of activity. Comprehensive details are provided in the participants' reports. Throughout this publication there are numerous abbreviations. These are listed in the abbreviations section of this publication.

Light elements may be defined as those that emit very low characteristic K_α X ray energies and which are below the useful energy response function of a Si(Li) X ray detector (~ 1 keV). Light elements are thus loosely defined as those lighter than Al. This coordinated research project focuses on certain priority light elements that play a dominant role in influencing the performance of modern materials and functional devices, specifically; H, Li, C, N and O.

Most light elements occur in the form of compounds such as hydrides, borides, carbides, nitrides and oxides in engineered thin films and film systems, or in the near-surface region of bulk materials. Their composition and distribution determines to a great extent, the bulk material's surface mechanical, optical, electrical and chemical properties. Enhancing the performance of these materials and functional devices requires reliable quantification of these light elements and distribution, and knowledge on how to control and manipulate them. Through various case studies, this coordinated research project assesses and demonstrates the effectiveness of accelerator-based, nuclear techniques for analysis, providing valuable data and knowledge not readily accessible using other methods.

There is a large diversity in configurations and dimensions of structures: discrete single and multilayers; diffuse surface regions, and with thicknesses ranging from nanometres to many microns. The host matrices in which light elements reside vary widely in composition and form.

1.1. Organization of round robin measurements in order to follow quality assurance matters

An essential requirement of all analytical techniques is knowledge about the quality and reliability of the outputs produced. This CRP has, as a performance assessment tool, organized round robin measurements between collaborating laboratories in order to assess quality across the broad spectrum of different accelerator-based analytical techniques used.

Invitations were issued to many accelerator laboratories to participate in the measurement of thickness and stoichiometry of thin aluminum-oxy-nitride films denoted as S1 (Al:N, ~ 1 nm), S2 (Al:O:N, ~ 1 nm), S3 (Al:O:N, ~ 10 nm) and S5 (Al:O:N, ~ 100 nm). Many analytical techniques were proposed in the expressions of interest received from prospective laboratories. They were divided into two groups:

1. Accelerator-based nuclear techniques (RBS — conventional, high resolution, magnetic sector, and high energy; ERDA — heavy ion, TOF and gas-ionisation, LEIS; MEIS; NRA; PIXE; PIGE).
2. Non accelerator-based methods (SIMS — conventional, TOF and quadrupole; XPS; AES; XRD; XRF; FTIR; ellipsometry; various microscopies).

In the first group, all those techniques originally proposed were in fact used, with the exception of LEIS. On the contrary, most of the proposed techniques in the second group were not used at all. Of those laboratories that proposed to use exclusively the techniques from the second group, only three actually participated. All of these three laboratories were unable to determine the stoichiometry of the films. This is an indication that accelerator-based nuclear techniques have a distinct advantage for the analysis of thin aluminium-oxy-nitride films.

The averaged results for the thickness and composition of the Al:O:N films are given in Table 1. From the collated results, it was noted that not all laboratories could measure the thinnest samples S1 and S2. Those that could, mainly used heavy ion ERDA and NRA. A combination of other techniques also proved successful. Agreement between the different laboratories is very good, even for the ultra-thin samples for which measurement techniques are at their limits of capability.

Table 1. Averaged results of thickness and composition of aluminium oxynitride thin films

sample	thickness (10^{15} at/cm^2)	Al (10^{15} at/cm^2)	N (10^{15} at/cm^2)	O (10^{15} at/cm^2)	Al (at.%)	N (at.%)	O (at.%)
S1	30.5 ± 4.7	8.1 ± 3.1	1.7 ± 0.5	16.0 ± 1.9	34.8 ± 3.2	6.9 ± 2.8	54.9 ± 4.9
S2	30.9 ± 6.2	7.7 ± 3.4	1.0 ± 0.8	17.8 ± 1.1	32.9 ± 4.5	8.3 ± 5.6	57.6 ± 3.4
S3	209 ± 39	75 ± 12	8.3 ± 3.1	112 ± 14	38.1 ± 3.5	3.9 ± 0.9	53.9 ± 3.4
S5	1989 ± 161	732 ± 100	62 ± 16	1136 ± 52	37.0 ± 3.5	3.1 ± 1.3	55.4 ± 3.4

In a second intercomparison exercise, well-characterized Ta_2O_5 oxygen reference samples were distributed to participants to assist them quantify their experiments using the same traceable standard. The main advantage of using this common point of reference is that the results of different experiments carried out at different laboratories can be directly compared, and has thus facilitated collaborations. Further Ta_2O_5 reference samples are available for all laboratories. In this way, the benefits of this project have been extended to the scientific community at large.

The two harmonization exercises organized under this CRP have been very successful. IBA has been shown to be capable of quantitatively analysing light elements in ultra-thin films of current technological relevance. Harmonisation of NRA experiments for the determination of oxygen has also been achieved between large numbers of laboratories.

1.2. Databases of physical parameters needed for analysis of specific thin films and surfaces

It is known, for example, from the IAEA's Nuclear Data Section's databases [1], that some of the old nuclear data measured decades ago are not of sufficient quality for today's needs, and in some cases data do not exist at all. New, precise and accurate nuclear data need to be generated. As part of this CRP, selected nuclear reaction cross-sections and stopping powers were measured.

1.2.1. Nuclear reaction cross-sections: The $H(\alpha,p)^4He$ and $^{12}C(\alpha,\alpha)^{12}C$ reactions

For the first time, differential cross-sections for the $H(\alpha,p)^4He$ reaction have been measured for the angular range from 45º to 60º for a variety of incident beam energies. New data for the angular range from 30º to 45º were also generated. Results are presented in Table 2.

Table 2. Differential $H(\alpha,p)^4He$ cross-sections (mb/sr) as a function of incident beam energy (keV). The error is estimated to be less than 7% for all energies

E (keV)	30°	40°	45°	50°	55°	60°
2500	350	360	421	426	488	-
3000	323	310	320	319	349	449
3500	321	296	288	297	306	337
4000	361	314	265	244	221	250
4500	399	316	262	262	239	216

All measured differential cross-sections, except that for 60°, deviate from the Rutherford value. These experimental results were compared with other available experimental data for lower recoil angles and also, with theoretical calculations obtained by fitting the phase shifts of the kinematic inverse reaction using the principle of detailed balance. Good agreement was found between these new experimental data and other published data. Comparison of the theoretical data shows reasonable agreement for low recoil angles, but at 55° and 60°, the theoretical differential cross-sections are significantly higher than the experimental data.

The differential cross-sections for $^{12}C(\alpha,\alpha)^{12}C$ change significantly with different energies and scattering angles. For backscattering angles and energies higher than 3 MeV, all cross-sections exceed Rutherford values. For energies from 3.5 to 4.1 MeV and scattering angles typical for RBS (150°-170°), the $^{12}C(\alpha,\alpha)^{12}C$ differential cross-sections are quite smooth and suitable for the determination of the carbon content in heavier matrices. The resonance at 4.26 MeV can be used to enhance depth resolution, especially in cases when low amounts of carbon are present in the sample. In the analysis of SiC films, differential cross-sections for both elements can be measured simultaneously.

Differential cross-sections for the $^{12}C(\alpha,\alpha)^{12}C$ reaction have been measured at angles of 30°, 45°, 60°, 135° and 150° in the energy range from 2 to 4.8 MeV and compared with existing experimental data and optical model calculations. For the first time, differential cross-sections were also measured for some forward angles that can be used for forward scattering measurements and also for normalization purposes in ERDA.

From new measurements of the $^{12}C(\alpha,\alpha)^{12}C$ resonance scattering cross-section at 4.26 MeV and 165°, it was found that the differential cross-section at the resonance energy is about 12.5% smaller than that reported in the literature. Also found was that resonance energy of the $^{28}Si(\alpha,\alpha)^{28}Si$ reaction, which is

close to that of the $^{12}C(\alpha,\alpha)^{12}C$ resonance energy, should be increased by 13 keV than that as reported in the literature. The $^{12}C(\alpha,\alpha)^{12}C$ data obtained in this CRP are in very good agreement with the recommended values [2].

1.2.2. Stopping powers and range parameters of light ions and molecules in random and channeling directions in Si and SiO_2

The random stopping powers of He, Be and O in Si have been measured in the energy range between 200 keV and 13.5 MeV. The results agree well with other published measurements and have been parameterized according to the formula proposed by Kalbitzer and collaborators [3]. The channeling stopping powers of Li, Be and O in Si have also been measured in the energy range from 200 keV to 13.5 MeV. These results have been correlated with those carried out at a random direction since they are used as an input to the calculation of the channeling results.

Channeling data play an important role in the understanding of polarization effects during the interaction ion-matter. The measurement of channeling energy loss of a wide variety of light ions (He, Li, Be, B and O) in channeling directions in Si has proved to be very important for the clarification of fundamental issues such as the Barkas effect, which reflects the influence of the polarization process during the ion-matter interaction. Moreover, these results open new possibilities for further research to be pursued both in fundamental and applied fields.

The stopping power of molecules in thin targets is substantially larger than the sum of the individual stopping power of their constituents. Therefore, molecules become more useful where light ions and large energy depositions are required. The molecular stopping power of H_3 as well as the energy straggling of H has been measured for thin SiO_2 films. The results have provided new information on the effects of the inhomogeneous distribution of electrons in calculations of straggling in this structure.

The range parameters R_p and ΔR_p of O in SiO_2 in these thin films have also been measured. These parameters are important quantities used in the production of microelectronic devices.

A computationally expensive, but experimentally simple method to determine stopping powers based on energy spectra alone was developed. A Bayesian inference algorithm using Markov chain Monte Carlo integration was developed. This method was used to determine the stopping power of $^4He^+$ in Si, SiO_2 and Al_2O_3, where the Bragg rule for addition of elemental stopping powers is not valid.

1.3. Corrosion and related problems

1.3.1. Improving the understanding of the oxidation of nanoporous titanium surfaces produced by low-energy helium implantation

Helium ion implantation into polished titanium surfaces was performed using plasma-immersion ion implantation and accelerator based ion implantation with the aim to fabricate nanoporous titanium surfaces. Light elements and their depth distributions were successfully measured with ion beam analysis. Proton microprobe analyses revealed that helium implanted surfaces took up more oxygen from the atmosphere than unimplanted surfaces. Nanoporous surfaces exposed to heavy ions took up twice as much oxygen and over ten times as much nitrogen as the immediately adjacent undisturbed helium implanted surface. High energy, heavy ion TOF-ERDA also significantly modified the surface topology - after long times of analysis, the implanted helium layer disappeared.

1.3.2. Understanding the oxidation of amorphous silicon nitride and crystalline silicon carbide

Thin films of chemical vapour deposited silicon nitride on (100) silicon were measured with ion beam analysis using TOF-ERDA. Depth profiles of Si, N, O and H were obtained. From these depth profiles, an oxygen enrichment was observed both at the surface of the film and at its interface with the bulk silicon. Some erosion of the film material was observed after ion beam irradiation, and was subsequently investigated using atomic force microscopy.

TOF-ERDA has been used with mixed success to depth profile light elements in new emerging materials for various applications. In some materials, TOF-ERDA provided information that is useful to improve the materials performance. However, for many other materials, e.g. silicon nitride and implanted titanium, TOF-ERDA significantly affected the integrity of sample's surface. The ion beam interactions that cause this surface modification have not been identified.

Knowledge gaps exist in the properties of certain materials identified for application in high temperature and radiation hardened sensors and devices. One such example is silicon carbide (SiC) a material of outstanding physical and chemical properties. Accelerator-based nuclear analytical techniques have been applied to investigate the oxidation kinetics of this technologically important material.

Isotopic tracing was used to follow the oxidation mechanism of SiC. First, double face polished 6H-SiC samples were oxidised in a very dry oxygen atmosphere. Subsequent oxidations in $^{16}O_2$ and $^{18}O_2$ were made. Ion beam analysis was used to measure the relative oxygen isotope concentrations and depth profiles. The SiO_2 layers that formed on SiC were found to be stoichiometric. The oxidation rate of SiC on Si terminated surfaces was found to be about 10-times faster than the oxidation rate of <100> Si, and is about 5-times slower for the C-terminated surface.

1.4. The role of hydrogen, carbon, nitrogen and oxygen in electrical and structural properties of semiconductors and other materials

1.4.1. Quantitative analysis of amorphous hydrogenated SiC thin films (a-SiC:H) for optoelectronics and protective coatings

Amorphous hydrogenated SiC thin films are used in solar cells, in light emitting diodes, phototransistors, and hard coatings. The properties of a-SiC:H critically depend on the composition and structural ordering. Hence, reliable characterization methods are very important to elucidate these properties.

Thin a-SiC:H films on a Si substrate were produced by a magnetron sputtering process. The ion beam techniques of conventional RBS/ERDA, ERDA using time-of-flight and ΔE(gas)-E(PSD) techniques, and Forward Scattering were successfully applied to determine the stoichiometry, depth profiles and thicknesses of the thin films.

In conventional RBS, problems can arise when analyzing light elements in heavy matrices, such as SiC films. RBS between 3.5 and 4 MeV He ions can be useful at backward angles, as the cross-sections for helium scattering on carbon are a few times higher than the Rutherford values. For very thin films (few tens of nm) conventional RBS/FS was found to be not sensitive enough in most cases. By using Forward Scattering, all elements present in the film can be detected simultaneously. High sensitivity and good depth resolution was achieved with ERDA using Time-Of-Flight and ΔE(gas)-E(PSD) techniques. To enhance the depth resolution for carbon analysis at the near surface region of the samples the 4.26 MeV $^{12}C(\alpha,\alpha)^{12}C$ elastic resonance was applied.

Using classical RBS, carbon can be successfully profiled and quantified using 3.5 - 4 MeV He beams due to the enhanced cross-sections (e.g. enhancement factor = 6 at 165º). For very thin films (a few tens of nm), heavy ion mass resolving ERDA and the 4.26 MeV $^{12}C(\alpha,\alpha)^{12}C$ elastic resonance methods and high resolution magnetic spectrometry can be used to better effect in analyzing the SiC films.

1.4.2. The determination of hydrogen and nitrogen in silicon nitride films produced by plasma enhanced chemical vapor deposition to control production processes

Silicon nitrides are the alternative to SiO_2 dielectrics in modern semiconductor technology. Quantified measurements of the chemical composition are very demanding due to the substantial presence of hydrogen in the silicon nitride layer, which is a by-product of the production process.

Conventional RBS/ERDA analysis, ERDA using time-of-flight, ERDA using ΔE(gas)-E(PSD) technique and forward scattering were all applied to determine the stoichiometry and thickness of plasma enhanced chemical vapour deposition silicon nitride films, provided by the Institute 'Jožef Stefan', Ljubljana, Slovenia. Ion beam techniques used in the round-robin measurements are capable, in a single measurement, of providing the complete Si:N:H stoichiometry as well as the different elemental depth profiles. The measured Si:N concentrations were found to be consistent with the trend in the production parameters. The hydrogen concentration shows a very constant depth profile throughout the layer, which has been verified using the $^{15}N(p,\alpha\gamma)^{12}C$ reaction. As a spin-off, this constancy in the hydrogen profile enables it to be potentially used as a thick hydrogen standard for ion beam analysis. The benefit being greater resistance to the ion beam induced hydrogen desorption process that occurs with the conventionally used Kapton™ material. In summary, mass resolving ERDA methods are the most appropriate techniques in analyzing thin layer systems comprising several light elements, such as silicon nitride.

1.4.3. Measurements of TiN/Ti/Steel multilayers samples prepared by physical vapour deposition reactive magnetron sputtering

An IBA method was developed to analyze TiN/Ti/Stainless steel multilayer coatings. Such techniques are needed to provide feedback on the plasma coating production parameters and also to control the quality of the coatings for corrosion resistance. RBS and NRA using a 1400 keV deuterium beam was used to measure individual thicknesses of the Ti and TiN_x layers in the multiplayer stack, as well the nitrogen concentration in each of the TiN_x layers.

Analyses of the particle energy spectra are very complex and time-consuming using computer codes such as RUMP, SIMNRA, etc. Instead, the computer code WINDF was found to be more appropriate, with spectral analyses being performed using data from both the RBS and the NRA measurements. The use of this code allowed a fast analysis of a large number of samples.

Relatively thick (0.75 to 9.8 μm) TiN/Ti multilayers can be used to significantly improve the corrosion resistance of type 304 stainless steel substrates. The corrosion resistance was found to be dependent on the number of layers in the coating. The improvement in the corrosion resistance was evidenced mainly through a strong reduction in the rate of attack by pitting. The TiN layers deposited using different magnetic fields showed that the corrosion resistance is also strongly dependent on the amount of ion bombardment during growth, and increased when the amount of bombardment is high. The interplanar distance is influenced by changes in the ion bombardment caused by the magnetic field.

2. CONCLUSIONS

The round robin exercise undertaken as part of this CRP has demonstrated the ability to provide reliable and quantitative data for a most demanding system. The participating laboratories that have high quality facilities were able to measure all the samples distributed, while others could only

measure the thicker samples. Further improvement in analytical facilities and experimental method is required in some laboratories. Nearly all experimental results reported agree within statistical limits. Unexpected deviations can mostly be attributed to participants using different nuclear and atomic databases for analysis, using different analytical software packages, and inaccuracies in measuring some key experimental parameters. These observations indicate a need to harmonise the various nuclear and atomic databases used for IBA analysis, and also, enhance quality assurance and control protocols to calibrate measured quantities such as charge and solid angle.

Quantitative spectral analysis is sensitive to the stopping power data used, especially when using heavy ions. More precise measurements of the energy stopping powers are required to improve the spectra evaluations. Also, the hydrogen elastic recoil cross-sections for lithium ions should be measured, as this ion beam species is being more widely used as an alternative to the conventional ERDA method using helium ions.

For the $H(\alpha,p)^4He$ differential cross-section, it is an opportune time to evaluate all existing measurement data for different scattering angles and energies, to derive recommended parameters for ERDA users. This is especially important for the recoil angles between 30° and 45°, which are most commonly used geometry.

The outputs of this CRP demonstrate that accelerator based nuclear techniques of analysis can provide reliable quantitative information on a wide range of emerging materials of technological importance. Of main importance is to harmonize databases, and to supplement it with reliable information in areas where there are identified deficiencies. Additionally, quality assurance protocols need to be strengthened, and suitable reference standards provided, to ensure all Member States provide high quality, and comparable information.

REFERENCES

[1] INTERNATIONAL ATOMIC ENERGY AGENCY, Report on the IAEA Technical Meeting on Database of Evaluated Cross-Sections for Ion Beam Applications, INDC(NDS)–449, Vienna (2003).

[2] GURBICH, A.F., Evaluation of the cross-section for elastic scattering of ^4He from carbon, Nucl. Inst. Meth. B161-163 (2000) 125.

[3] DOS SANTOS, J.H.R., BEHAR, M., GRANDE, P.L., BOUDINOV, H., STOLL, R., KLATT, CHR., KALBITZER, S., Electronic stopping power of ^{10}B in Si in random and <100> channeling directions. Phys. Rev. B55 (1997) 13651.

CORROSION STUDIES OF TiN/Ti MULTILAYERS

E. Andrade, E.P. Zavala
Instituto de Física, Universidad Nacional Autonoma de México,México

M. Flores
Depto. de Ingeniería de Proyectos, Universidad de Guadalajara,México

M.F. Rocha
Escuela Superior de Ingeniería Mecánica y Eléctrica, IPN, México

N.P. Barradas
Instituto Tecnológico e Nuclear, Portugal

S. Muhl
Instituto de Investigaciones en Materiales, Universidad Nacional Autonoma de México, México

Abstract

TiN/Ti multilayers, 1.74 – 9.80 μm thick, with different number of layers were deposited on 304 stainless steel substrates by reactive magnetron sputtering. It is known that such multilayers can improve the corrosion resistance of metallic substrates. The titanium layers help to reduce the incidence of pinholes that occur because of irregularities in the substrate surface, and decrease the porosity of subsequent TiN coatings by improving the layer microstructure. One group of multilayers were prepared using balanced magnetron sputtering with a concentric electromagnet coil around the magnetron in order to produce a variable unbalance of the magnetron, and in this way provide changes in the ion bombardment of the substrate. It was observed that the additional magnetic field increased the plasma temperature as well as altering other plasma characteristics. The field caused changes in the ion bombardment of the substrate and was found to modify the film microstructure**.** A 1400 keV deuterium beam was used to analyze the samples, and combinations of RBS/NRA methods were applied to evaluate the sample spectra. The $^{14}N(d,\alpha_1)^{12}C$ NRA cross sections are well known and were used as a way to determine the ^{14}N concentration in the TiN_x layers. The corrosion resistance of the layers was studied by means of potentiodynamic polarization scans in a 0.5 M NaCl solution. The corrosion test demonstrated that the number of TiN/Ti layers determined the corrosion resistance and the unbalancing of the magnetron improved the corrosion resistance.

1. INTRODUCTION

Austenitic stainless steel can suffer from localized corrosion in saline environments, such as seawater, and this is attributed to intergranular corrosion attack. In general, stainless steel is a relatively corrosion resistant material because of the formation of a passive chromium oxide surface layer. However, if this layer is damaged by erosive wear, the corrosion is accelerated [1]. One way to protect stainless steel against corrosion is by the application of hard coatings that are resistant to both wear and corrosion. TiN hard coatings are intrinsically very chemically stable. However, monolayer films of TiN deposited on steel by physical vapour deposition (PVD) techniques, such as magnetron sputtering, generally have a columnar

microstructure and when they are exposed to a corrosive environment the defects and pinholes in this microstructure that propagate through the film act as pathways for the corrosive liquids. Moreover, the noble TiN coating and the active metallic substrate form a galvanic pair that can accelerate the pitting corrosion.

TiN/Ti multilayers have been used to reduce the coating porosity since the interfaces between the layers act as barriers that restrict the pathways to the substrate; therefore, the use of multilayers tends to increase the corrosion resistance. It was reported [2-3] that multilayers with graded interfaces are more corrosion resistant than multilayers with sharp interfaces. When TiN/Ti multilayers are deposited without deposition interruption, the interface between TiN and Ti is thicker than the interface between Ti and TiN. This effect is attributed to residual nitrogen on the target [4]. The ion bombardment controlled by the magnetic fields of an unbalanced magnetron can be used to improve the microstructure, and therefore, the corrosion resistance of TiN/Ti multilayers [5]. The magnetic field changes the ion bombardment of the substrate and it was found to modify the film microstructure through the changes in the ion-to-atom ratio J_i/J_a: this changes the average energy per depositing atom [6]. The structure zone model of Thorton [7] shows the relationship between the normalised temperature and the pressure and the resulting microstructure of the PVD prepared films. The modified structure zone model of Messier [8] introduced the polarization voltage of the substrate, and more recently it was proposed that the ion to atom ratio was another axis of the structure zone model [9]. In TiN/Ti multilayers, the titanium layer is known to help in reducing the incidence of pinholes and decreases the porosity of subsequent TiN coatings by providing new nucleation sites for each layer.

The aim of this work is to study the corrosion resistance of multilayers of TiN/Ti deposited on stainless steel and the influence of the magnetic field on the corrosion resistance of TiN/Ti deposited on H13 substrates. The determination of the Ti and TiN_x layer thickness and the N concentration "x" are important parameters to measure and IBA methods are appropriate for this end. Additionally, we report some details of the IBA methods established here to analyze the TiN/Ti multilayers samples.

2. EXPERIMENTAL DETAILS

Two groups of samples were prepared; the first are compounds of multilayers deposited at a constant magnetic field with the number of layers deposited on 304 stainless steel substrates varying from two to 14. The second set was of multilayers with six regular periods deposited using different magnetic fields on H13 steel. All the substrates were prepared using 600 and 2000 grit abrasive paper and polished with 1 μm and 0.5 μm diamond paste. Prior to deposition, the substrates were ultrasonically cleaned, first in acetone and then in isopropanol.

Figure 1 is a photograph of the stainless steel reaction chamber used for the deposition of multilayer coatings by reactive magnetron sputtering. A concentric electromagnet coil around the balanced magnetron was used to produce a variable unbalance of the magnetron as is shown schematically in Figure 2. In this figure we also show the array of probes used to measure the plasma characteristics. The results of the plasma studies were published elsewhere [5].

Figure 1. The chamber used to deposit the multilayers, with the coil concentric to magnetron.

For both groups of samples the titanium target was 10.20 cm in diameter, 6 mm thick and of 99.99% purity. The TiN/Ti multilayers were produced using an argon plasma for the titanium layers and a mixture of argon plus nitrogen for the titanium nitride.

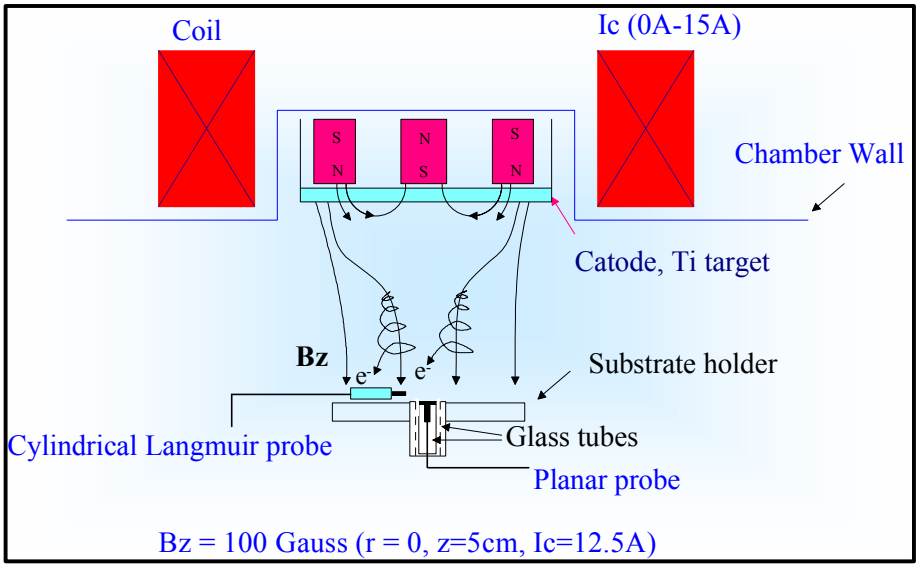

Figure 2. Schematic drawing of the concentric electromagnet coil around the balanced magnetron used to produce a variable unbalance of the magnetron and the position of the probes used to study the plasma.

2.1. Deposition conditions for the samples with different number of layers

The temperature of the stainless steel substrates was maintained at 400°C, the samples were grounded and placed 5 cm from the target. The deposition pressure for both layers was 0.53 Pa (4 mTorr), total gas flow of 10 sccm. The first deposited layer on the substrate was Ti and the last was TiN_x. The change from Ti to TiN_x deposition was achieved by controlling the nitrogen flow without plasma interruption, so that a graded interface was generated. The following notation was used to identify the sample: nTiNnTi, where "n" is the total number of

layers. The samples analysed in this work were for n =1, 2 and 7, with total thickness 1.74 – 9.80 μm.

2.2. Deposition conditions for the samples deposited with variable magnetic field

The substrates were samples 2.54 x 7.62 x 1.27 cm^3 made of cut pieces of rolled and annealed commercial plate steel (AISI H13) without thermal treatment, they were polished using 2000 grit abrasive paper and finished with 1 μm and 0.5 μm diamond paste. The multilayer coatings were deposited by magnetron sputtering in an argon plasma. The titanium layers were deposited by sputtering in an atmosphere of argon plus nitrogen for 4 minutes, while the titanium nitride layers were deposited by sputtering for 10 minutes. Each deposited layer was 150 ± 30 nm thick. The temperature of the substrates was maintained at 450°C and the substrates were placed 5 cm in front of the target. The change from Ti to TiN deposition was the same as for the first sample set. For all the specimens, the layer deposited first was of Ti and the last of TiN. A bilayer sample with a Ti layer, 280 nm thick, and a TiN layer of 2 μm was prepared as a reference.

The corrosion resistance of the multilayers was evaluated using the potential-current curves obtained by potentiodynamic polarization scans in a NaCl 0.5 M solution (29.22 g/l). Fig. 3 is a schematic diagram of the three electrodes used for the corrosion resistance measurements. A saturated calomel electrode was used as the reference electrode. The potential sweep rate was 10 mV/min performed at room temperature (22°C). The sidewalls of the samples were double-painted with enamel, leaving a 0.9 cm diameter circle in contact with the solution. The corrosion current was estimated by a linear fit and Taffel [1] extrapolation to the cathodic part of the polarization curve.

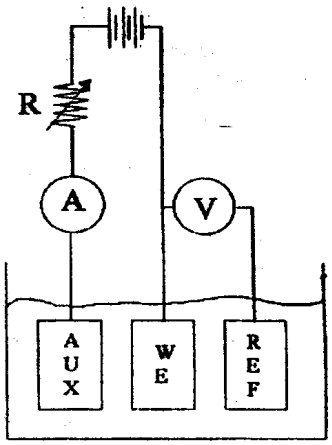

Figure 3. Schematic diagram of the arrangement of the three electrodes used in the corrosion studies.

The IBA facilities of the Institute of Physics of the National Autonomous University of Mexico based on a single ended 5.5 MV Van de Graaff accelerator [6] were used to obtain the atomic composition profiles and the TiN/Ti multilayers thickness. Several possibilities were considered to choose an appropriate IBA method. It is known that a standard 2 MeV $^4He^+$ RBS method is limited to analyse about the first 2 μm from the target surface. We choose a combination of RBS/NRA method described below. A 1480 keV $^2H^+$ beam was used to bombard the samples so that several nuclear reactions with positive Q values, such as: $^{14}N(d,\alpha_i)^{12}C$ (i = 0, 1, 2, 3) and $^{14}N(d,p_j)^{15}N$ (j = 0, 1, 2, 3, 4, 5) are possible. A surface barrier detector, 1000 μm thick, equipped with a standard electronics set at θ = 150° was used to measure the energy of particles. We did not insert a particle absorbing foil in front of the

detector, hence, the system was able to simultaneously measure the spectrum from the $^{2}H^{+}$ RBS low energy region and the high particles energy region of the nuclear reaction particles.

3. RESULTS AND DISCUSSION

Figure 4 shows the magnetic field B_z produced from the permanent magnets and its modification for different coil currents Ic. (Ic =0, 5, 10 & 12.5 A). It was observed that the plasma characteristics were strongly influenced by the magnetic field resulting in a focused central zone of the target [5].

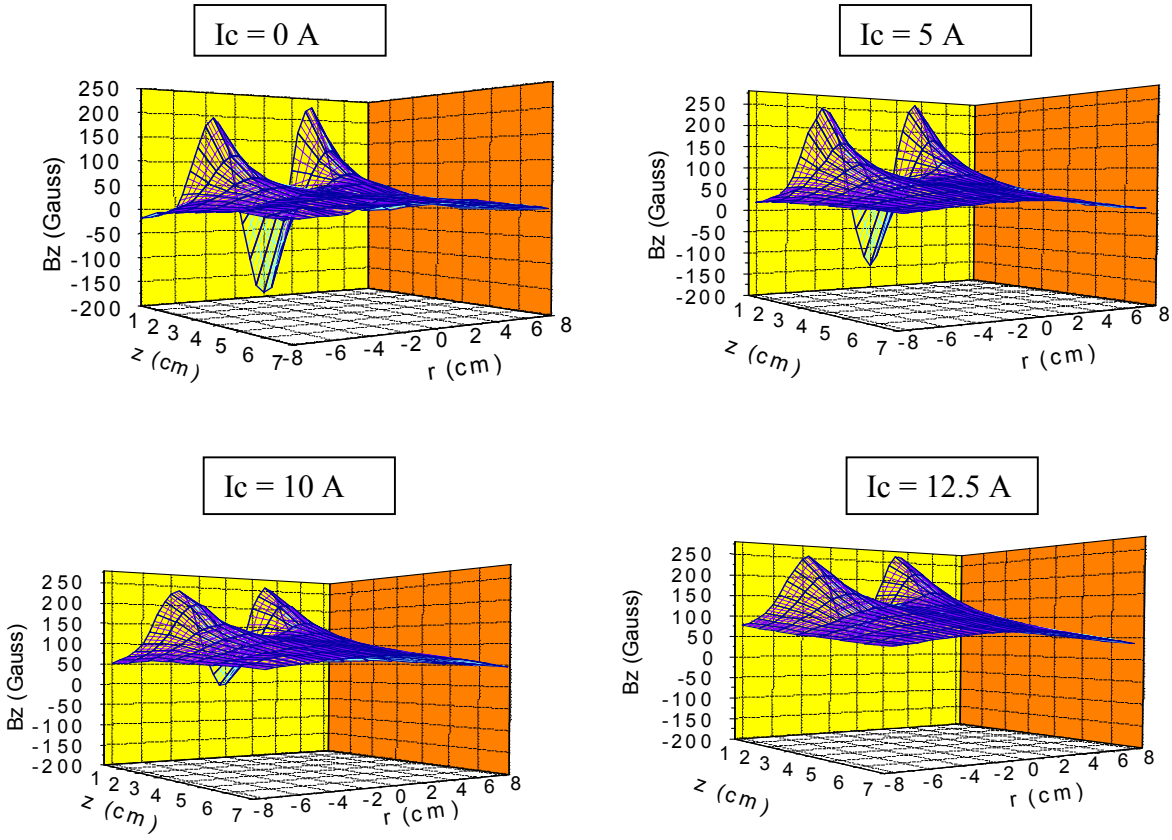

Figure 4. Magnetic field produced by the sum of the fields from the permanent magnets of magnetron and the coil current.

3.1. Corrosion resistance of multilayers produced with variable magnetic fields

The polarization curves are shown in Figure 5, and it can be seen that the multilayers reduce the corrosion current i_{corr} by an order of magnitude for the multilayers deposited at 10 A, and by 5 times for the multilayer deposited at 12 A relative to the uncoated substrate. The corrosion potential E_{corr} of the multilayers was found to be nobler than the substrate. This improvement indicates that there had been a reduction in the density of defects and pinholes in the multilayer deposited at larger ion bombardment.

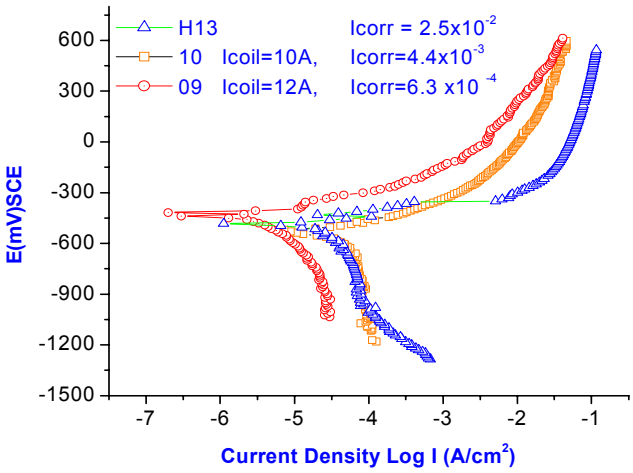

Figure 5. Polarization curves for the multilayers deposited at different coil current.

Fig. 6 shows the temporal evolution of the open circuit potential or rest potential (E_{rest}). The three multilayers start with positive potential values that are nobler than the substrate. The potential of 1Ti1TiN shows a decrease similar to the substrate and no passivation is observed. The samples 2Ti2TiN and 7Ti7TiN begin with an increase in the potential associated with surface passivation, but after ~10 minutes the potential began to decrease, indicating surface activation. All the coated samples have a more noble value of E_{rest} 1 hour after the immersion (see table 1), but somewhat surprisingly the value is not related to the numbers of layers.

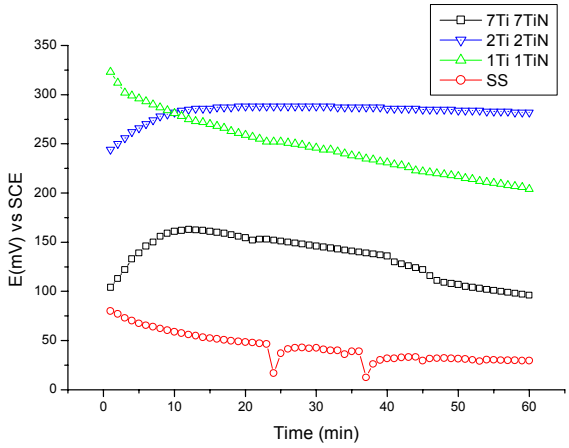

Figure 6. Evolution in the time of the open circuit potential or rest potential (E_{rest}) for the indicated nTiNnTi/SS multilayers and for the 304 SS substrate.

Fig. 7 shows the polarization curves for the samples with different numbers of layers and the substrate. The multilayers 1Ti1TiN and 2Ti2TiN show a current similar to the substrate value in the cathodic region, so the corrosion current i_{corr} estimated for these samples is only about half that of the substrate, however, the 7Ti7TiN sample performs much better. In the anodic region, the coated samples are better than the substrate and have a similar behaviour until pitting begins. Here the currents are different by orders of magnitude depending on the number of layers in the multilayer. The sample 2Ti2TiN showed a variation in the current that is an indication of passivation and activation cycles. This behaviour is maintained during almost all of the polarization, until a potential value near to the pitting point is reached.

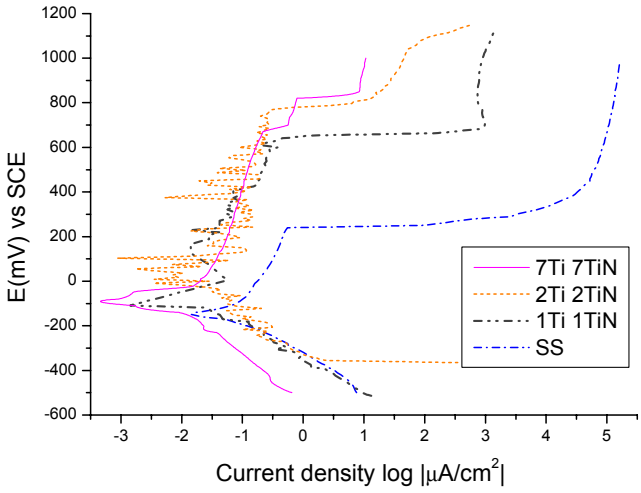

Figure 7. Polarization curves for samples with different numbers of multilayers on the substrate.

Table 1 shows the electrochemical parameters obtained in this work for the multilayers deposited on the stainless steel substrates. The E_{corr} potential, when the current is zero for the coated samples, is less active than the substrate, but no clear tendency exists. The corrosion current i_{corr} is lower for the multilayers and smallest for the thickest coating. The i_{corr} values were estimated from the cathodic region.

Table 1. Electrochemical parameters for multilayers with different numbers of layers

Sample	E_{rest} (mV) After 1h	E_{corr} (mV) (i = 0)	E_{pit} (mV)	i_{corr} (μA/cm^2)	i (E = 1V) (μA/cm^2)
304SS	29.6	-150	220	5.6×10^{-2}	1.62×10^{5}
1T 1TiN	282	-110	620	2×10^{-2}	933
2Ti 2TiN	204	-75	680	2.4×10^{-2}	46.7
7Ti 7Ti	96	-95	720	7×10^{-3}	10.7

Since the weak point of the substrate and the coatings is pitting (which occurs in the anodic region), possibly this parameter in not the best to compare the corrosion resistance of these samples. Therefore, an analysis of the pitting potentials and the current response after the pitting was performed as a complimentary way to compare the corrosion resistance. The pitting potential of multilayers is nobler than the substrate and is related to the number of layers. The largest pitting resistance was seen for the sample with the most layers and was almost four times better than the substrate. The current at 1 V, a potential after which pitting has begun, is lower for all the coated samples by at least three orders of magnitude and for the thickest sample with 14 layers is four orders of magnitude less than the substrate.

3.2. Results of the XRD and IBA studies

Fig. 8a shows the experimental RBS spectrum (dots) from the 1400 keV ^{2}H bombardment of the 6 TiN6Ti sample. The peaks in this spectrum correspond to the Ti layers and the valleys correspond to the TiN_x layers. Fig 8b is part of the corresponding high energy region of the

spectrum where the $^{14}N(d,\alpha_1)^{12}C^*$ peaks are displayed. There the peaks corresponds to the nitrogen in the TiN_x layers and the valleys corresponds to the Ti layers. The task of simulating such complex spectra using traditional computer codes such as RUMP, SIMNRA, etc., are very time consuming. The solid line in the spectrum represents the WINDF simulation code [10].

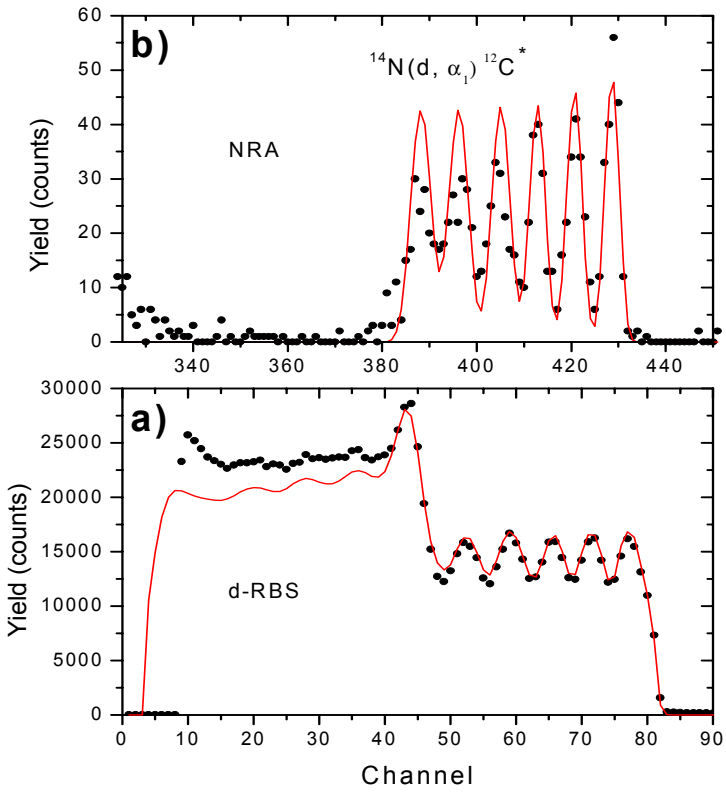

Figure 8. a) The experimental RBS spectrum (dots) for a 1400 keV ^2H beam incident on a sample made of 6TiN6Ti layers. b) The $^{14}N(d,\alpha_1)^{12}C$ NR of the spectrum. The solid lines represent the WINDF fit to the spectrum. The average thickness for TiN_X layers was 875 and for the Ti layers was 816 nm, respectively. The measured ratio Ti/N =0.88.

The approach of this programme tries to answer the question: "given RBS or NR data, what is the depth profile"? The $^{14}N(d,\alpha_1)^{12}C^*$ NRA cross sections were added to this program to obtain the nitrogen fit in the TiN_x layers by NRA. The solid line in Fig. 8b is the simulation of the $^{14}N(d,\alpha_1)^{12}C^*$ peaks using the nitrogen content "x" of each of the TiN_x layers obtained from the RBS fit. The good fit to the NRA spectrum shows that the determination of the nitrogen by the RBS was correct. The WINDF simulation shows that the ratio Ti/N = 0.88 ratio, i.e. the layers are nitrogen rich. The element profile of this sample was carried out using 6 bilayers of TiN_x–Ti, plus the substrate sublayer. The average thickness for the TiN_x was 406 nm and for the Ti was 278 nm, with a total coating thickness of 4122 nm. The bulk densities for the TiN (4.51 g/cm^3) and for Ti (5.68 g/cm^3) were used to transform the IBA monolayer thickness (10^{15} atoms/cm^2) to linear thickness (nm).

Fig. 9a shows the experimental RBS spectrum (dots) from the 1480 keV ^2H bombardment of the 5TiN65Ti sample. The thickness of the TiN_x and Ti layers do not allow observation of the individual layer contribution in the spectrum. However, the corresponding high energy region

of the spectrum where the $^{14}N(d,\alpha_1)^{12}C^*$ peaks are displayed in Fig. 9b the nitrogen peaks from the TiN_x peaks are resolved. The average thickness of the TiN layers were 875 nm and for the Ti 816 nm. The ratio Ti/N = 1.25 indicates that the TiN_x layers are Ti rich.

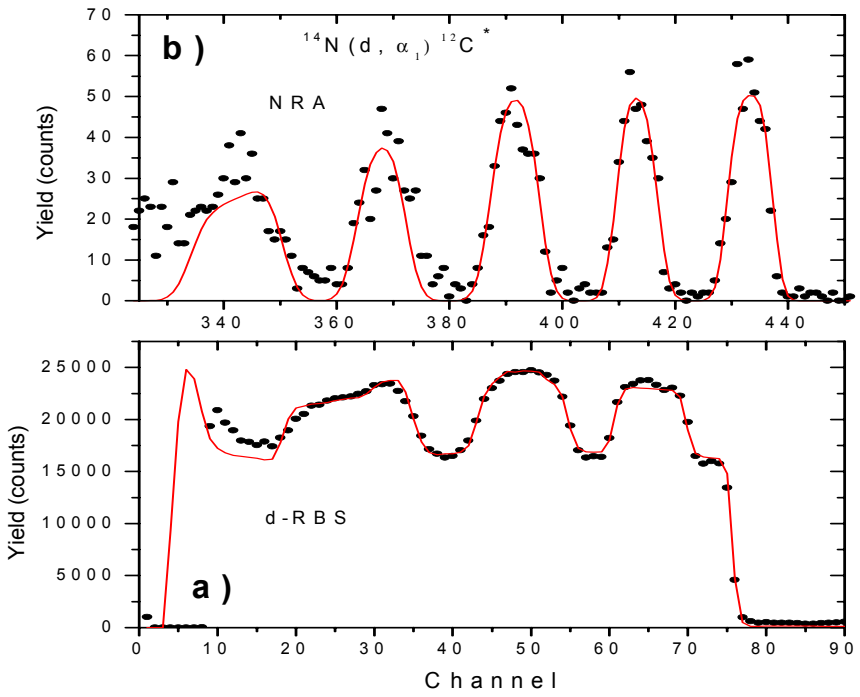

Figure 9. a) The experimental RBS spectrum (dots) for a 1400 keV ^2H beam incident on a sample made of 5TiN5Ti layers. b) The $^{14}N(d,\alpha_1)^{12}C$ NR of the spectrum. The solid lines represent the WINDF fit to the spectrum. The average thickness for TiN_X layers was 875 nm and for the Ti layers was 816 nm respectively. The measured ratio Ti/N = 1.25.

Fig. 10 is the spectrum for a 2TiN2Ti/SS (2 bilayers) and Fig. 11 is the spectrum for a 1TiN1Ti/SS (1 bilayer). The WINDF simulated layer thickness for the TiN and Ti layers and the Ti/N ratio are given in the figure captions.

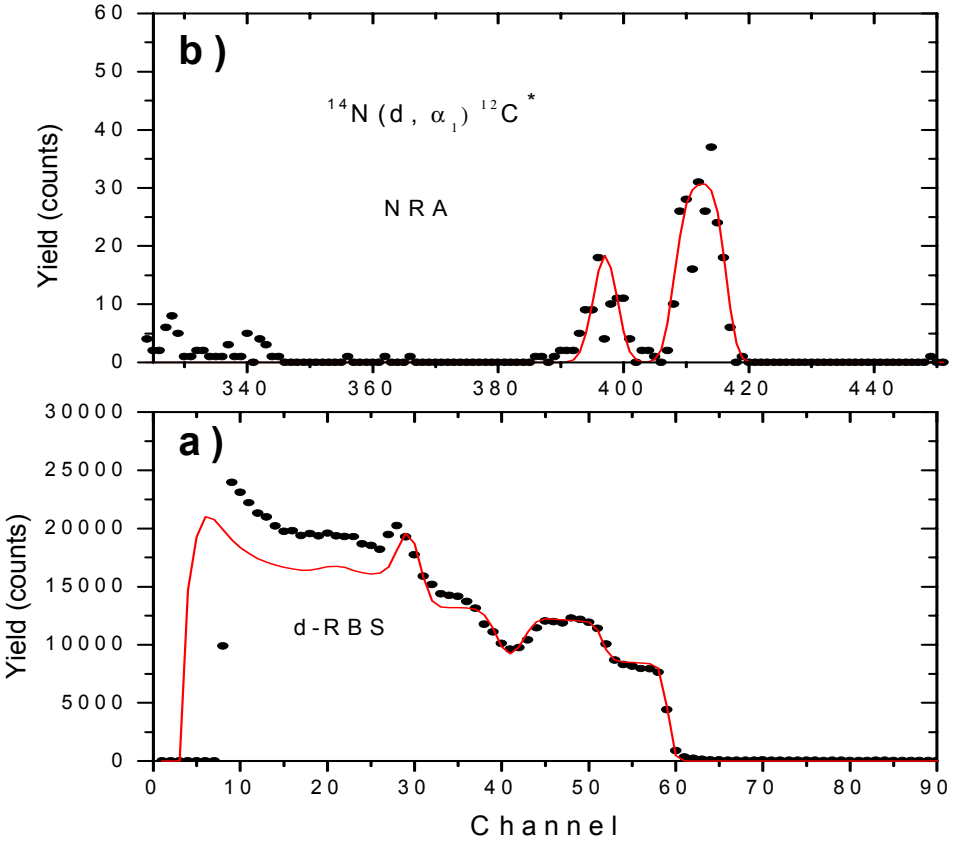

Figure 10. a) The experimental RBS spectrum (dots) for a 1400 keV ^2H beam incident on a sample made of 2TiN2Ti layers. b) The $^{14}N(d,\alpha_1)^{12}C$ NRA of the spectrum. The solid lines represent the WINDF to the spectrum. The thickness for the first and second TiN_X layers are 956 nm and 392 nm, respectively and for the first and second Ti were 675 nm and 648 nm. The measured ratio Ti/N = 1.26.

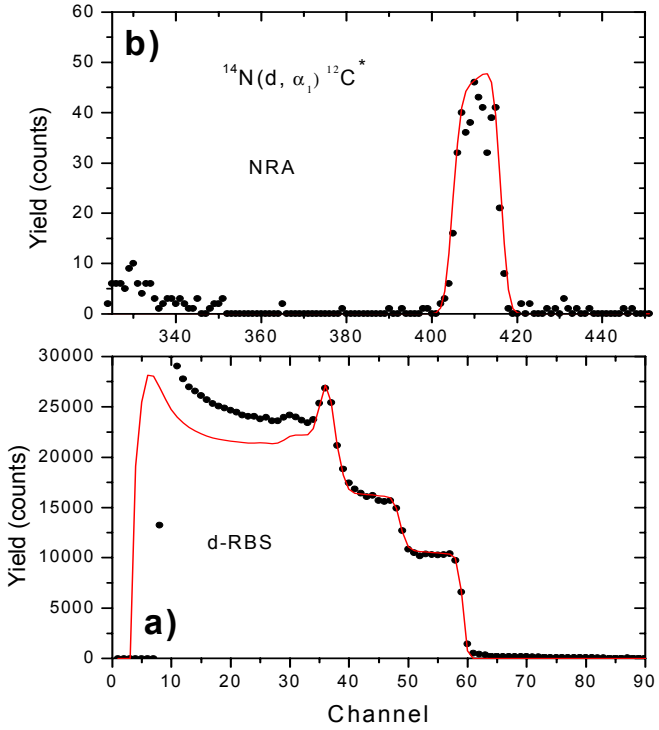

Figure 11. a) The experimental RBS spectrum (dots) for a 1400 keV 2H beam incident on a sample made of 1TiN1Ti layers. b) The 14N(d,α1)12C NRA of the spectrum. The solid lines represent the WINDF fit to the spectrum. The thickness of TiNx layers was 1411 nm and for the Ti was 912 nm. The measured ratio Ti/N = 1.00.

In Figure 12 we show the XRD spectra for multilayers deposited at different magnetic fields. The interplanar distances d_{111} and d_{200} of the TiN layers deposited at higher ion bombardment are seen to reduce.

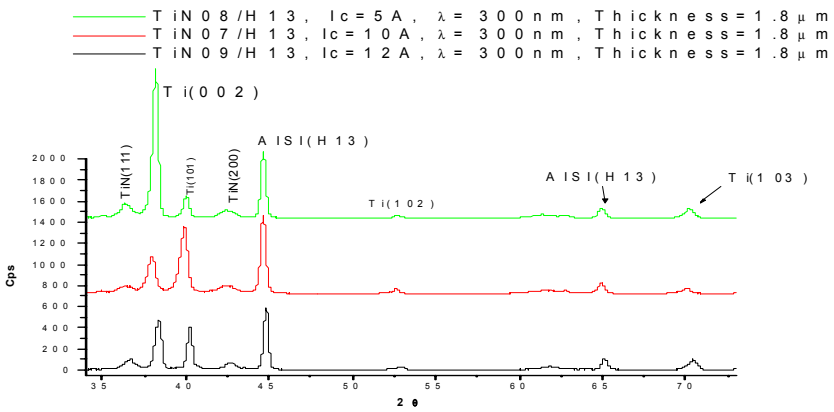

Figure 12. XRD pattern of multilayers as a function of the coil current.

In Figure 13 we show the XRD spectra of the sample with 14 layers. The principal planes of preferential orientation Ti (002) and (111) and (200) for the TiN are similar to those of

samples deposited at variable magnetic field in Figure 12. However, in this sample produced without an additional magnetic field, the preferential orientation is less strong, and more planes of orientations are present.

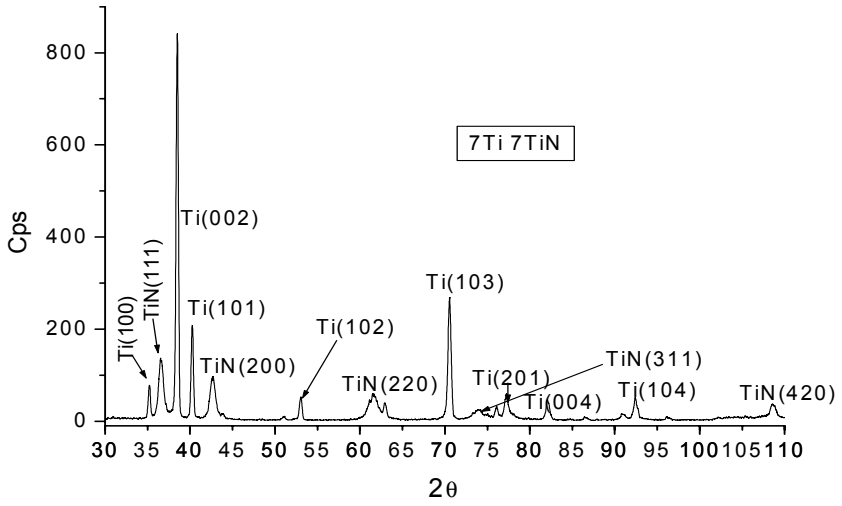

Figure 13. XRD pattern of the sample with 14 layers.

4. CONCLUSIONS

Relatively thick (0.75 μm) TiN-Ti multilayers can be used to significantly improve the corrosion resistance of 304 SS substrates. The corrosion resistance was found to be dependent on the number of layers in the coating. The improvement in the corrosion resistance was seen to be mainly through a strong reduction in the attack by pitting. The layers with a period of about 300 nm, deposited using different magnetic fields, showed that the corrosion resistance is strongly dependent on the degree of ion bombardment during growth and increased, when the degree of bombardment is high. The interplanar distance is influenced by the changes in the ion bombardment caused by the magnetic field.

ACKNOWLEDGEMENTS

The authors wish to acknowledge the support of R. Cuéllar in maintaining and operating the accelerator. This work has been supported by IAEA contract. No. 11365.

REFERENCES

[1] FONTANA; M.G., Corrosion engineering, Mc Graw Hill, (1986) 92.

[2] HUBLER, R., Characterisation of gradient interfaces in thin film multilayers used to protect orthopaedic implants, Surf. Coat. Technol. 116–119 (1999) 1116.

[3] RIES, L.A.S., ASAMBUJA, D.S., BAUMVOL, I.J.R., Corrosion resistance of steel coated with Ti/TiN multilayers, Surf. Coat. Technol. 89 (1997) 114.

[4] SANT, C., DAIA, M.B., AUBERT, P., LABDI, S., HOUDY, P., Interface effect on tribological properties of titanium–titanium nitride nanolaminated structures, Surf. Coat. Technol. 127 (2000) 167.

[5] FLORES, M., MUHL S., ANDRADE, E., The relation between the plasma characteristic and the corrosion properties of TiN/Ti multilayers deposited by unbalanced magnetron sputtering, Thin Solid Films 433 (2003) 217.

[6] MUSIL, J., KADLEC, S., VALDOVA, V., KUZEL, R., CERNY, R., Surf. Coat. Technol. 43–44 (1990) 259.

[7] THORTON, J.A., Influence of apparatus geometry and deposition conditions on the structure and topography of thick sputtered coatings, J. Vac. Sci. Technol. 11 (4) (1974) 666.

[8] MESSIER, R., GIRI, A.P., ROY, R.A., Revised structure zone model for thin film physical structure, J. Vac. Sci. Technol. A2 (2) (1984) 500.

[9] ARNELL, R.D., KELLY, P.J., Recent advances in magnetron sputtering, Surf. Coat. Technol. 112 (1999) 170.

[10] ANDRADE, E., Ion beam analysis at the University of Mexico, Nucl. Instr. Meth. B56–57 (1991) 802.

[11] BARRADAS, N.P., JEYNES, C., WEBB, R.P., Simulated annealing analysis of Rutherford backscattering data, Appl. Phys. Lett. 71 (1997) 291.

A ROUND ROBIN CHARACTERIZATION OF THE THICKNESS AND COMPOSITION OF THIN TO ULTRA-THIN ALUMINUM OXYNITRIDE FILMS

N.P. Barradas
Instituto Tecnológico e Nuclear, Portugal

Abstract

A round-robin exercise involving 16 laboratories was undertaken to test the capabilities of various analytical techniques to determine the composition and thickness of thin to ultra-thin AlO_xN_y films. Both accelerator-based, ion beam analytical techniques and non-nuclear techniques of analysis were used by participating laboratories. The accelerator-based techniques were found to able to provide the required information, as opposed to non-nuclear techniques. There is good agreement between the results reported by accelerator laboratories.

1. INTRODUCTION

AlO_x, AlN_x and AlO_xN_y thin layers are used as insulating layers in spin-dependent tunnel junctions for magnetic read heads and non-volatile memories based on the spin-dependent electron tunnelling magnetoresistance (TMR) effect. TMR values higher than 40% at room temperature have been obtained with resistance-area products down to a few hundred $\Omega\times\mu m^2$ [1–3]. The TMR effect is a change of the junction resistance when an external magnetic field is applied with a correspondent change in the tunnelling current.

The properties of these junctions are strongly influenced by the quality of the insulating layer. As these layers have thicknessess typically smaller than 20 Å, determining their exact composition is a challenge for both IBA and non-nuclear techniques. Determination of the N and O content in very thin layers is at the border of their capabilities, and hence constitutes a very interesting test case, defining the scope for optimisation of the different techniques used in different labs. This round robin exercise was organized to ascertain the strengths and weaknesses of different analytical techniques, in determining the composition of thin to ultra-thin AlO_xN_y films.

2. SAMPLE PREPARATION

The samples were deposited by reactive magnetron sputtering at INESC, Lisbon, in the period 6–17 November 2000, using a Nordiko 3000 ion beam system with a base pressure of 4.5×10^{-8} mbar. (001) Si wafers (previously etched) with 6'' diameter were used. The nominal structures deposited were:

Wafer #1 etch/ Ta 20Å/ AlN 9Å/ Au 20Å
Wafer #2 etch/ Ta 20Å/ AlNO 9Å/ Au 20Å
Wafer #3 etch/ Ta 20Å/ AlNO ~100Å/ Au 20Å
Wafer #4 etch/ Ta 20Å/ AlNO ~1000Å/ Au 20Å (Au layer contaminated)
Wafer #5 etch/ Ta 20Å/ AlN 9Å/ Au 20Å (nominally equal to #1)
Wafer #6 etch/ Ta 20Å/ AlNO ~1000Å/ Au 20Å (nominally equal to #4)

The Si surface was ion milled for 1 min prior to the Ta layer deposition to remove the SiO_2 layer. Ion milling conditions: 65 W, +500V extraction, -200V deceleration, 8 sccm Ar, beam/sample surface angle = 70º. In wafers 1, 2 and 5, the AlN and AlNO layers were prepared by oxidation/nitridation of a metallic Al layer nominally 9 Å thick with the following parameters:

Al deposition	deposition gun: 100W, +1450V, -300V, 1 sccm Xe, 33 mA
Wafer #1	nitridation 200s, 110W, +0V, -0V, 10 sccm Ar, 25 sccm N_2
Wafer #2	oxi-nitridation 15s, 110W, +0V, -0V, 4 sccm Ar, 15 sccm N_2, 20 sccm O_2

For wafers 3, 4 and 6 the AlNO layer was prepared by assisted deposition of the Al (reactive deposition) with the following parameters:

Deposition gun (for the Al): 100W, +1450V, -300V, 1 sccm Xe, 33 mA
Assist gun (for the N and O): 50W, +200V, -100V, 10sccm Ar, 6 sccm N_2, 1.5 sccm O_2

There was Ag contamination in the Au film in wafer #4. On opening the chamber, there was a hole on the Au foil target with exposed Ag glue. The resistivity of wafer #1 was mapped prior to photoresist deposition. The resistivity is an exponential function of the thickness deposited. Across the wafer the uniformity in resistivity is 11.5%. In the central 5×5 cm^2 used for the round robin, it is 2.2%. It is hence expected that thickness uniformity on the layer thickness in wafers #1 and #2 is better than 2.2%, and considerably better in wafers #3 and #4.

All wafers were cut into 1x1 cm^2 squares using a DISCO DAD321 automated saw. Only the inner part of the 6" wafer was used. Each square was introduced in an individual labeled box immediately after cutting. The wafer surface was protected with 1.5 μm of photoresist (which is removed by agitation for 1 min in an ultrasonic acetone bath). The exact location of each sample within the wafer was identified for each participating laboratory.

3. DATA COLLECTION AND EVALUATION

The data measurements and analyses made on each sample was the responsibility of the participating laboratories. The experimental methods and data analysis procedures used are described in the reports received at ITN. Of the 25 laboratories that expressed their wish to participate, 16 reports have been received. Table 1 lists a summary of the IBA techniques actually used by the different groups. The identity of the participants is kept undisclosed.

Table 1. List of analytical techniques used by participating laboratories

participant	HI-ERDA	RBS	HI-RBS	EBS	MEIS	NRA	PIXE	PIGE	AES	SIMS	AFM
h8	mag spec										
e9		channelling									
e6		+		+							
j/f6	ToF										
h6	ToF						+	+			
f/j9									+		
j/f7										500eV Cs^+ at 60°	
j/f8		mag spec									
i7		+				$^{14}N(d,\alpha)^{12}C$ $^{16}O(d,p)^{17}O$					
g6		+	+	+							
h9	+										+
g8		+			+						
g9		+				$^{18}O(p,\alpha)^{15}N$ $^{15}N(p,\alpha\gamma)^{12}C$ $^{27}Al(p,\gamma)^{28}Si$					
g10	E-□E		+								
j10										+	
i10		channelling				$^{14}N(d,\alpha)^{12}C$ $^{16}O(d,p)^{17}O$					

One should note that the techniques originally proposed by laboratories expressing their interest in this round robin experiment are listed in Table 2. By comparison between those techniques initially proposed and those actually used, we can see that all IBA techniques proposed were effectively utilized, except LEIS. On the other hand, most of the non-IBA methods initially proposed were not utilized. Several of the laboratories that had proposed to use exclusively non-IBA methods in the end did not participate in the round robin. Only three labs used exclusively non-IBA methods. Not knowing the reasons for this, it is nevertheless an indication that at least for the system studied, IBA is highly competitive. Non-IBA methods appear to have difficulties in providing the required information.

Table 2. List of all analytical techniques initially proposed by the participants

IBA Methods	***Non-IBA methods***
RBS	SIMS (standard, TOF, quadrupole)
EBS	XPS
ERDA (heavy ion, TOF, gas-ionisation)	AES
Mass resolved low energy ion scattering (LEIS)	X-ray diffraction (XRD)
Medium energy ion scattering	X-ray fluorescence (XRF)
NRA	FTIR
PIXE	ellipsometry
PIGE	various microscopies

4. SUMMARY OF RESULTS: STOICHIOMETRY OF ALUMINUM OXYNITRIDE FILMS

The results reported by the participating laboratories are listed in Tables 3 – 6. The standard deviations quoted are given in parenthesis against the sample identification. The calculated overall averages and their uncertainties are obtained by excluding the largest and lowest values of each sample measurement.

Table 3. Sample S1

Sample	t (at/cm^2)	t (Å)	Al (at/cm^2)	N (at/cm^2)	O (at/cm^2)	Al (at.%)	N (at.%)	O (at.%)
S1 - h8				1.23 (8)	19.1 (5)			
S1 - e9	31 (9)		12.9 (1.6)	1.7 (5.5)	16.0 (2.3)	42.2 (14.0)	5.5 (18.1)	52.3 (17.7)
S1 - e6								
S1 - j6	33 (3)		11.4 (1.3)	1.98 (0.2)	15 (0.7)	34.65 (4)	6.0 (6)	45.5 (2.0)
S1 – h6								
S1 - f9		10 (2)						
S1 - j7								
S1 - j8	*							
S1 - i7			-	2.47 (0.17)	15.8 (8)			
S1 - g6	23.7 (0.7)	23.5	7.65	1.19	13.91	32.3 (0.3)	5.0 (0.8)	58.7 (4.0)
S1 - h9								
S1 - g8								
S1 - g9	50	42		<1		39.4	0	59.2
S1 - g10	34.3 (4.0)		4.1 (0.9)	3.6 (1.0)	26.6 (3.7)	12 (3)	11 (3)	78 (4) *
S1 - j10								
S1 - i10	16		5.25	1.84	7.87	32.8	11.5	49.2
Average	30.5 (4.7)		8.1 (3.1)	1.73 (48)	16.0 (1.9)	34.8 (3.2)	6.9 (2.8)	54.9 (4.9)

Table 4. Sample S2

Sample	t (at/cm^2)	t (Å)	Al (at/cm^2)	N (at/cm^2)	O (at/cm^2)	Al (at.%)	N (at.%)	O (at.%)
S2 - h8				0.30 (2)	19.5 (5)			
S2 - e9	35 (7)		11.3 (3.0)	4.9 (2.3)	18.8 (2.1)	32.3 (10.9)	14 (7)	53.7 (12.8)
S2 - e6								
S2 - j6	34 (8)		9 (1.2)	0.57 (.06)	15.3 (0.9)	30 (4)	1.9 (2)	51 (3)
S2 - h6								
S2 - f9		9 (2)						
S2 - j7								
S2 - j8								
S2 - i7			-	0.58 (0.05)	17.0 (9)			
S2 - g6	23.8 (0.5)	23.7	7.14	1.31	14.3	30 (3)	5.5 (0.5)	60.0 (5.0)
S2 - h9								
S2 - g8								
S2 - g9	50	42		<1		39.4	0	59.2
S2 - g10	21.1 (3.2)		3.2 (0.9)	2.5 (0.9)	15.4 (2.9)	15 (4)	12 (4)	73 (6) *
S2 -j10								
S2 - i10				0.5 (2)		50	50	
Average	30.9 (6.2)		7.7 (3.4)	1.0 (8)		32.9 (4.5)	8.3 (5.6)	57.6 (3.4)

Table 5. Sample S3

Sample	t (at/cm^2)	t (Å)	Al (at/cm^2)	N (at/cm^2)	O (at/cm^2)	Al (at.%)	N (at.%)	O (at.%)
S3 - h8	241 (17)		109	8.5(3)	124 (2.6)	45.2	3.3	51.5
S3 - e9	212 (5)		77.9 (1.2)	7.1 (1.6)	116.1 (1.5)	36.8 (1.0)	3.3 (8)	54.9 (1.4)
S3 - e6	600					85 (21)		14.5 (1.0)
S3 - f6	210 (21)		74.6 (4.2)	10.5 (0.6)	112 (4.2)	35.5(2.0)	5.0 (3)	53.4(2.0)
S3 - h6	123±25%		46	5	72	37.0±20%	4.1±10%	58.9±10%
S3 - j9		102 (20)						
S3 - f7								
S3 - f8								
S3 - i7			-	9.13 (0.64)	126 (6)			
S3 - g6	211 (11)	210.0	71.9	13.3	108.0	34.1 (4.0)	6.3 (1.0)	51.2 (5)
S3 - h9						35 (2)	3.6 (3)	51 (2)
S3 - g8	150	300				42.0	4.1	50.1
S3 - g9	217	185		<1		39.4	0	59.2
S3 - g10	269 (41)		93 (21)	14 (5)	162 (35)	35 (7)	5.2 (1.9)	60 (7)
S3 - j10		260 (20)						
S3 - i10	160		58.6	4.4	87.9	36.6	2.7	54.9
Average	209 (39)	218 (38)	75 (12)	8.3 (3.1)	112 (14)	38.1 (3.5)	3.9 (9)	53.9 (3.4)

Table 6. Sample S5

Sample	t (at/cm^2)	t (Å)	Al (at/cm^2)	N (at/cm^2)	O (at/cm^2)	Al (at.%)	N (at.%)	O (at.%)
S5 - h8	2144 (129)		945	52 (1.5)	1147 (25)	43.9	2.6	51.1
S5 - e9	1943 (30)		641 (5)	126 (12)	1098 (11)	33.0 (6)	5.2 (2.6)	57.5 (3.0)
S5 - e6	2300					50 (2)	1.0 (4)	50.0 (5)
S5 - j6	1775 (177)		607 (18)	52.7 (0.3)	934 (18)	34.2 (1.0)	2.97 (15)	52.6 (1.0)
S5 - h6	2078±25%		830	58	1190	40±20%	2.8±10%	57.2±10%
S5 - j9		830 (170)						
S5 - j7								
S5 - j8								
S5 - i7	1901		687 (0.3)	51.4 (5.0)	1090 (50)	36.1	2.70	57.3
S5 - g6	1926 (80)	1918	611	94	1219	31.7 (0.5)	4.9 (1.5)	63.3 (1.0)
S5 - h9	2093 (107)	1600 (100)	740 (30)	57 (3)	1120 (50)	34.6 (2)	2.7 (1)	52.7 (3)
S5 - g8	1473.4	4110 (120)				33.0	19.6	45.2
S5 - g9	1833	1560		<1		39.4	0	59.2
S5 - g10	2300 (300)		890 (180)	72 (22)	1370 (270)	38 (6)	3.1 (1.0)	59 (7)
S5 -j10								
S5 - i10	1895		723	-	1085	38.2	-	57.3
Average	1989 (161)	1692 (196)	732 (100)	62 (16)	1136 (52)	37.0 (3.5)	3.1 (1.3)	55.4 (3.4)

5. CONCLUSIONS

Most of the results reported are not statistically different from the reference values, taken as the median of all observations. Only seldom, are large deviations observed. This observation demonstrates the capability of IBA techniques to quantitatively analyse this very demanding system. Only about half of the participants could measure the ultra-thin films, which pose a severe challenge for any analytical technique, and several of the participants had to utilize their facilities close to their sensitivity and resolution limits. However, it was not possible to identify a given technique, or a group of techniques, as being the preferred method for analysing the ultra-thin samples. Unexpected deviations in some results reflect a need for further measurements of fundamental quantities, namely cross-sections and stopping powers, in energy ranges useful for IBA. Furthermore, precise measurements of beam fluence and detector solid angle would lead to improvements in the accuracy of some of the quantities reported, particularly areal densities.

REFERENCES

[1] SOUSA, R.C., SUN, J.J., SOARES, V., FREITAS, P.P., KLING, A., DA SILVA, M.F., SOARES, J.C., Large tunneling magnetoresistance enhancement by thermal anneal, Appl. Phys. Lett. 73 (1998) 3288.

[2] SUN, J.J., SOARES, V., FREITAS, P.P., Low resistance spin-dependent tunnel junctions deposited with a vacuum break and radio frequency plasma oxidized, Appl. Phys. Lett. 74 (1999) 448.

[3] PARKIN, S.S.P., ROCHE, K.P., SAMANT, M.G., RICE, P.M., BEYERS, R.B., SCHEUERLEIN, R.E., O'SULIVAN, E.J., BROWN, S.L., BUCCHIGANO, J., ABRAHAM, D.W., LU, Y., ROOKS, M., TROUILLOUD, P.L., WANNER, R.A., GALLAGHER, W.J., Exchange-biased magnetic tunnel junctions and application to nonvolatile magnetic random access memory, J. Appl. Phys. 85 (1999) 5828.

DEVELOPMENT OF ARTIFICIAL NEURAL NETWORKS FOR THIN $AL_xN_yO_z$ FILMS MEASURED BY RUTHERFORD BACKSCATTERING

N.P. Barradas, A. Vieira, V. Matias, G. Öhl, J.C. Soares
Instituto Tecnológico e Nuclear, Portugal

S. Cardoso, P.P. Freitas
INESC, Lisbon, Portugal

Abstract

The performance of artificial neural networks on RBS analysis of spectra from AlN_xO_y thin films deposited on silicon substrates was investigated. After training, the networks were applied to real spectra. The results obtained were very close to those using the traditional, time-consuming methods. Artificial neural networks outperformed other methods when applied to differentiated data.

1. INTRODUCTION

Thin films of AlN_xO_y are being used as insulating barriers between metallic layers of spin-tunnel-junctions for advanced reading and recording devices [1–4]. RBS analysis of these films is not an easy task [5–7]. Relevant signals from N and O are small and superimposed on a large Si background, and the Al signal is also partially superimposed on a Si background.

Here we describe the results of applying Artificial Neural Networks (ANN) to the analysis of RBS spectra. The basic ANN structure was adapted in order to deal with the different data manipulation necessary to tackle this problem, namely smoothing and differentiation necessary to improve the signal — background ratio. To evaluate the ANN results, we assume as reference the values obtained with the usual method for RBS spectra analysis, namely the peak integration method and the step height analysis [8].

2. EXPERIMENTAL DETAILS

We prepared two sets of samples grown on (100) silicon single crystals. The first set, composed of three samples (1–3) had the nominal composition AlN. Small amounts of oxygen present in the chamber were incorporated in the samples during preparation. This set was prepared by reactive magnetron sputtering of an Al target in a Nordiko7000 system. Samples 1 and 3 had a nominal thickness of 1000×10^{15} at/cm^2 and sample 2 has 500×10^{15} at/cm^2. The second set is composed of two samples, 4 and 5 with nominal composition Al_2O_3 and nominal thicknesses of 200×10^{15} at/cm^2 and 1500×10^{15} at/cm^2. They were prepared by ion beam sputtering of an Al target in a Nordiko3000 system, using an Ar-O beam during the deposition.

The RBS analysis was performed using a He^+ beam at the ITN 3 MV Van de Graaff accelerator. We used beam energies between 1.0 and 1.9 MeV, and angles of incidence θ_{inc} between 0º and 30º. We used an annular surface barrier detector in the IBM geometry placed

at about 180º to the incident beam direction. The energy resolution of the system is 26 keV at full width half maximum (FWHM). The product of detector solid angle with the analyzing beam fluence was between 2.6 and 315.6 μC msr.

3. ARTIFICIAL NEURAL NETWORKS

The network architecture is defined by the size of the input layer, the number of hidden layers and the output layer. The input layer receives the RBS spectrum data to be analyzed along with some experimental parameters related to the spectrum, namely, the beam energy, angle of incidence and deposited charge. At the output layer, containing four nodes, the three elements concentrations and the film thickness are presented. Although the RBS spectra used for training have 512 channels, we only used 207 channels, where the Al, O and N signals are relevant. The input layer has therefore 210 nodes covering the three experimental parameters. All ANNs have three hidden layers containing 80, 40 and 20 nodes.

We used four ANNs, one dedicated to raw data analysis ($ANN_{Raw,}$), another dedicated to the smoothed data ($ANN_{Smoothed}$), one dedicated to the analysis of the smoothed and differentiated data ($ANN_{Differentiated}$), and finally one equal to the previous, but without information of experimental conditions ($ANN_{No\_exp\_Param}$). The architecture of the networks is (N, 80, 40, 20, 4) with N = 210 for ANN_{Raw}, $ANN_{Smoothed}$ and $ANN_{Differentiated}$, and N=207 for $ANN_{No\_exp\_Param}$.

To teach the ANNs, we fed them with a large set of RBS examples, called the training set, and another smaller independent set to test their performance — the test set. We take particular care to build a training set composed by a sufficiently large and representative set of examples that adequately represent all possible experimental situations. We used a computational model to obtain 20 000 simulated experimental data, to which we added realistic Poisson noise in order to simulate the statistical fluctuation associated to experimental data. The spectra obtained were initially supposed to cover all the experimental conditions we used to analyze our samples, namely, beam energy between 1 and 2 MeV, angle of incidence between -40º and 40º, charge-solid angle product between 52.4 and 393 μC msr, film thickness between 150 and 850×10^{15} at/cm^2, Al atomic concentration between 19 and 77%, O and N atomic concentrations between 0 and 68%. In fact, sample 5 is thicker than the upper limit in these training data, and in a few cases the analyzing beam fluence was lower than the lower limit used. This provides us with cases where the limitations of the ANNs developed can be tested.

To simulate the channeling in Si, we used a zeroth order approximation, which consisted of multiplying the Si signal with a constant between 0 and 1. This ignores the fact that the yield reduction due to channeling depends on the beam energy, on the probed depth, and on the exact orientation of the crystal relative to the incident beam [8].

Since these spectra are composed of small signals on top of a large background signal, we had to develop numerical transformations to better expose the relevant signals. First we smoothed the raw data in order to reduce statistical fluctuations. This proved to be ineffective as is seen by comparing the raw and smoothed data in Figure 1.

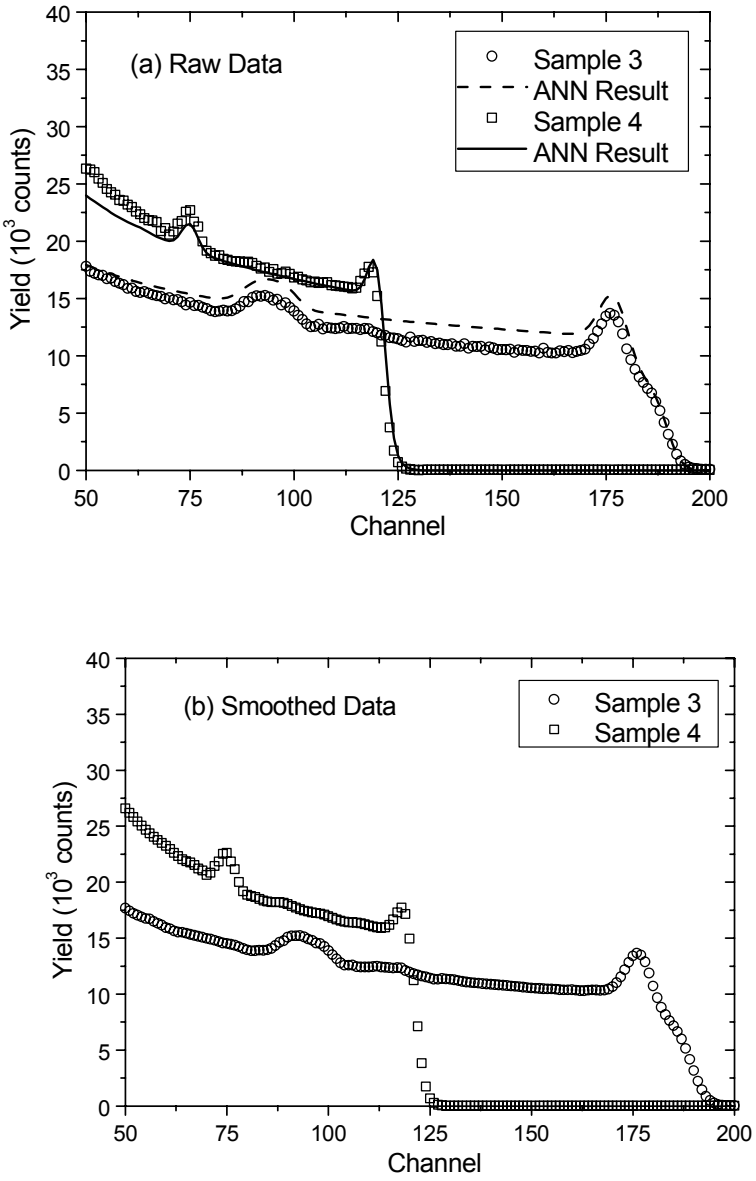

Figure 1. RBS spectra of samples 3 and 4. (a) Raw data. The solid lines are results obtained with $ANN_{Differentiated}$*. (b) Smoothed data.*

Since the O, N and Al peaks change rapidly, while the Si background signal is nearly constant, the relevant signals should be enhanced by smoothing and differentiating the raw data spectra. Figure 2 shows two examples of differentiated spectra.

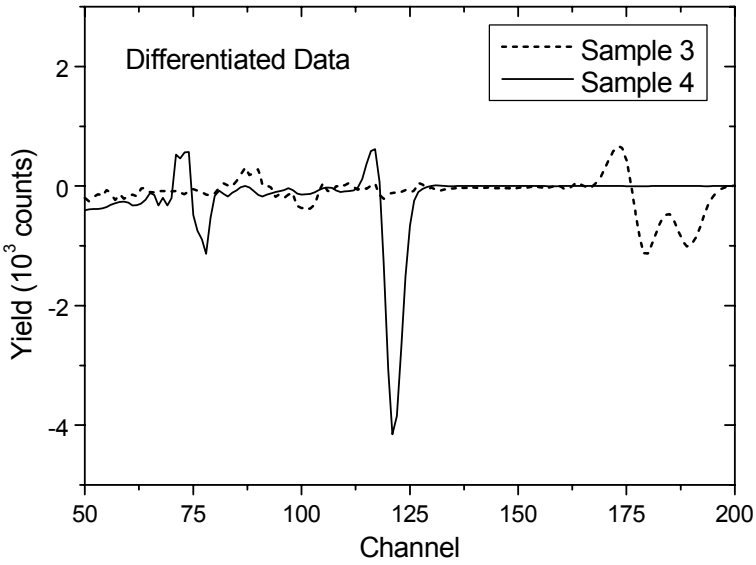

Figure 2. Spectra from the differentiated raw data for samples 3 and 4.

From the set of simulated experimental RBS spectra, 18,000 simulations were used to train the network, while the other 2,000 were used to test the network, not having been used for training. For each example, the corresponding output is compared with the output evaluated by the ANN. The calculated error, a mean squared error (MSE), between the ANN result and the expected result is used as a control tool to adjust the weights between the nodes during the feedforward backpropagation learning process. During the training and test stages, after a few iterations, all cases with a MSE larger than 40% are excluded from both sets, as can be seen in Figure 3 around iteration 50. The MSE evolution with the iterations is shown in this figure for the training and test sets.

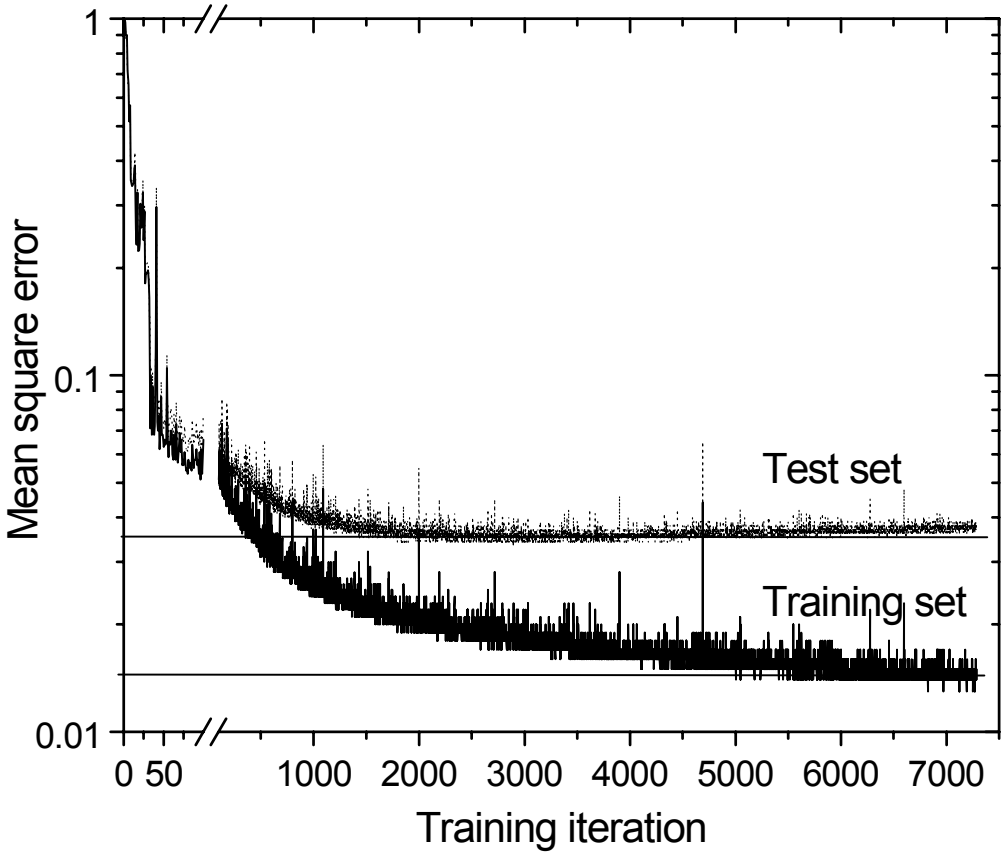

Figure 3. Mean square error evolution with the training iteration. Overfitting starts around iteration 2000, where the error on the training set continues slowly to improve, but the error on the test set settles around the same value and starts to worsen after some iterations, as can be verified around iteration 5000.

The learning process should be stopped to avoid overfitting. This point is achieved when the test set error starts to increase, as can be seen in Figure 3 after iteration 3,000. The final weights taken are those for which the test set error is smallest. Table 1 shows the final MSE for the training and test sets for each ANN. In all cases they are rather small, indicating that the networks could generalize well the patterns in the data. The errors are smallest for ANN_{Raw}, comparable for $ANN_{Smoothed}$ and $ANN_{Differentiated}$, and largest for $ANN_{No\_exp\_Param}$. Note that these errors are only an indication of the performance of ANNs on the trained data. The real test is their performance on *real* experimental data.

Table 1. Mean squared errors in the training and test sets for all the studied networks

Network	Train set MSE (%)	Test set MSE (%)
ANN-Raw	2.2	2.8
ANN-Smooth	2.9	3.7
ANN-Differentiated	2.4	3.4
ANN-No_Exp._Param	3.1	4.3

4. RESULTS AND DISCUSSION

We trained and tested the ANNs to analyze the RBS data from our samples. In all cases the results were compared with reference values obtained by applying the peak integration method [8]. A comparison between the four networks is presented in Table 2. To evaluate the quality of each network, the ratio between the ANN result and the reference value is calculated for each sample. The ANN result was taken to be the average of the results obtained for all the spectra measured from each given sample. The standard deviation of the ratio values is also shown in the table since it reflects the stability of the ANN against variation of experimental conditions. Even for an average ratio of 1, a high standard deviation would mean that the ANN performs poorly.

We see that the results from all ANNs are in general good and fairly similar. The most important exception is sample 5, where all ANNs perform poorly. This can be explained by the fact that the film thickness (nominally 1500×10^{15} at/cm^2) is significantly above the maximum value used to train the ANNs (850×10^{15} at/cm^2), which means that this sample is outside the range where the generalizations capabilities of the ANNs are valid. This shows that the representativeness of the training data is a determinant factor of the reliability of ANN predictions.

The similarity of results obtained with ANN_{Raw} and $ANN_{Smoothed}$ indicates that the network analysis did not improve much by smoothing the raw data. Smoothing could reduce slightly some noise, but since the relevant signals remain small, the improvement should not be significant.

However, differentiation of the data proved to be very effective in outlining the O and N peaks. This explains the better results obtained with $ANN_{Differentiated}$ in most cases. This is particularly true for the smallest signals, which are the O concentration in samples 1 to 3, and the N concentration in sample 4, where $ANN_{Differentiated}$ outperforms ANN_{Raw} and $ANN_{Smoothed}$ both with respect to the average result and in the standard deviation. This shows clearly that the differentiation was highly successful in enhancing small signals and reducing the influence of the background.

The results obtained with $ANN_{No\_exp.\_Param.}$ are comparable with the ones obtained with $ANN_{Differentiated}$, but less accurate. This indicates that, even without the information on the experimental parameters, the network structure is versatile enough to recognize the relevant patterns for the analysis.

A comparison between the raw data and a simulation done with the $ANN_{Differentiated}$ results for samples 3 and 4 is shown in Figure 1 (a). For sample 4, the results from the ANN are very close to the raw data, meaning that the analysis performed by the network was successful. For sample 3, at first sight the analysis was less successful, because the simulated yield is higher than the experimental yield. However, this is due to channeling in the Si crystal which occurred in the experiment, but was not taken into account in the simulation. This does not affect the signal of the Al, N and O, or the shape and height of those peaks. Results from ANN are very close to the raw data, which indicates that the analysis is correct. This is also confirmed by the excellent values of thickness and concentration obtained with $ANN_{Differentiated}$ for this spectrum.

Table 2. Average and standard deviation σ (between brackets) for the ratio between the ANN values and the reference values for the film thickness.

Sample	ANN	Thickness	[Al]	[N]	[O]
1	Raw	0.92 (0.12)	0.87 (0.08)	1.17 (0.08)	0.75 (0.5)
	Smoothed	0.92 (0.12)	0.85 (0.08)	1.2 (0.08)	0.78 (0.5)
	Differentiated	0.94 (0.16)	0.94 (0.1)	1.07 (0.1)	1.1 (0.3)
	No exp. Param.	0.84 (0.19)	0.83 (0.08)	1.14 (0.09)	1.66 (0.78)
2	Raw	1.14 (0.18)	0.76 (0.17)	1.19 (0.09)	1.5 (1.31)
	Smoothed	1.4 (0.18)	0.77 (0.2)	1.17 (0.07)	1.59 (1.24)
	Differentiated	1.06 (0.08)	1.01 (0.08)	1.02 (0.08)	0.79 (0.34)
	No exp. Param.	1.09 (0.15)	0.98 (0.11)	1.04 (0.11)	0.79 (0.26)
3	Raw	0.91 (0.17)	0.95 (0.13)	1.12 (0.13)	0.51 (0.88)
	Smoothed	0.9 (0.15)	0.93 (0.11)	1.1 (0.15)	0.85 (0.86)
	Differentiated	0.88 (0.15)	0.99 (0.12)	1.04 (0.1)	0.86 (0.3)
	No exp. Param.	0.86 (0.12)	0.93 (0.14)	1.09 (0.11)	0.92 (0.51)
4	Raw	1.14 (0.21)	0.83 (0.09)	7.16 (0.64)	0.75 (0.15)
	Smoothed	1.1 (0.2)	0.89 (0.1)	6.91 (0.63)	0.73 (0.16)
	Differentiated	0.82 (0.17)	1.13 (0.1)	1 (0.27)	0.98 (0.07)
	No exp. Param.	0.82 (0.16)	0.95 (0.09)	1.3 (0.31)	1.09 (0.08)
5	Raw	0.08 (0.03)	1.27 (0.12)	16.82 (1.72)	0.01 (0.04)
	Smoothed	0.11 (0.07)	1.09 (0.1)	19.1 (1.83)	0.01 (0.05)
	Differentiated	0.1 (0.03)	1.38 (0.11)	15.21 (1.64)	0.04 (0.01)
	No exp. Param.	0.1 (0.01)	1.7 (0.19)	10.29 (4.59)	0.09 (0.02)

5. CONCLUSIONS

We studied the performance of artificial neural networks on the difficult problem of RBS analysis of spectra from AlN_xO_y thin films deposited on Si substrates. After training the networks, we applied them to real experimental RBS spectra obtained from four samples measured in different experimental conditions. The results were very close to reference values obtained with traditional time-consuming methods. The ANN for the differentiated data performed better than the other ones because the signal from the slowly varying Si background is minimized. The ANN with no knowledge on the experimental conditions also performed well, although slightly worse, because it could extract from the data itself the information required to do a valid analysis.

REFERENCES

[1] CARDOSO, S., FREITAS, P.P., DE JESUS, C., WEI, P., SOARES, J.C., Spin-tunnel-junction thermal stability and interface interdiffusion above 300 °C, Appl. Phys. Lett. 76 (2000) 610.

[2] TEHRANI, S., SLAUGHTER, J.M., CHEN, E., DURLAM, M., SHI, J., DE HERRERA, M., Progress and outlook for MRAM technology, IEEE Trans. Magnetics 35 (1999) 2814.

[3] KUIPER, A.E.T., GILLIES, M.F., KOTTLER, V., HOOFT, G.W., VAN BERKUM, J.G.M., VAN DER MAREL, C., TAMMINGA, Y., SNIJDERS, J.H.M., Plasma oxidation of thin aluminium layers for magnetic spin-tunnel junctions, J. Appl. Phys. 89 (2001) 1965.

[4] BOEVE, H., GIRGIS, E., SCHELTEN, J., DE BOECK, J., BORGHS, G., Strongly reduced bias dependence in spin–tunnel junctions obtained by ultraviolet light assisted oxidation, Appl. Phys. Lett. 76 (2000) 1048.

[5] BRIJS, B., DELEU, J., CONARD, T., DE WITTE, H., VANDERVORST, W., NAKAJIMA, K., KIMURA, GENCHEV, I., BERGMAIER, A., GOERGENS, L., NEUMAIER, P., DOLLINGER, G., DÖBELI, M., Characterization of ultra thin oxynitrides: A general approach, Nucl. Instr. Meth. B161-163 (2000) 429.

[6] CHENG, L.L., YU, Y.H., SUNDARAVEL, B., LUO, E.Z., LIN, S., LEI, Y.M., REN, C.X., CHEUNG, W.Y., WONG, S.P., XU, J.B., WILSON, I.H., Compositional and morphological study of reactive ion beam deposited AlN thin films, Nucl. Instr. Meth. B169 (2000) 94.

[7] WALKER, S.R., DAVIES, J.A., MASCHER, P., WALLACE, S.G., LENNARD, W.N., MASSOUMI, G.R., ELLIMAN, R.G., OPHEL, T.R., TIMMERS, H., Characterization of silicon oxynitride films using ion beam analysis techniques, Nucl. Instr. Meth. B170 (2000) 461.

[8] TESMER, J.R., NASTASI, M. (Eds.), Handbook of Modern Ion Beam Analysis, Materials Research Society, Pittsburg, USA (1995).

DETERMINATION OF THE STOPPING POWER OF ^{4}He USING BAYESIAN INFERENCE WITH THE MARKOV CHAIN MONTE CARLO ALGORITHM

N.P. Barradas
Instituto Tecnológico e Nuclear, Portugal

C. Pascual-Izarra, A. Climent-Font
UAM, Madrid, Spain

M. Bianconi
CNR-IMM-Sezione di Bologna, Bologna, Italy

Abstract

A new method for the experimental determination of stopping powers based on Bayesian Inference with the Markov chain Monte Carlo (MCMC) algorithm has been devised. This method avoids the difficulties related to thin target preparation. By measuring the RBS spectra for a known material, and using the known underlying physics, the stopping powers are determined by best matching the simulated spectra with the experimental spectra. Using silicon, SiO_2 and Al_2O_3 as test cases, good agreement is obtained between calculated and experimental data.

1. INTRODUCTION

The energy loss per unit path length dE/dx is known as the stopping $S[E(x)]$. Many measurements of these energy loss values have been made, for many incident beams and targets, leading to a spread of values up to 10%. A database parameterising the periodic table has long been available [1]. The accuracy with which the stopping powers are known is currently rather poor. As an example, there were 10% errors even for the technologically important element silicon until very recently [2]. The main reason for this poor accuracy is that the experimental determination of stopping powers by traditional methods is difficult, involving preparation of pure thin targets and accurate measurements of their thicknesses [3]. For a recent evaluation of the current stopping power database, see [4].

We have devised a new method for the experimental determination of stopping powers which avoids all the previous difficulties related to thin target preparation. It involves simply measuring the RBS spectra from known target, which is experimentally trivial. We can then simulate a theoretical spectrum for the known experimental parameters since the physics are well known, apart from the stopping power. Since the experimental parameters are known with well-defined errors, we can fit the stopping powers to obtain a match between the simulated spectrum and the data.

We have developed a code based on Bayesian Inference (BI) with a Markov Chain Monte Carlo (MCMC) algorithm to determine both the stopping powers and the confidence limits on the values calculated.

2. RUTHERFORD BACKSCATTERING

The algorithms for calculating RBS spectra are well covered in the literature, e.g. [2]. Briefly, the energy loss to the incident ion is calculated from the kinematics by determining the energy

loss at the collision, and then integrating the energy loss over the path lengths to the collision and from the collision to the detector. Since the RBS cross-section is given analytically by the Coulomb law, the scattering probability is well known and the whole spectrum can be calculated. However, we make the assumption in this work that no incident ion reaching the detector suffers more than one scattering event, that is, we ignore multiple and plural scattering. We point out below the effect this has on the calculated spectrum.

Parameterizations are based on fitting empirical or semi-empirical formulae to the data available. The most widely used have been those presented by Ziegler and co-workers [4]. Other parameterizations have been presented [3,6–9], which include different amounts of theoretical input and ad-hoc formulas. Theoretical calculations of stopping power have also been formulated [10–12]. In this work we will use the parameterization of ref [5] for the electronic stopping, also used in the well-known code RUMP [13], which uses equation (1) based on 8 parameters to be fitted:

$$S(E) = (SL * SH) / (SL + SH) \quad (1)$$

where

$$SL = a_1 V^{a2} + a_3 V^{a4} \quad (2)$$

$$SH = a_5/V^{a6} \ln (a_7/V + a_8 V) \quad (3)$$

$$V = E / m. \quad (4)$$

3. METHODOLOGY

Suppose that the result of an RBS analysis of a sample gives a spectrum $\mathbf{X}=(X_1,\ldots,X_k)$ where k is the number of channels in the spectrum. This spectrum can be viewed as a stochastic vector, in the sense that it has been contaminated with noise and/or modelling errors. However we assume an underlying deterministic model which depends on a set of quantities $\Theta=(\theta_1,\ldots,\theta_n)$. These include some over which we have some degree of control, such as the beam energy, incident angle, and detector solid angle. It contains known elements such as the sample composition (pure Si). It also contains parameters about which we would like to learn, in this case the stopping power curve *S(E)*. By combining the standard theory of RBS and statistical models of the error mechanisms we can connect $\mathbf{X}$ and Θ into a single statistical model.

We then use Bayesian inference [14] to infer information about the parameters Θ given a statistical model and the observed $\mathbf{X}$. We assume for simplicity independent Poisson noise on the RBS yield. The prior distribution is obtained by conditioning the stopping power curve shape on the parameterisation given by equations (1–4), with a uniform distribution on the a_i parameters.

Computation is done with a Markov Chain Monte Carlo (MCMC) algorithm, according to the Metropolis-Hastings criterion [15]. We calculate the mean solution $\langle\Theta\rangle$ as well as confidence intervals given by the standard deviation $\sigma(\Theta)$. In this case we take the Θ_i to be the stopping power curve.

4. RESULTS AND DISCUSSION

4.1. Silicon

We have previously presented a code based on the Simulated Annealing (SA) algorithm [16], which can automatically analyse RBS and other IBA data, determining depth profiles of the measured samples. It also implemented the BI/MCMC formalism to determine confidence limits on the depth profiles obtained [17,18]. We have now expanded the algorithm to apply BI/MCMC to stopping power values.

The data are shown in Fig. 1, together with the simulations obtained with the nominal experimental parameters and the tabulated stopping power values. The measured yield increases with decreasing energy (channel number) much faster than the simulation. This is due to plural and multiple scattering. We hence only used, for each spectrum, the higher energy portion that is unaffected by these effects.

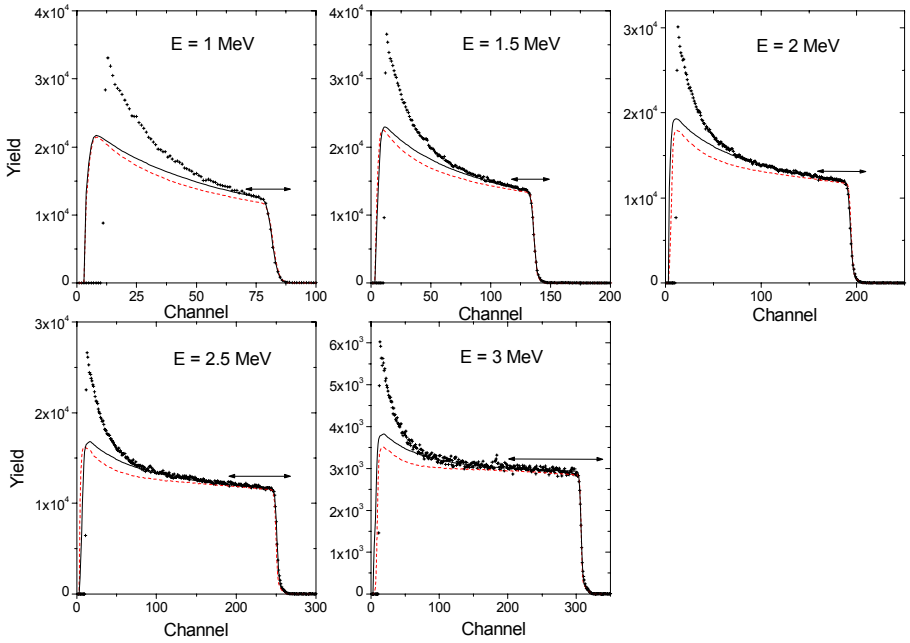

Figure 1. Experimental data (dots) and simulations obtained with the nominal parameters and the tabulated stopping power values (dashed lines). Simulations obtained with the stopping power values of one of the accepted states are also shown (solid lines).

For the data collected for the 1 MeV beam there is a large discrepancy between the data and the simulated spectrum even in the high energy region where no plural and multiple scattering exists. The discrepancy is smaller for larger beam energy. It cannot be accounted for by the small errors in the beam fluence and solid angle of the detector, which are a normalisation factor on the simulation. It must then be due to the stopping power values.

We constructed a Markov chain with 112,000 elements, that is, stopping power data sets up to 3 MeV. Each leads to RBS spectra that fit the five experimental spectra well, as defined by the χ^2 value. Hence the stopping power values determined are consistent with the entire energy range probed.

To test for convergence, plots of moving averages of sample moments against the number of accepted states were used. These plots converge to a constant as equilibrium is reached. To calculate the average and standard deviation of the a_i and of the stopping power curve, we used only the last 100000 elements of the Markov chain.

The results are shown in Fig. 2. The energy regions accessed with each initial beam energy are also shown. For each beam energy two discontinuous energy regions are accessed, corresponding to the energy lost by the beam on its way in, and on the way out. The discontinuity is due to the energy lost in the scattering process itself.

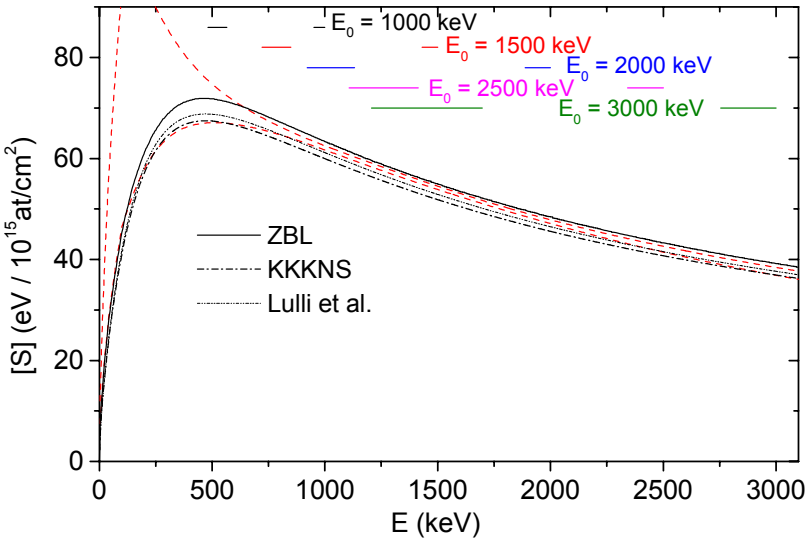

Figure 2. Confidence limits (± 1σ) for the stopping power values (dashed curves). The energy ranges probed with each beam energy are shown.

The confidence limits are narrower where the density of data available is larger, that is, in the energy range 1000–1700 keV. Above, there are fewer energy regions accessed, and the width of the error bars increases. Finally, the minimum energy accessed is 482 keV. Energies below that value are not probed at all, and consequently the confidence limits are much broader.

Both the data of Lennard *et al*, who determined the stopping power values at 0.5, 1, 2 and 3 MeV [2] and those of Lulli *et al*, which have determined the stopping power values at 1.16, 1.5, 2, 3 and 3.7 MeV [19], agree with the data of Konac *et al*. [3] within 2%. Lulli *et al* obtain a better agreement by scaling Konac's data up by a uniform factor of 2%, while Lennard *et al* finds a slightly different energy dependence, with values 1 to 1.5% larger than Konac's data in most of the energy range.

We show the ^{4}He in Si electronic stopping power values obtained by us and by Lulli [19] in Table 1 (Lennard [2] do not quote S_e values directly). We obtain values that are between 2 and 4.5% larger than those of Konac [3].

Table 1. Electronic stopping powers at different beam energies

	S_e (eV/ 10^{15} at/cm^2)					
E_0 (MeV)	0.5	1	1.5	2	2.5	3
This work	70.9 (3.9)	62.10 (41)	54.20 (34)	47.51 (37)	42.03 (58)	37.65 (78)
Lulli.	68.76	61.15	52.88	46.48	41.55	37.66
RUMP	71.8	63.4	54.9	48.4	43.3	39.2
KKKNS	67.41	59.95	51.84	45.57	40.74	36.92

Several energy intervals e.g. [2500, 2754] or [2000, 2341] are not accessed in the experiment but the confidence limits are not significantly broader on these energy ranges because the parameterisation used effectively constrains the stopping power values in the whole energy range.

4.2. SiO_2

A major change is needed in this case relative to the previous one. For Si, the information was derived from the height of the signal in the region where plural scattering does not influence the results, by fitting the data with theoretical spectra based on single-scattering calculations. This is not possible in this case, because the relevant information is in the following signals:

1. Height of the Si surface signal.
2. Height of the O surface signal.
3. Width of the Si signal in the SiO_2 film.
4. Width of the O signal in the SiO_2 film.
5. Shape of the Si and O signals in the SiO_2 film.

The only signal that can be correctly fitted by single-scattering calculations is (1), that does not carry enough information to obtain accurate results. So a different strategy was adopted. The Si signal was multiplied by a 3rd order polynomial to represent the effect of plural scattering. It proceeds as follows: First, we calculated a simulation for ZBL stopping powers and for the nominal film thickness. The result is shown in Fig. 3.

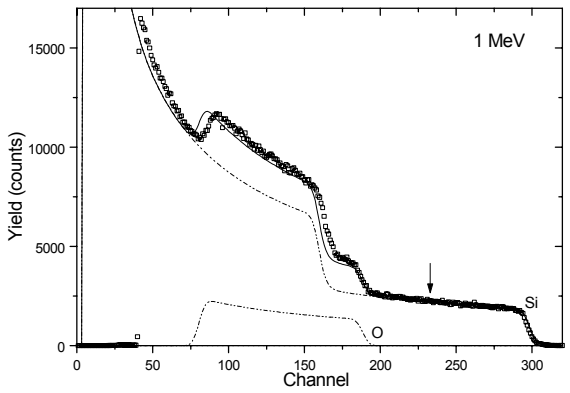

Figure 3. Simulation of SiO_2.

Then we divided the data (from which the partial simulated O signal was subtracted) by the partial simulated Si signal. We eliminated the blips near the interfaces, and obtained the result shown in Fig. 4. This is the polynomial that is then applied to the Si partial signal during the Bayesian inference analysis. However, the polynomial is only applied up to the channel where its value is 1 (240).

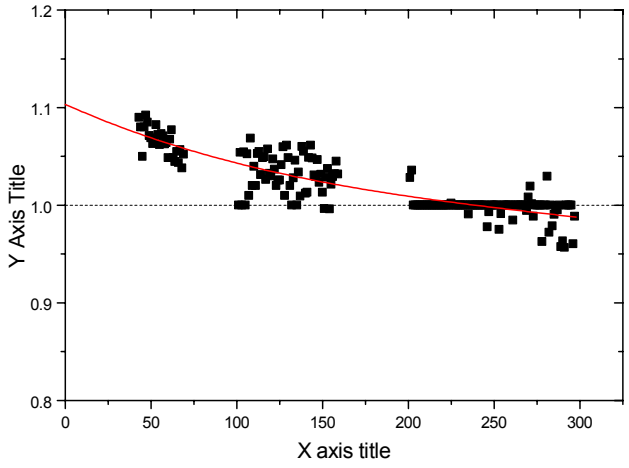

Figure. 4. Ratio of measured to simulated spectrum for SiO_2.

Finally, the calculated stopping powers are shown in Fig. 5 as the ± 1σ confidence limits (dashed curves). The agreement is excellent with the measured stopping powers (solid curve), except at the stopping power maximum, where the present results are slightly larger. Notice however, that ± 1σ are the 70% or so confidence limits; ± 2σ is 95%, and ± 3σ is 99%.

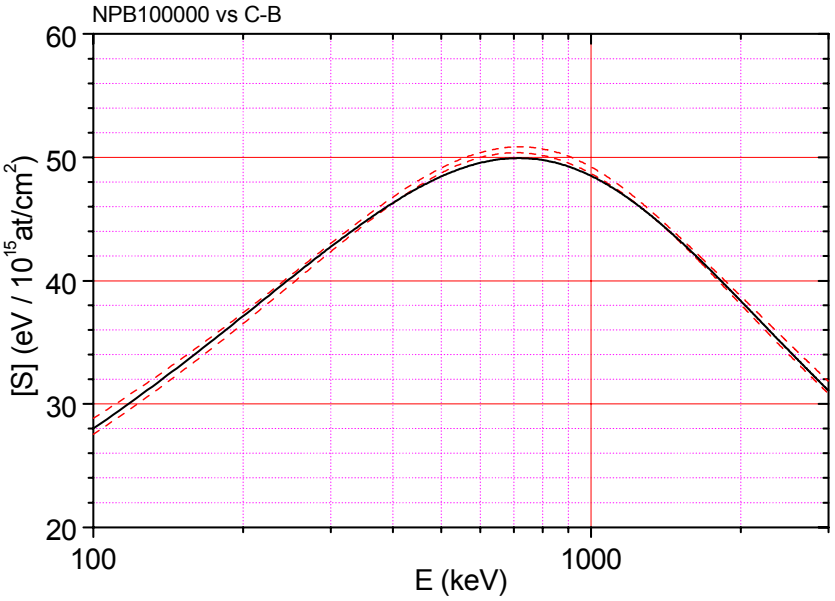

Figure 5. Calculated (dashed curves) and measured (solid curve) stopping powers for SiO_2.

4.3. Al_2O_3

A similar procedure as for SiO_2 was adopted. The results are given in figure 6. A different method, called symmetrical tilt energy shifts (STES), based on measuring spectra at ± θ, was used. The results are compared with the SRIM values.

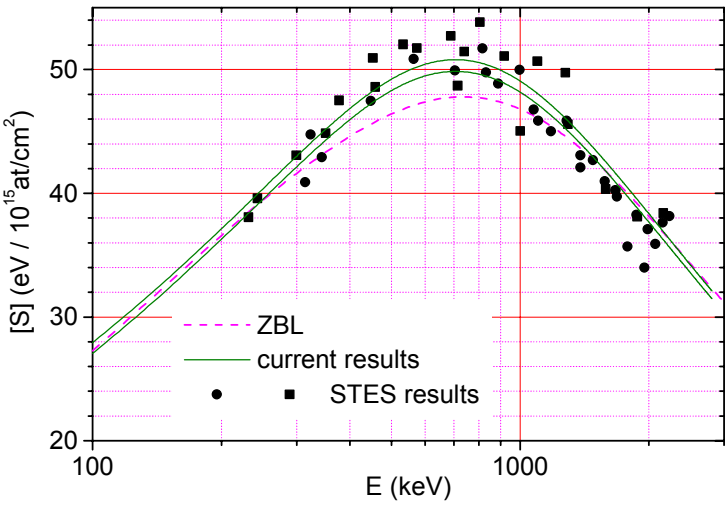

Figure 6. Comparison between calculated and measured stopping powers for Al_2O_3 .

5. CONCLUSIONS

We have devised an experimentally simple method to determine the stopping power of ions in matter. The method is universal and experimentally involves only measuring simple RBS energy spectra. The data analysis is involved, and requires using Bayesian inference with the Markov chain Monte Carlo algorithm. As the problems in measuring stopping powers have traditionally been associated with difficulties in the experimental methods, the alternative we present could become extremely useful.

The method employed uses Bayesian inference with the Markov chain Monte Carlo algorithm not only to determine the most likely stopping power curve in the whole energy range up to the highest beam energy used, but also to provide one with confidence limits on the results obtained, reflecting the uncertainty in the experimental parameters and in the data collection statistics. We applied the method presented to three cases, namely backscattering of ^4He off Si, SiO_2, and Al_2O_3, in the energy range up to 3 MeV.

REFERENCES

[1] ZIEGLER, J.F., BIERSACK, J.P., LITTMARK, U., Stopping and Ranges of Ions in Solids, (Pergamon, New York, 1985).

[2] LENNARD, W.N., MASSOUMI, G.R., SIMPSON, T.W., MITCHELL, I.V., Improved stoichiometry measurements using ^4He elastic backscattering: experiment and simulation, Nucl. Instr. Meth. B152 (1999) 370.

[3] KONAC, G., KALBITZER, S., KLATT, C., NIEMANN, D., STOLL, R., Energy loss and straggling of H and He ions of keV energies in Si and C, Nucl. Instr. Meth. B136-138 (1998) 159.

[4] ZIEGLER, J.F., RBS/ERD simulation problems: Stopping powers, nuclear reactions and detector resolution, Nucl. Instr. Meth. B136-138 (1998) 141.

[5] ZIEGLER, J.F., BIERSACK, J.P., SRIM2000 — The Stopping and Range of Ions in Matter, Version 0.06 (2000), code available from Ziegler@Watson.IBM.Com.

[6] REITER, G., KNIEST, N., PFAFF, E., CLAUSNITZER, G., Proton and helium stopping cross sections in H_2, He, N_2, O_2, Ne, Ar, Kr, Xe, CH_4 and CO_2, Nucl. Instr. Meth. B44 (1990) 399.

[7] NIEMANN, D., OBERSCHACHTSIEK, P., KALBITZER, S., ZEINDL, H.P., Energy loss and straggling of MeV ^{4}He ions in a Si/Sb multilayer target, Nucl. Instr. Meth. B80-81 (1993) 37.

[8] MUNNIK, F., PLOMPEN, A.J.M., RÄISÄNEN, J., WÄTJEN, U., Stopping powers of 200–3000 keV ^{4}He and 550–1750 keV ^{1}H ions in Vyns, Nucl.Instr.Meth. B119 (1996) 445.

[9] PLOMPEN, A.J.M., MUNNIK, F., RÄISÄNEN, J., WÄTJEN, U., Stopping powers of 200–3200 keV ^{4}He and 550–1550 keV ^{1}H ions in polyimide, J. Appl. Phys. 80 (1996) 3147.

[10] LINDHARD, J., SØRENSEN, A.H., Relativistic theory of stopping for heavy ions, Phys. Rev. A53 (1996) 2443.

[11] GRANDE, P.L., SCHIWIETZ, G., Impact-parameter dependence of the electronic energy loss of fast ions, Phys.Rev. A58 (1998) 3796.

[12] SCHIWIETZ, G., GRANDE, P.L., A unitary convolution approximation for the impact-parameter dependent electronic energy loss, Nucl. Instr. Meth. B153 (1999) 1.

[13] DOOLITLE, L., Algorithms for the rapid simulation of Rutherford backscattering spectra, Nucl. Instr. Meth. B9 (1985) 344.

[14] LEE, P.M., Bayesian Statistics, 2nd edition (Arnold, London, 1997).

[15] SMITH, C.R., GRANDY, W.T., (Eds.), Maximum Entropy and Bayesian Methods in Inverse Problems, Reidel Pub. Co. 1985.

[16] BARRADAS, N.P., JEYNES, C., WEBB, R.P., Simulated annealing analysis of Rutherford backscattering data, Appl. Phys. Lett. 71 (1997) 291.

[17] BARRADAS, N.P., JEYNES, C., JENKIN, M., MARRIOTT, P.K., Bayesian error analysis of Rutherford backscattering spectra, Thin Solid Films 343 (1999) 31.

[18] BARRADAS, N.P., KNIGHTS, A.P., JEYNES, C., MIRONOV, O.A., GRASBY, T.J., PARKER, E.H.C., High-depth-resolution Rutherford backscattering data and error analysis of SiGe systems using the simulated annealing and Markov chain Monte Carlo algorithms, Phys. Rev. B59 (1999) 5097.

[19] LULLI, G., ALBERTAZZI, E., BIANCONI, M., BENTINI, G.G., NIPOTI, R., LOTTI, R., Determination of He electronic energy loss in crystalline Si by Monte-Carlo simulation of Rutherford backscattering–channeling spectra, Nucl. Instr. Meth. B170 (2000) 1.

ION BEAM STUDIES OF ATOMIC TRANSPORT OF LIGHT ELEMENTS IN SILICON CARBIDE DURING VARIOUS TREATMENTS

G. Battistig
Research Institute for Technical Physics and Materials Science, Department of Ion Beam Analysis, Hungary

Abstract

The atomic transport of the important dopants aluminium and nitrogen in the technologically important material SiC was investigated using ion implantation and backscattering-channelling analysis. It was found that that the radiation damage induced by the ion implantation process is elevated in the case of SiC as compared to Si, even for low doses. Channeling implantation of SiC was used to minimize the amount of the implantation-induced defects. The difference of damage in C and Si sublattices was shown. The oxidation kinetics of SiC was also investigated using isotopic tracing of ^{18}O and nuclear reaction analysis. The results show different oxidation kinetics of SiC on Si- and C-terminated surfaces.

1. INTRODUCTION

Light elements, especially hydrogen, carbon and oxygen, have a major influence on the properties of thin films, as well as of bulk materials. It is essential to understand the transport mechanisms of these elements during various treatments, like annealing, ion implantation, etc. Because the typical thickness of a layer in recent applications decreases rapidly, there is a need to develop and apply experimental methods that sense these elements in the films with a very good sensitivity and depth resolution. Various ion beam techniques were applied during this work.

Due to silicon carbide's basic physical properties of high thermal conductivity, large bandgap, high carrier mobility, high breakdown voltage, etc, it is a promising material for optoelectronics, and as a substrate material for high frequency and high power active devices.

Due to the negligible diffusivity of the dopant atoms in SiC, only using ion implantation can perform the local doping of SiC. Al and N ion implantations were performed for doping SiC. RBS and channeling experiments show, that radiation damage is elevated in the case of SiC (compared to Si), even low dose implantations can amorphise the surface layer of the substrate.

It is also a big advantage that SiO_2 can be grown thermally on the surface of SiC. This material, being a polar crystal, one face of it is terminated by Si atoms only, and the other face is terminated by C atoms only. The oxidation kinetics differ seriously on these faces. Ion beam analysis presents a key method to follow how oxygen atoms move during annealing, and how an oxide layer grows.

The physical properties of SiC are given in Table 1.

Table 1. Physical properties of SiC

Bandgap energy: 4H 6H	 3.26 eV 3.03 eV
Breakdown voltage: 4H 6H	 2.2×10^6 V/cm 2.4×10^6 V/cm
Thermal conductivity: 4H 6H	 4.9 W/cmK 4.9 W/cmK
Saturated electron drift velocity: 4H 6H	 2×10^7 cm/s at 2×10^5 V/cm 2×10^7 cm/s at 2×10^5 V/cm
Structure	3C, 4H, 6H, 15R, 21R, more than 180 polytypes
Lattice parameter	a ≈ 11Å, c ≈ 3Å
Density	3.21 g/cm^3
Mohr hardness	9

2. CARBON IMPLANTED SILICON

2.1. Implantation

Carbon was implanted with a nominal dose of 800 μC/cm^2 ($5x10^{15}$/cm^2) into a 3-inch p-type <100> Si wafer with an energy of 38 keV. During implantation no sample heating or cooling was applied. The C ions were extracted from a CO_2 gas plasma, which is safer, but gives a lower yield comparing to CO. During implantation, the ion beam was scanned horizontally by an electrostatic plate and the wafers are moved mechanically in the vertical direction to ensure homogeneity. After implantation, the wafers were treated in an oxygen plasma to remove the hydrocarbon deposited onto the wafer surface during implantation.

SRIM simulations were done to calculate the depth distribution of implanted species and the created damage. We note that SRIM calculation is very good for ion distribution, but poor for damage. Two essential phenomena can be deducted from the simulations, namely, the carbon distribution has a skew Gaussian shape and the backside of it is not abrupt. In principle, a box shape profile can be achieved by multiple energy implantations. For the dose applied, the concentration of carbon in Si was estimated to be around 2%.

2.2. Carbon dose determination

The implanted dose was measured by ion beam analysis (non-Rutherford Backscattering) using the 5 MV Van de Graaff accelerator of the Institute. First, we applied the $^{12}C(p,p)^{12}C$ resonance at 1730 keV to measure the total amount of implanted carbon. The advantage of this measurement is the increased cross-section by a factor of about 70, and the high count-rate available at lower energy and lighter probe ion. However, in this case the depth resolution is rather poor. Measuring in channeling geometry, the background of C peak could be further decreased. The dose distributions across the wafer in horizontal and vertical directions were mapped by this method and found to be about ± 10%.

To get some information on depth distribution of implanted C a 3550 keV $^4He^+$ beam has been used. At this energy the increase in the cross-section of He for C comparing to the Rutherford one is only of about six times. However, the depth resolution is better than for the former case. Channeling was used to reduce the Si background. Even though, as seen in Fig. 1, the C peak is small comparing to the background. Thus, the accurate determination of C concentration in this case needs higher measuring dose of He. In the aligned spectrum, one can observe the damage peak induced by carbon implantation near the surface of Si. This damage peak becomes more visible in Fig. 2 where the aligned spectrum detected by the glancing detector — i.e. the backscattered ions are detected at angle of 97° with respect to the primary ion beam direction to ensure optimal depth resolution — is drawn. The peak of the depth distribution of the carbon ions induced damage locates around a depth of 110 nm, which is slightly deeper than that obtained from SRIM simulation.

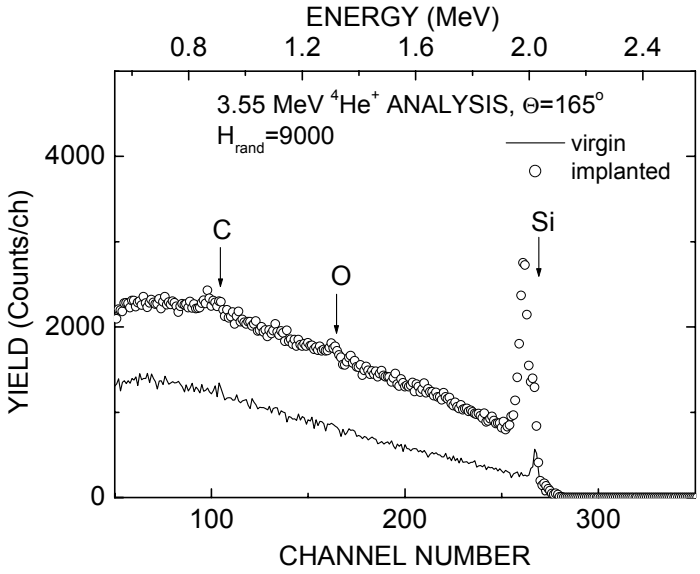

Figure 1. 3550 keV $^4He^+$ aligned backscattering spectra along <100> axis of the unimplanted (virgin) and the implanted samples. The detection angle was 165°.

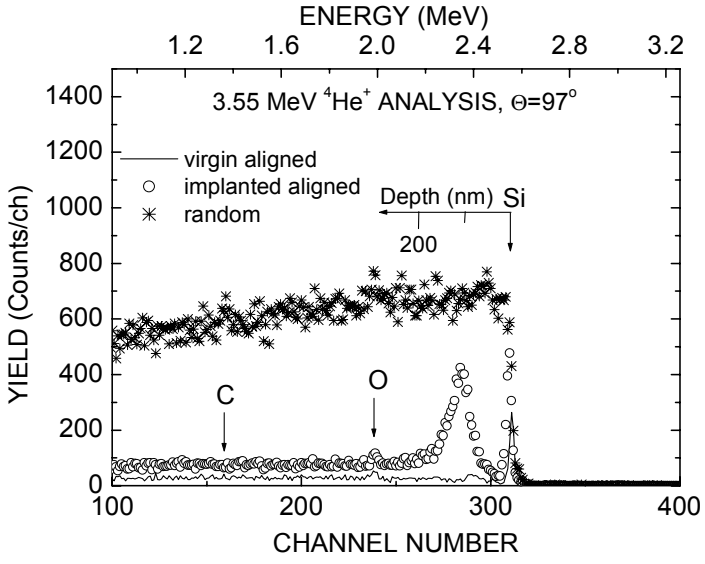

Figure 2. 3550 keV $^4He^+$ backscattering spectra aligned along <100> axis of the unimplanted (virgin) and the implanted samples. The detection angle was 97°.

3. DETERMINATION OF He CROSS SECTION FOR CARBON AND SILICON AROUND 4.2 MeV

An other possibility to study carbon with great sensitivity is the 4.26 MeV resonance in the cross section of the $^{12}C(\alpha,\alpha)^{12}C$ nuclear reaction. The cross section of this reaction at 165º scattering angle is rather well known, but our previous experiments showed differences to the values published before. The cross section of He for Si in this energy range varies very quickly with the energy. Although these cross sections are known since long, the accuracy of the data available is not sufficient for the determination of carbon defects in ion implanted silicon and silicon carbide (SiC) samples. To apply this nuclear reaction technique, hence, requires verifying the cross sections available from the literature.

For this reason proper multilayer samples were produced for cross section measurements. Carbon is a light element, therefore, in backscattering experiments, if a thin carbon layer is deposited on the surface of a heavier substrate, the yield from carbon is situated in a high background due to heavy substrate. To avoid the background of a heavier substrate, the application of a substrate lighter than carbon could be a solution. However in our case there is no easy way to apply such a substrate. To overcome this problem, multilayer samples were produced: a vitreous carbon substrate was applied, a 8.4×10^{17} Au/cm^2 thick gold layer was deposited by evaporation on it, on the top of the gold, a very thin SiC layer was grown by microwave plasma deposition. In Fig. 3 two backscattering spectra are shown taken at 4240 keV and 4280 keV He energy. These two graphs illustrate how the yield from the carbon substrate and the yield from the carbon in the surface layer are separated on the SiC/Au/C multilayer sample.

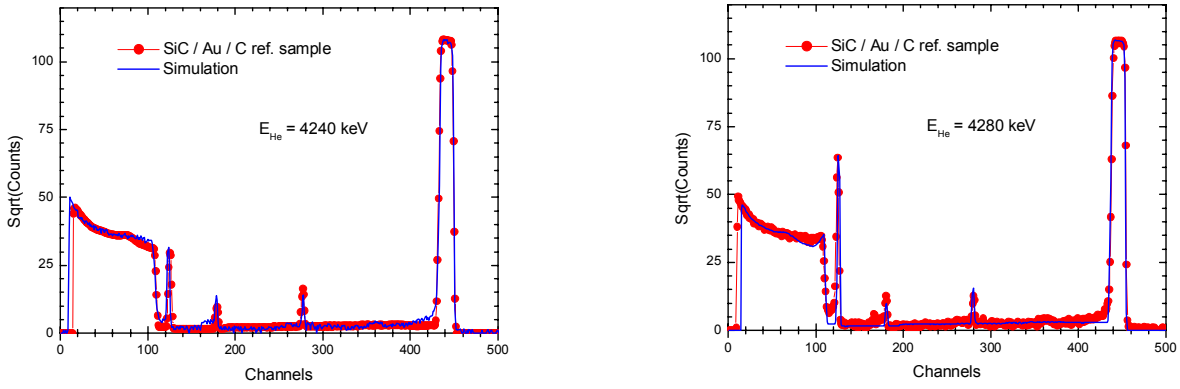

Figure 3. $^4He^+$ Backscattering spectra of the multilayer sample recorded at two different energies. Surface carbon and silicon appears at channel ≈120 and channel ≈280 respectively. The peak corresponding to the gold layer is located at the far end, at around channel ≈450. The peak appearing at channel ≈180 corresponds to oxygen that is always present at the surface. It can be seen, that the yield from the carbon substrate (beginning at channel ≈105) is well separated from the yield due to the carbon in the surface layer.

Scanning over a larger energy range and recording the backscattering spectrum at every energy step, the peak areas corresponding to carbon and silicon can be determined. Hence from the C and Si peak areas the cross section curves can be created (see Fig. 4). We found that the resonance peak in the C cross section at 4.26 MeV is smaller by about 12.5% than the value given [1]. Also, the cross section of Si [2] should be shifted by 13 keV towards the larger energies.

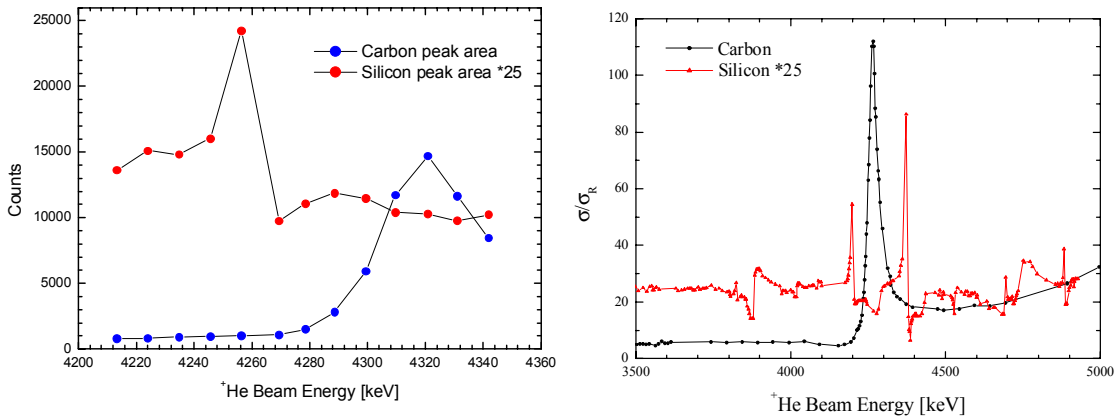

Figure 4. Left side: Carbon and silicon experimental peak areas in the energy range of 4210 keV to 4350 keV, right side: the updated He cross sections for carbon and silicon.

4. A IMPLANTED 4H-SiC

4.1. Implantation

Single crystalline 4H-SiC samples (from CREE Res. Inc.) were implanted with 200 keV and 350 keV Al^+ ions at room temperature. The implant dose was about $4\times10^{13}/cm^2$ for both energies. During implantation the ion beam was swept electrostatically both in x and y directions.

4.2. Results

In Fig. 5, backscattering-channeling spectra of a SiC sample implanted with 200 keV $4\times10^{13}/cm^2$ Al^+ are shown. A scattering angle of 165° was chosen at the beam energy of 3550 keV.

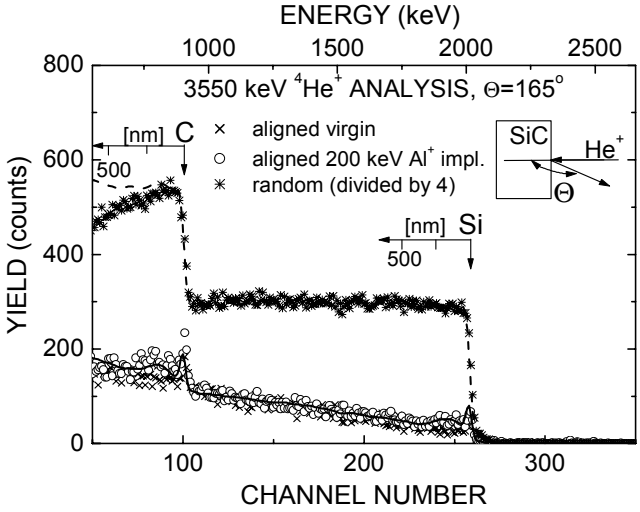

Figure 5. Backscattering spectra of 4H-SiC sample implanted with 200 keV 4×10^{13} Al^+/cm^2. Aligned backscatering spectra were measured along the <0001> axis. Depth scales for comparison are shown. The simulated spectra are also shown for implanted aligned 4H-SiC (solid line) and for the random case (dashed line).

In contrary to the conventional backscattering measurement, where the small radiation defects are hardly visible in the carbon sublattice, here the damage is well visible in both sublattices. Fig. 5 also shows the simulated spectra for implanted aligned 4H-SiC and for the random

case. In the simulation of the aligned spectrum only the assumption of different Gaussian distributions of disorder for different (Si or C) sublattices give acceptable fit. The simulated damage level for C differs from that of Si by a factor of 1.3 with a maximum damage level of 2 % located at a depth of 160 nm beneath the surface.

The damage in the sample implanted with 350 keV 4×10^{13}/cm^2 Al^+ (not shown here) is still visible in both sublattices. However, the damage peak is flatter and has a larger width compared to the case for 200 keV implantation, which makes the evaluation of the aligned spectrum rather difficult. It is noted that the depth resolution for silicon at the surface is about 34 nm.

Using the 4260 keV resonance for $^{12}C(\alpha,\alpha)^{12}C$, we can enhance the sensitivity of the backscattering measurement further, but the depth resolution for silicon at the surface is poorer compared to the previous cases. Fig. 6 presents spectra recorded using an analysing beam energy of 4300 keV, which is above the resonance energy. Aligned spectra taken on virgin and implanted samples are shown.

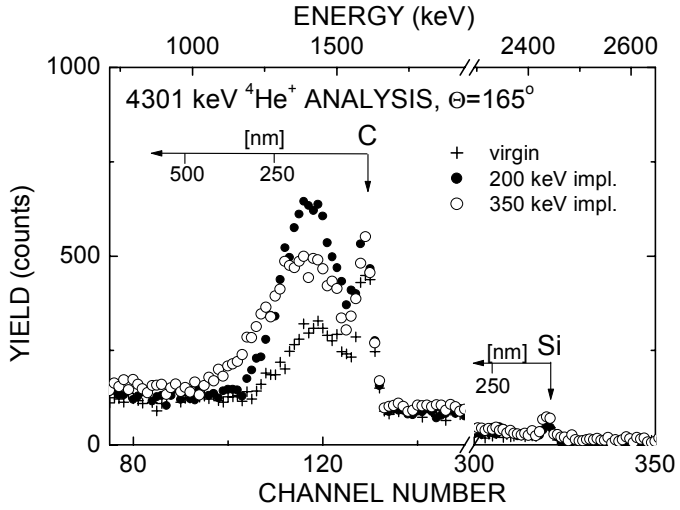

Figure 6. Aligned backscattering spectra of 4H-SiC samples implanted with 4×10^{13} Al^+/cm^2 of 200 keV and 350 keV energies. For comparison a virgin spectrum is also shown. Aligned backscattering spectra were measured along the <0001> axis.

The area of the resonance peak corresponds to the number of carbon atoms displaced from their lattice sites. Varying the incident beam energy (i.e, determining the excitation curve) (see Fig. 7) the depth distribution of displaced carbon atoms, i.e., damage, can be obtained. In Fig. 8, excitation curves recorded on the same samples are shown.

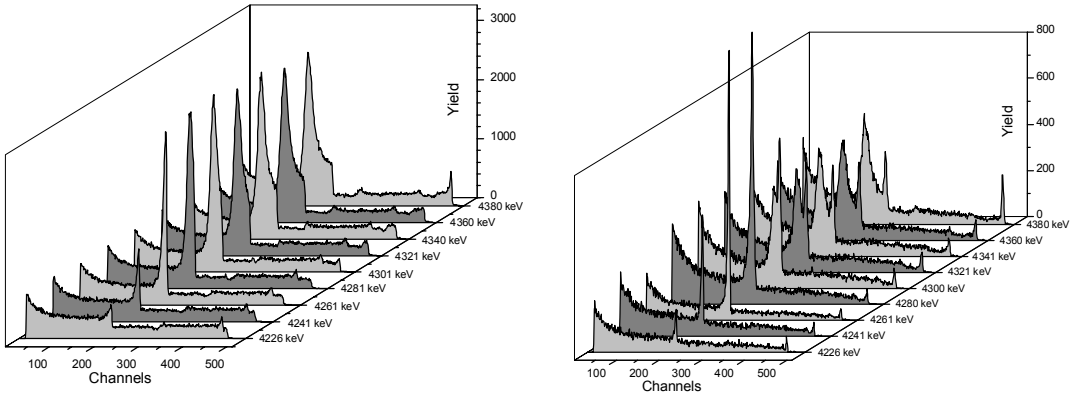

Figure 7. Random (left) and aligned (right) backscattering spectra, taken at 165° detection angle and at increasing beam energies. It is easily seen how the resonance peak moves toward deeper region in the sample.

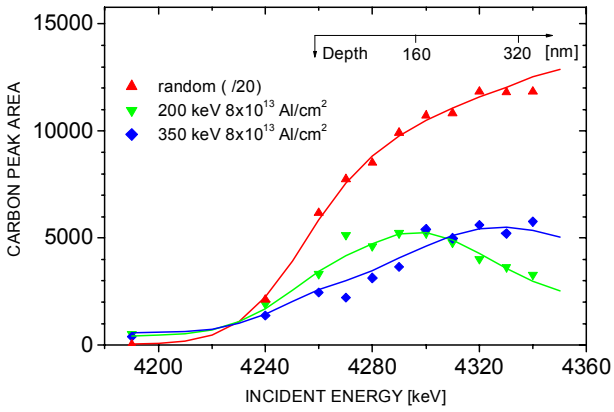

Figure 8. Excitation curves recorded on aligned SiC samples implanted with Al at different energies. The carbon peak areas were determined from similar spectra as shown in Fig. 4. Each point was measured with 8 μC/points in a fresh spot on the sample to avoid beam effects. To eliminate the background, the corresponding aligned virgin spectra were subtracted. For comparison the excitation curve for random case is also shown. (Solid lines are smoothing fits, used only for guiding the eyes.)

The excitation curves roughly follow the damage distributions created by the ion implantation. The excitation curve of 200 keV implanted sample exhibits a maximum around 4300 keV that corresponds to the maximum damage at around 160 nm. The decreasing edge at higher energies shows the decreasing damage at the deeper regions. In the case of 350 keV implantation only the region of increasing damage was exploited due to the fact that the practical maximum energy of the accelerator now was only 4340 keV. The evaluation of the excitation curves revealed the difference between Si and C sublattice damage level to be of a factor of 1.3, similar to the result from 3550 keV He measurements.

5. N IMPLANTED SiC

5.1. Implantation

Ion implantation appears to be suitable for selective doping of silicon carbide (SiC), which is the potential candidate for application in high-power and high-frequency devices capable of

operating at elevated temperature. However, this technique introduces defects into single crystalline SiC. When the implantation damage exceeds a critical threshold recrystallization of the implanted layer hardly takes place during post-annealing, and also, poor electrical characteristics could be observed. Therefore, keeping defects under a desired level during implantation is one of the most important goals in SiC device fabrication. It has been shown that channeling implantation appears to be one of the ways to reduce the implantation damage. However, no direct experimental observation of the damage distribution has been shown until now.

As N is a widely used donor in SiC, N implantation is a plausible n-type doping technique for fabrication of transistors. Moreover, a real angular scan can be measured with N ions, which presents the angular half-width ($\Psi_{1/2}$) of the <0001> channel in 6H-SiC. Since $\Psi_{1/2}$ is one of the most important parameters characterizing the channeling process, the measured angular scan curve could help to understand some aspects of channeling implantation.

Studying crystal defects created by ion bombardment Backscattering Spectrometry combined with channeling technique is a method extensively used. In our present work we used 3550 keV $^4He^+$ which was already successfully applied in our previous investigations to study separately the Si and C sublattices of SiC.

Double-side polished <0001> on-axis single crystalline 6H-SiC samples from CREE Res. Inc. were used. Channeling experiments were carried out using a two-axis goniometer with a tilt and angular precision of 0.01°. A 0.5 MeV N^+ angular scan was performed through the <0001> axis of 6H-SiC. The scan was conducted 15° off from the [11–20] plane. A fluence of about 2.6×10^{14} N^+/cm^2 was used for each angle. Change to fresh spot of the sample was done after every 8 measurements.

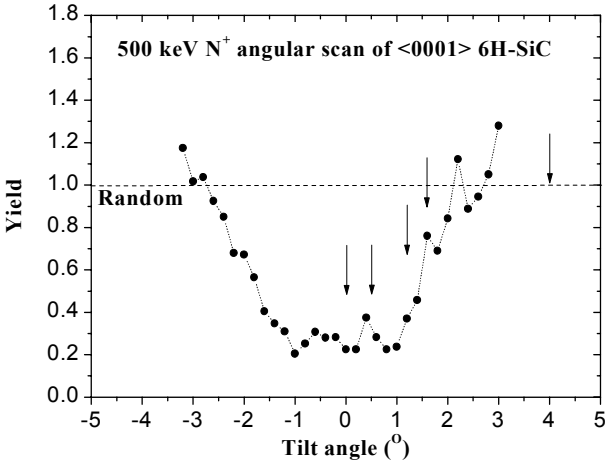

Figure 9. 500 keV N^+ angular scan through <0001>-axis of 6H-SiC. The selected implantation tilt angles are marked by the arrows.

After N^+ implantation, 3550 keV $^4He^+$ channeling measurements were carried out using a low current of 15 nA to reduce the damage created by the analysing beam itself. Damage depth distributions were evaluated from BS/C spectra using the RBX code. In the evaluation of the damage, average potential was assumed for dechanneling calculation, since Si and C atoms locate one after the other in the <0001> atomic row of 6H-SiC, or randomly as an interstitial.

The 500 keV N^+ angular scan around the <0001> axis of 6H-SiC is shown in Fig. 9. Due to low energy of backscattered N ions (≤ 63.5 keV), the total yield was used for each point, which holds information just about the surface layer of the sample (~100 nm). Based on the angular scan, implantation tilt angles of 0^o, 0.5^o, 1.2^o, 1.6^o and 4^o have been chosen.

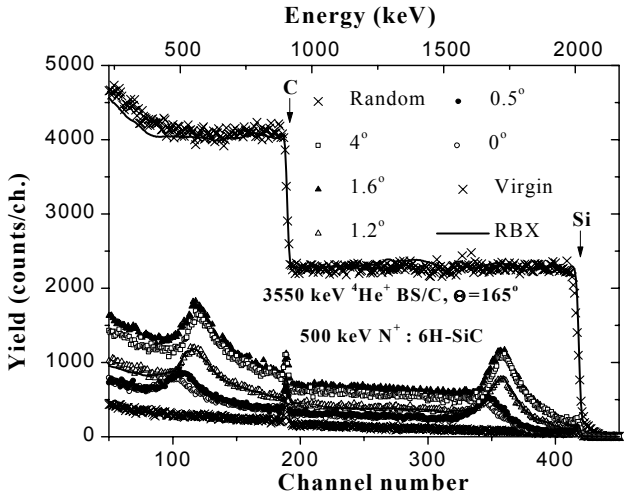

Figure 10. Aligned 3550 keV backscattering spectra of 6H-SiC implanted by 500 keV N^+ with a fluence of $1.5\times10^{15}/cm^2$ at room temperature from different directions. For comparison, virgin and random spectra are also shown. Solid lines represent RBX simulations of random, virgin, and the 1.2^o implanted spectra.

Fig. 10 shows the <0001>-aligned backscattering spectra of SiC implanted at different tilt angles. For comparison, random and aligned virgin spectra are also included, as well as the RBX simulations for random, virgin and 1.2^o implanted spectra. On the channeled spectra of the implanted SiC both of Si and C sublattice damage are readily resolved owing to the high non-Rutherford cross-section of helium for carbon at an ion energy above 3 MeV. The extracted damage distributions are shown in Fig. 11(a) and (b) for the Si and C sublattices, respectively. The essential difference between channeling and random implantation is that the defect peaks of both Si and C are shifted about 25% deeper — from about 570 nm to about 720 nm — for on-axis irradiation. When increasing the tilt from 0^o, the damage peak moves toward the surface. We then could observe that random implantation conditions are reached at a tilt angle of 1.6^o.

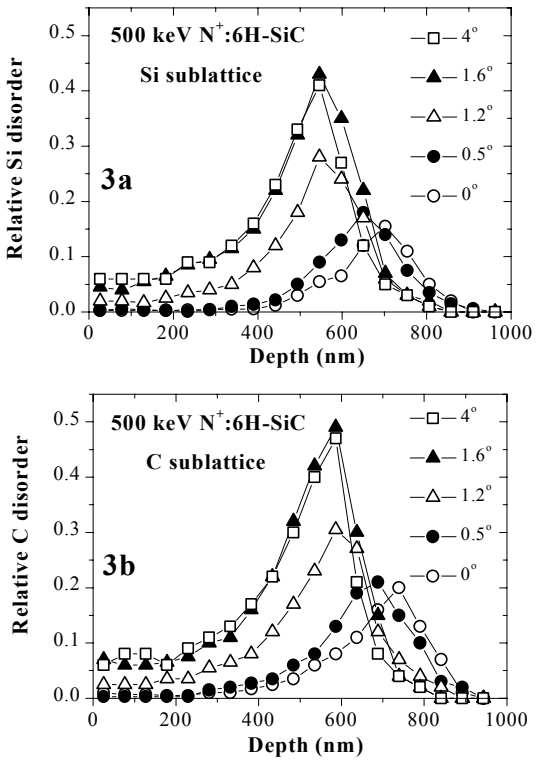

Figure 11. Relative disorder in the a) Si and b) C sublattices of 500 keV N^+ implanted 6H-SiC in function of depth extracted from channeling spectra using RBX code.

The most remarkable observation in Fig. 11 is that in both sublattices, about 3 times less damage was created by on-axis implantation than by the random one.

As one can see in Fig. 11, the shapes of the damage curves at each tilt angle are similar for Si and C sublattices, but more defects are induced for C than for Si. This result reveals that the effective displacement energy is higher for Si than for C in the present circumstances. The estimation of the effective displacement energy for Si and C sublattices by SRIM2000 code is 23.5 eV and 17 eV, respectively.

The presented work shows the advantages of channeling implantation of SiC to minimize the amount of the implantation induced defects. The difference of damage in C and Si sublattices was demonstrated.

6. AL IMPLANTED SiC — EFFECT OF ION BEAM FLUENCE

The combination of Backscattering Spectrometry and channeling with the $^{12}C(\alpha,\alpha)^{12}C$ nuclear resonance at 4.26 MeV to study radiation damage in the carbon sublattice of 6H-SiC was applied. 6H SiC samples were implanted with 200 keV Al ions in a dose range of $4\times10^{14}/cm^2$ - $1\times10^{16}/cm^2$ with different current densities at room temperatures. The implanted samples were annealed at 1200ºC in argon for 1 hour. In the case of low dose, low current density implantation damage recovery seems to be complete.

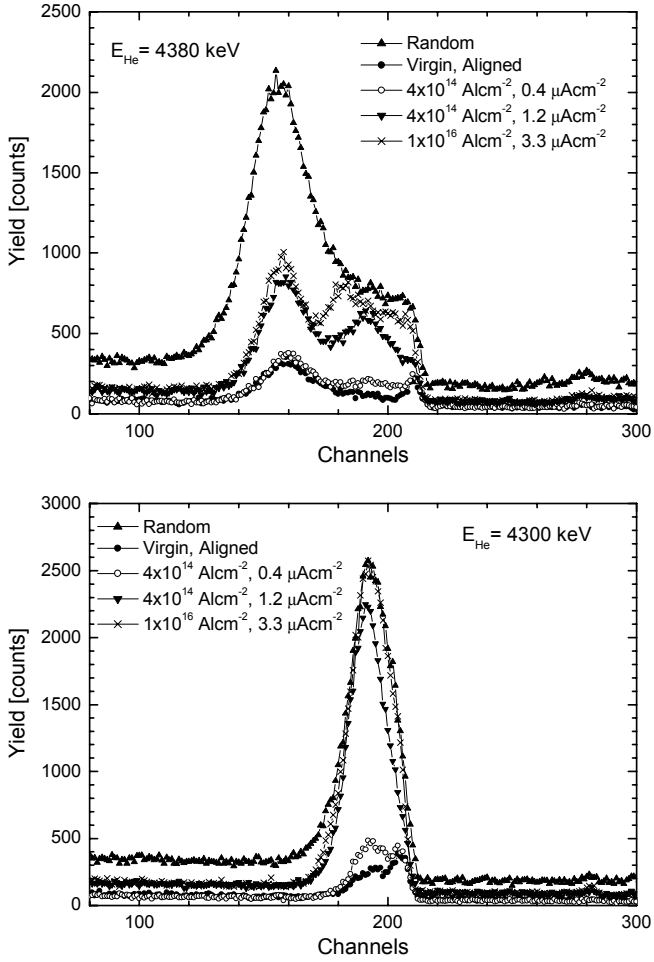

Figure 12. Spectra recorded on SiC samples at 4.3 MeV (bottom) and 4.38 MeV (top) bombarding energy. The dose and current densities of implantation are indicated on the figure.

In Fig. 12 the channeling spectra of ion implanted SiC are shown recorded at 4300 keV and 4380 keV, respectively. The random and virgin spectra are also shown. Comparing the implanted, virgin and random carbon peak areas, the damage created by ion implantation in the carbon sublattice can be determined.

Varying the incident beam energy step by step above the resonance energy and determining the peak area vs. energy curve, the depth distribution of displaced carbon atoms, i.e., damage, can be obtained. Such curves recorded on implanted samples are shown in Fig. 13. The carbon peak areas were determined from similar spectra as shown in Fig. 12. In this case the measuring dose was 10 μC, each measurement was performed of a fresh impact point on the sample to avoid the beam effects. To eliminate the background, the corresponding aligned virgin spectra were subtracted.

From Fig. 12 we can deduct that for the 200 keV Al implantation the maximum damage appears at about 150 nm below the surface. Low dose and low current density implantation (4×10^{14}/cm^2, 0.4 μA/cm^2) generates small damage, while the same dose, but higher current density implantation results in higher lattice disorder. High dose implantation (1×10^{16}/cm^2, 3.3 μA/cm^2) generate an almost amorphised, highly damaged layer. It is also seen, that the damage distribution follows the depth distribution of the implanted ions. It is smaller close to the surface and highest near to the projected range of the ions. In the case of the sample

implanted with a dose of $2\times10^{15}/cm^2$ with a current density of 0.4 $\mu A/cm^2$ amorphisation seems to be complete near to the surface, but deeper the damage becomes smaller compared to the highest dose implantation.

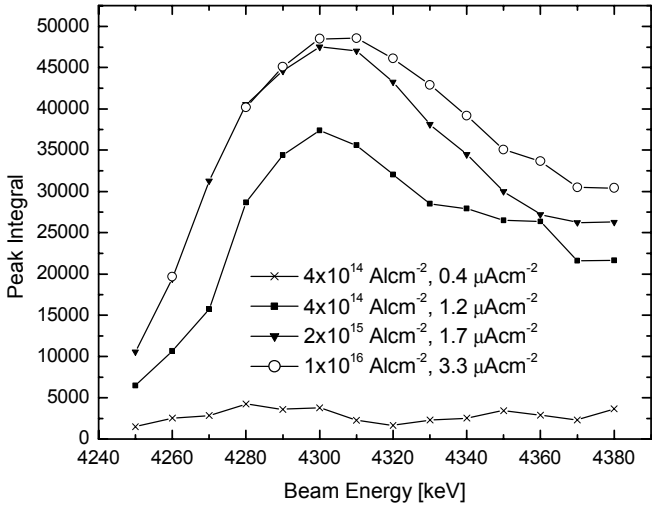

Figure 13. The carbon peak integrals are presented as a function of the bombarding energy.

The effect of the post implantation annealing was also followed by this method. The implanted samples were annealed at 1200ºC in an argon atmosphere for 1 hour. During annealing a thin oxide layer formed on the surface of the samples due to the small amount of H_2O existing in the ambient atmosphere. In the case of low doses, low current density implantation damage recovery seems to be complete. For higher dose implantation partial crystal recovery only occurs near to the bulk in the damaged layer, while the number of displaced carbon atoms hardly decreased near to the surface.

7. OXIDATION OF SiC

Since numerous institutes and laboratories deal with SiC, the oxidation properties of this crystalline material are widely studied. However results from various groups are hardly comparable because the substrate material used often has different polytype (crystalline SiC presents more than 180 different polytypes), the experimental parameters are imperfect (it is rarely given which face of SiC is considered). Systematic oxidation studies, hence, are needed on both sides of a well-chosen polytype of SiC.

First experiments on oxidation of 6H-SiC were performed in co-operation with Groupe de Physique des Solides, Université Paris. Nuclear reaction analysis was used to measure the number of oxygen atoms incorporated into the SiO_2 later. The results obtained show the different oxidation kinetics on a Si and C-terminated surface.

Both faces of 6H SiC were oxidised in a dedicated UHV furnace which allows us to perform ultra-dry ($[H_2O] < 1$ppm) oxidation using $^{18}O_2$ gas up to 1100ºC. The samples were studied by the $^{18}O(p,\alpha)^{15}N$ nuclear reaction around 730 keV, allowing us to determine the total amount of oxygen present in the samples. It turned out (Fig. 14) that the growth rates are sub-linear for both faces of 6H SiC. This cannot be caused by a simple interfacial limitation of the reaction rates.

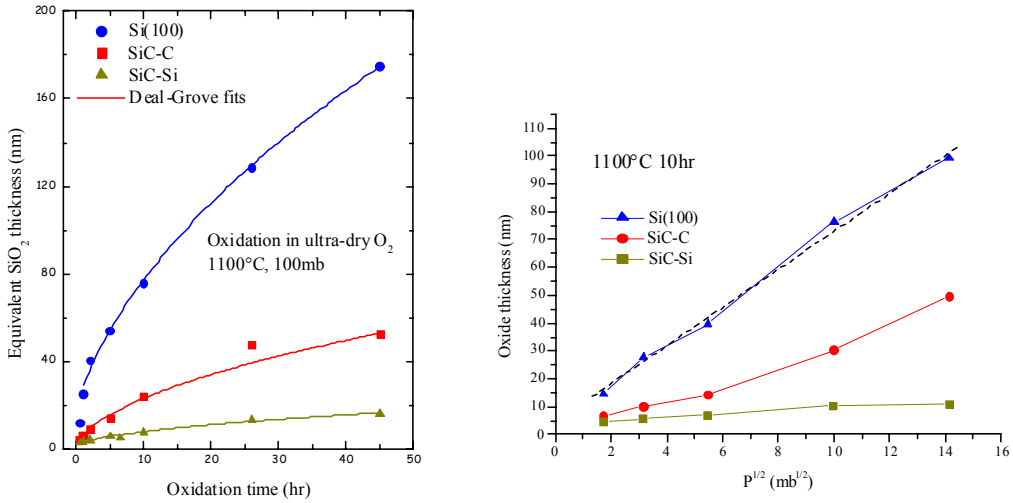

Figure 14. The measured oxide thickness vs oxidation time for Si (100), SiC Si and C terminated surfaces (left). The pressure dependence of the formed oxide thickness (right).

Pressure dependence in the parabolic regime was also determined. Oxide thickness is proportional to ~p for 6H SiC-C and ~$p^{1/4}$ for 6H SiC-Si, suggesting the establishment of different chemical equlibria in the interfacial region.

In Fig. 15 excitation curves are presented. They were recorded on SiC samples oxidised at first in $^{16}O_2$ gas at 100 mbar, and 1100ºC for 40 hours, and subsequently in $^{18}O_2$ gas with the same parameters, but for 5 hours. The oxidation takes place at the SiO_2/SiC interface (similarly to Si). The peak around 156 keV for SiC-Si and around 168 keV for SiC-C is related to the ^{18}O fixed at the interface. A peak at the sample surface is due to a physical exchange of ^{16}O and ^{18}O at the surface. The concentration profiles show that the ^{18}O / Si ratio in the interface region is far from 2; there is a mixture of ^{16}O and ^{18}O is present in this region.

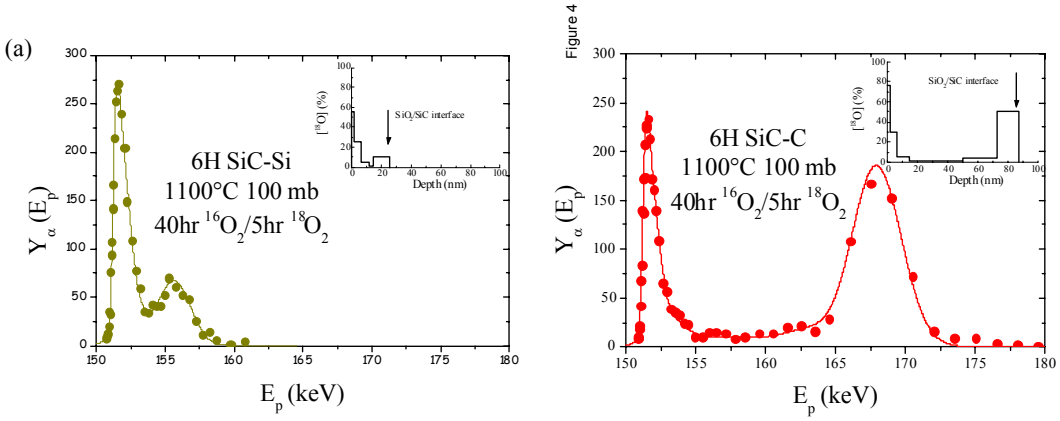

Figure 15. $^{18}O(p,\alpha)^{15}N$ nuclear reaction resonance excitation curves recorded around the 152 keV resonance. In the inset the calculated ^{18}O concentration profiles are given.

Oxidation in pure $^{18}O_2$ followed by resonance profiling [$^{18}O(p,\alpha)^{15}N$ nuclear reaction resonance at 152 keV] shows that the oxide is stoichiometric in the region where the oxygen marking is less than 100% in the isotopic tracing experiments. The solid lines in Fig. 16 (left)

are calculated best fit excitation profiles for the abrupt-interface structure shown in Fig. 16 (right) with 16nm (SiC-Si) on top of 79 nm of pure SiO_2. The dashed lines in Fig. 16 (left) are calculated excitation curves for depth distributions containing the same total amount of ^{18}O, distributed as shown by the dashed lines in Fig. 16 (right).

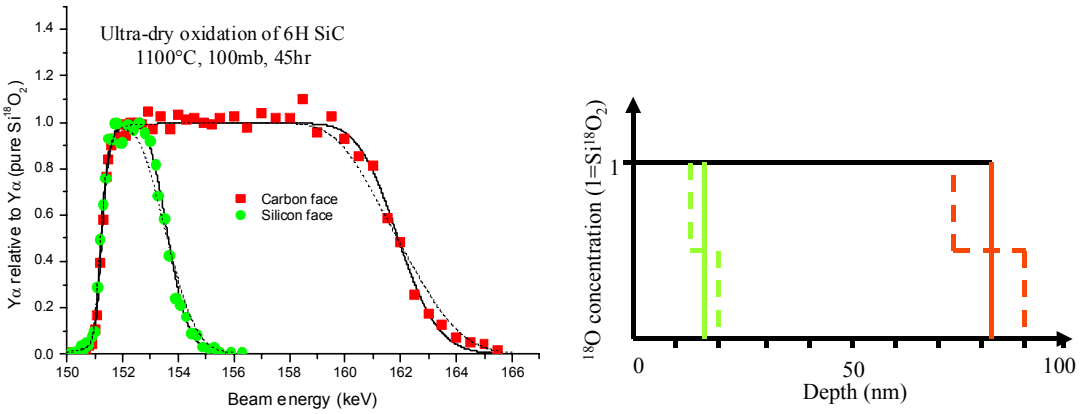

Figure 16. $^{18}O(p,\alpha)^{15}N$ nuclear reaction resonance excitation curves for samples treated in pure $^{18}O_2$ (left). The calculated concentration profiles are also presented (right).

Thermodynamically, the oxidation of SiC-Si and SiC-C are the same — the chemical energy released per unit of SiO_2 formed is the same (and positive). The reaction is thus kinetically limited. The central question is, how does the polarity of the crystal influence the oxidation mechanisms and rates? If the limitation is simply the interface reaction rate, then we would expect linear oxide growth kinetics, contrary to our observations. In the parabolic regime studied here, the limitation cannot be due to diffusion of oxygen through the growing oxide, as was the case for silicon, since then we would expect similar growth rates to those observed on Si(100), which is not the case here. If the limitation is simply due to diffusion of reaction products (assumed the same for each face) out through the oxide, then we would expect the same growth rate on SiC-Si and on SiC-C, at least in the parabolic regime, which is not the case here either.

However, the data presented here give us some clues. The very different pressure dependencies of the oxidation rate on the two faces and on Si(100) suggests the establishment of different equilibria between chemical reactions occurring near the interface. We can imagine three hypotheses to explain the weak isotopic marking of the interfacial growth region:

1. Exchange due to oxygen lattice movement.
2. Lower total oxygen concentration due to substoichiometric oxide or the presence of high impurity concentrations (e.g. carbon).
3. Silicon atomic movement.

We have previously shown that after a further oxidation in $^{16}O_2$, the oxygen fixed in the region of the interface does not move appreciably, thus excluding hypothesis 1. The measured total oxygen concentration as a function of depth shown in Fig. 16 allows us to exclude hypothesis 2. Thus hypothesis 3 appears to be the most reasonable at present. We note that the atomic density of silicon atoms in SiC is almost the same as that of silicon atoms in Si, and that the atomic density of silicon in SiO_2 is approximately half of that in Si — so one volume

of Si or SiC produces two volumes of SiO_2 upon thermal oxidation. In the case of oxidation of silicon, the resulting stress is responsible for the injection of interstitial silicon atoms into the silicon substrate. In the case of thermal oxidation of SiC, we expect to have the same Si interstitial generation as in the case of thermal oxidation of Si, but a reduced elimination of the interstitials from the vicinity of the SiO_2/SiC interface because of the much lower Si diffusion coefficient in the dense SiC lattice. This could promote injection of Si atoms into the SiO_2 matrix during oxide growth. It is clear that a Si isotopic tracing experiment would shed light on this system — one such experiment would be deposition of a thin $^{29}SiO_2$ layer onto SiC, and subsequent oxidation. Is the ^{29}Si in the oxide, after growth of further oxide, diluted by the arrival of the supposed Si atoms which are oxidised at some distance from the interface?

8. CONCLUSIONS

It was found that that the radiation damage induced by the ion implantation process is elevated in the case of SiC as compared to Si, even for low doses. It has been shown that there are differences of damage in C and Si sublattices. Channeling implantation of SiC was found to be an effective method to minimize the amount of the implantation-induced defects.

We found that the resonance peak in the C(α,α)C cross-section at 4.26 MeV is smaller by about 12.5% than the value given [1]. Also the cross-section of Si(α,α)Si [2] should be shifted by 13 keV towards a higher energy.

The oxidation kinetics of SiC was investigated using isotopic tracing of ^{18}O and nuclear reaction analysis. The results show different oxidation kinetics of SiC on Si- and C-terminated surfaces. The oxidation mechanism of Si is well understood; the Deal-Grove model describes the kinetics of oxidation. In our work isotopic tracing combined with $^{18}O(p,\alpha)^{15}N$ nuclear reaction resonance was the key method to determine the transport properties of the corresponding atoms during oxidation of SiC. Our results give a deep insight into the oxidation mechanism and kinetics, but we do not fully understand the oxidation mechanism, hence further investigations are still needed to clarify the atomistic processes involved.

REFERENCES

[1] FENG, Y., ZHOU, Z., ZHOU, Y., ZHAO, G., Cross sections for 165° backscattering of 2.0–9.0 MeV 4He from carbon, Nucl. Instr. Meth. B86 (1994) 225.

[2] LEUNG, M.K., Ph.D. dissertation, University of Kentucky, USA (1972).

DETERMINATION OF RANDOM AND CHANNELING STOPPING POWERS OF LIGHT ATOMIC AND MOLECULAR IONS IN Si AND SiO_2 SUBSTRATES

M. Behar
Universidade Federal do Rio Grande do Sul, Instituto de Fisica, Laboratory de Implantacao Ionica, Brazil

Abstract

The random stopping powers of He, Be and O in Si have been measured in the energy range between 200 keV and 13.5 MeV. The results agree well with other published measurements and have been parameterized according to the formula proposed by Kalbitzer and collaborators. The channeling stopping powers of Li, Be and O in Si have also been measured in the energy range from 200 keV to 13.5 MeV. This data has been used to understand polarization effects during the interaction ion-matter. The molecular stopping power of H_3 as well as the straggling of H has been measured for thin SiO_2 films. The results have provided new information on the effects of the inhomogeneous distribution of electrons in calculations of straggling in this structure.

1. THE MOLECULAR STOPPING POWER OF H_3 IN SiO_2 TARGETS

In order to perform this experiment we have used $Si^{18}O_2$ films with thickness that ranged between 2.5 and 50 nm. Beams of H and molecular H_3 were employed together with the $^{18}O(p,\alpha)^{15}N$ nuclear reaction in order to determine, for each case, the thickness of the corresponding film. Consequently the ratio of the thickness determined with H_3 and H gives directly the ratio between the molecular and atomic stopping powers. The results of these experiments show that this ratio is about 1.8 for the thinnest target and decreases with increasing thickness as shown in Figure 1. At 50 nm it reaches the unity. The results agree well with the Lindhard model for different Wigner-Seitz radius [1].

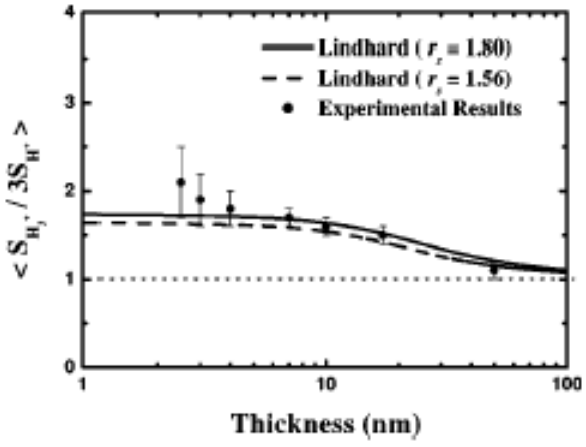

Fig. 1 Ratio of the thickness of $Si^{18}O_2$ films measured using molecular H_3 and atomic H. For films < 10 nm, this ratio is ~ 1.8. The solid and dashed lines are theoretical predictions.

2. RANGE PARAMETERS OF ^{18}O IMPLANTED IN Si AND SiO_2

We have determined the range parameters of O in Si and SiO_2 by implanting ^{18}O in both matrixes in an energy range between 25 and 200 keV. We have used the $^{18}O(p,\alpha)^{15}N$ nuclear resonant reaction at 151.2 keV in order to determine the ion distribution as a function of the depth. The results were compared with the TRIM predictions as listed in Table 1, and plotted in Fig. 2. In general, we have obtained a good agreement with respect to the projected ranges. Conversely, the agreement between experiment and TRIM predictions for the projected range straggling is worse, as is shown in Fig. 2 for oxygen in amorphous silicon. Currently, we do not have a plausible explanation for this behavior. These results have been published [2].

Table 1. Summary of the experimental range parameters, and the corresponding calculated TRIM values

	Target (Si)				Target (SiO_2)			
	Experimental		TRIM		Experimental		TRIM	
Energy (keV)	R_p (Å)	ΔR_p (Å)	R_p (Å)	ΔR_p (Å)	R_p (Å)	ΔR_p (Å)	R_p (Å)	ΔR_p (Å)
25	554	181	601	233	480	237	597	228
50	992	334	1158	385	877	316	1185	393
75	1545	357	1697	516	1350	371	1771	423
100	1957	587	2241	640	1880	404	2354	630
150	2918	661	3305	805	2703	655	3458	804
200	3982	569	4303	941	3419	544	4526	946

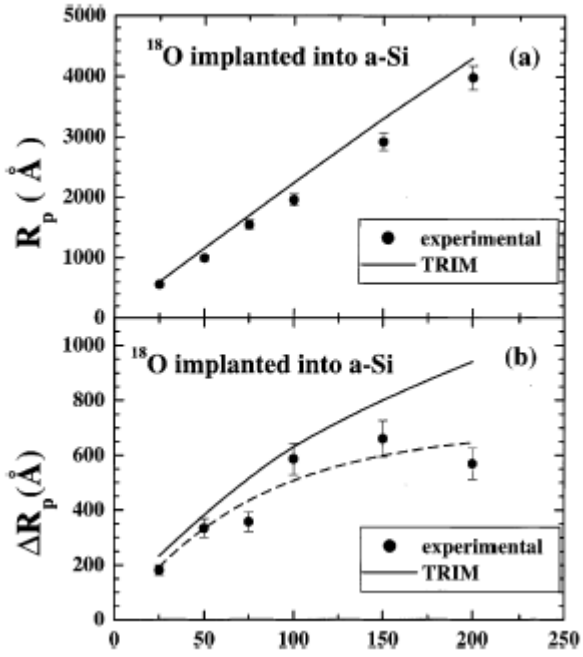

Figure 2. Experimental and TRIM range parameters of ^{18}O implanted in Si.

3. DETERMINATION OF He AND Li CHANNELING STOPPING POWERS IN Si

We have measured the He and Li stopping powers along the Si<100> and Si <110> directions in a energy range that covers typically the 400 keV — 5 MeV region. With this aim we have used the RBS/Channeling technique together with a SIMOX target (20 nm of Si<100> on top of a SiO_2 400 nm layer on top of a Si bulk). By measuring, for each energy, the corresponding random and channeling spectra and following a standard procedure develop in our laboratory [3], it is possible to determine the channeling stopping power for each case. The results were compared with first order calculations using the Unitary Convolution Approximation (UCA). Good agreement is observed at higher energies, while at lower energies the UCA predictions underestimated the experimental values in Fig. 3. This feature reflects the polarization of the medium (Barkas effect [4]) as was demonstrated in [5]. These results, along with random energy loss measurements of both ions in Si, have been published [6].

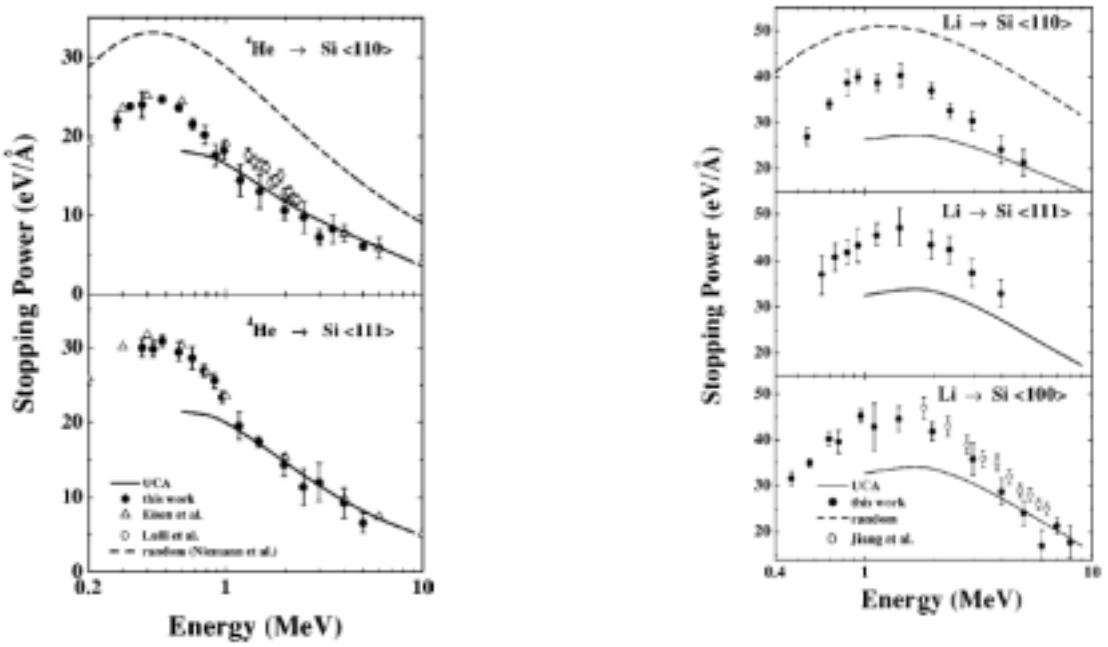

Fig. 3. Measured channeling stopping powers of ^{4}He in Si (left) and Li in Si (right). The solid and dashed curves are theoretical calculations using the UCA method.

4. DETERMINATION OF RANDOM AND CHANNELING STOPPING POWERS OF O AND Be IN Si TARGETS

We have measured the random and channeling stopping powers of O and Be into Si. For the random stopping, we have used a Bi marker implanted into the Si matrix. The studied energy range was between 300 keV and 13.5 MeV for O and 200 keV - 9 MeV for Be. For the O case, we have determined the range straggling and compared both random stopping and range straggling with current theories. The results for the stopping power, shown in Fig. 4, are in good agreement with similar results obtained previously.

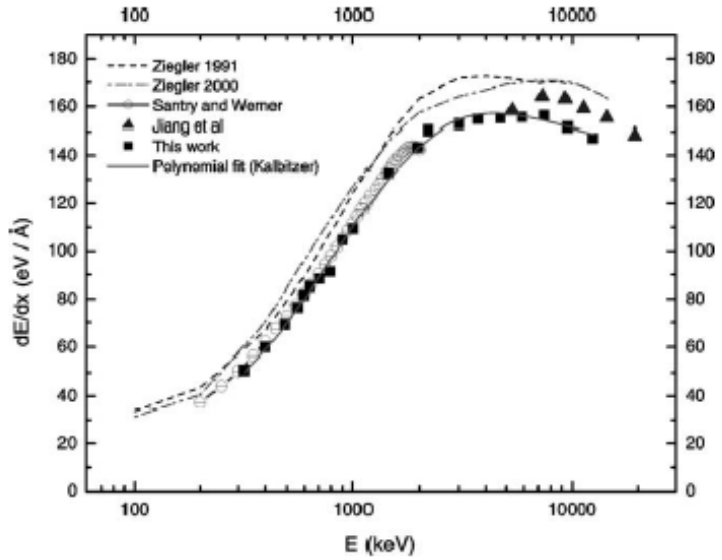

Fig. 4. Random and channeling stopping powers of O and Be into Si. The solid and dashed curves are theoretical predictions.

However, it must be pointed out that the results of [7] are systematically higher than our results. Concerning the straggling results, the data are higher than the Bohr predictions. However, at higher energies, a quite good agreement between theory and experiment is achieved as shown in Fig. 5. These measurements have been published in [8] and [9].

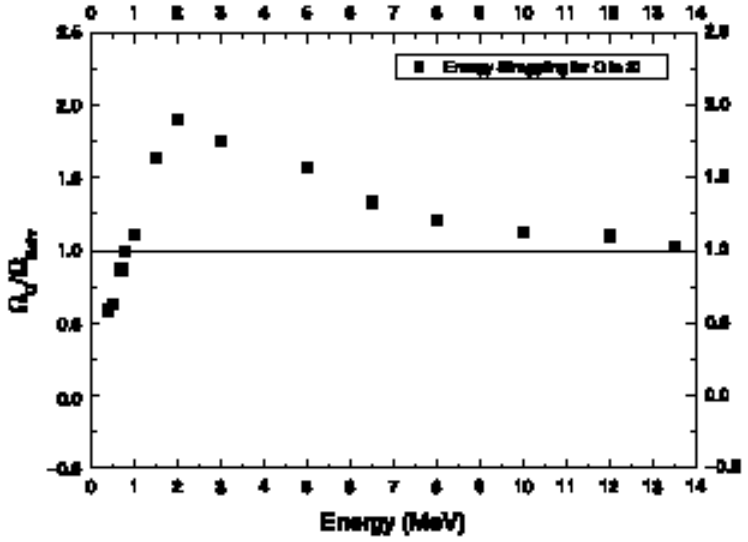

Fig. 5. Ratio of measured range straggling to calculated Bohr straggling for O in Si.

The Be results show that the random stopping power is overestimated by the TRIM predictions by a factor that oscillates between 5 and 12 %. On the other hand, the UCA predictions are lower than the experimental results. This feature indicates that the Barkas effect is very large also for the Be case and might be as large as for the Li case were the relative contribution was of the order of 40-50%. The studied energy interval was between 400 keV and 9 MeV.

5. DETERMINATION OF THE H_2 AND H_3 MOLECULAR STOPPING POWERS

The energy loss of the H_2 and H_3 molecules along the Si <100> and <110> and non-align directions was measured through the RBS technique together with a SIMOX target as specified earlier in this report. The experiments were performed at 300, 500 and 700 keV/amu. The main results are summarized in Table 2. The coherent distance L and the Coulomb explosion σ_{Coul} are also shown in this table. The overall results display three interesting features. First, the random and channeling stopping are larger than the corresponding atomic ones. Second, for a given energy per atom, the H_3 energy loss is larger than the one for H_2. Third, within the experimental error, the channeling and random stropping are equal. According to these results, there are strong indications that the screened Coulomb explosion of the molecule affects the channeling stopping power. These results were published in [10].

Table 2. Summary of results of H_2 and H_3 molecular stopping powers

Energy (keV/atom)	Ion	ΔE^r (keV)	ΔE^c (keV)	L^r (nm)	L^c (nm)	λ (nm)	σ^r_{Coul} (keV)	σ^c_{Coul} (keV)
300	H_2	0.6 ± 0.2	0.5 ± 0.2	17 ± 6	14 ± 6	40	1.5 ± 0.4	1.2 ± 0.4
	H_3	1.3 ± 0.4	1.6 ± 0.4	18 ± 6	22 ± 6		2.4 ± 0.1	2.5 ± 0.2
500	H_2	1.1 ± 0.3	0.8 ± 0.3	41 ± 11	30 ± 11	66	2.3 ± 0.1	1.8 ± 0.2
	H_3	1.9 ± 0.5	2.0 ± 0.5	36 ± 10	38 ± 10		3.6 ± 0.5	3.5 ± 0.4
700	H_2	0.3 ± 0.1	0.3 ± 0.1	14 ± 5	14 ± 5	92	2.4 ± 0.7	2.3 ± 0.7
	H_3	1.2 ± 0.2	0.9 ± 0.2	27 ± 5	20 ± 5		3.6 ± 0.4	3.8 ± 0.4

Note: The superscripts r and c stand for random and channeling, respectively.

6. STRAGGLING OF H IN SiO_2 TARGETS

We have studied the proton straggling in SiO_2 films as a function of the energy. In this study, the transmission technique (in collaboration with the Centro Atomico Bariloche — Argentina) was combined with our own measurements carried out using the Nuclear Reaction Analysis and RBS techniques. To this end, we have used films of SiO_2 and determined the straggling of the protons by comparing the front and back edge of the film. The difference is attributed to the straggling in the film. We have employed the resonant nuclear reaction $^{18}O(p,\alpha)^{15}N$ at 150 keV and for higher energies (between 200 keV and 1.5 MeV) the RBS technique. It should be mentioned that for the energy range that covers the 30 – 600 keV, the transmission technique was used. The experimental results were interpreted on the basis of the so-called bunching effect. The bunching effect is produced by the inhomogeneous distribution of the atomic target electrons participating in the energy loss process. It has been shown previously that this introduces an additional source of energy loss fluctuation, which is similar to the effect produced by foil roughness or target inhomogeneities. Calculations based on the dielectric formalism [5] combined with the bunching effect show a remarkably good agreement with the experimental results, as can be seen in Figure 6.

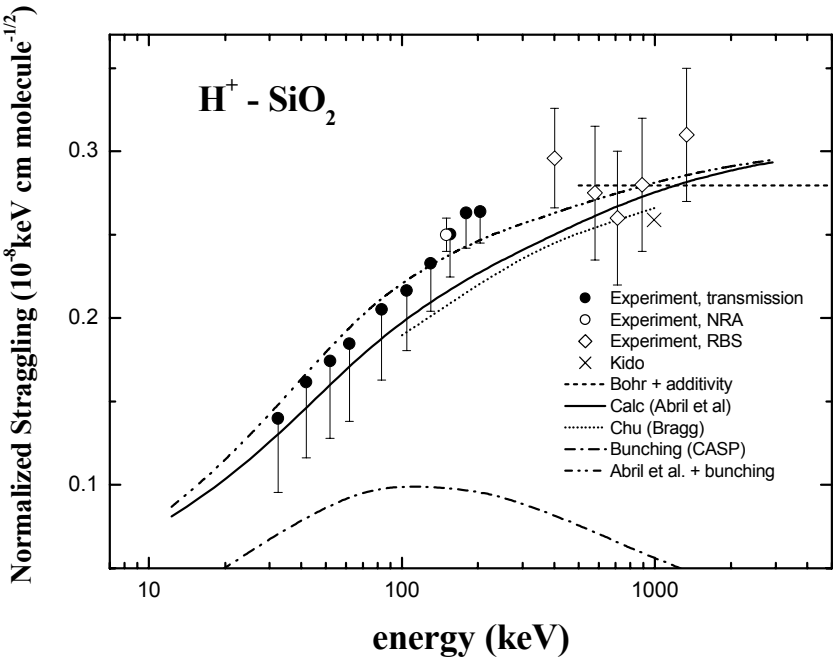

Figure 6. Straggling of H in SiO_2 measured by transmission, NRA and RBS methods. The solid and dashed lines are theoretical calculations using various models.

7. CONCLUSIONS

The random stopping powers of He, Be and O in Si have been measured in the energy range between 200 keV and 13.5 MeV. The results agree well with other published measurements and have been parameterized according to the formula proposed by Kalbitzer and collaborators [3]. The channeling stopping powers of Li, Be and O in Si have also been measured in the energy range from 200 keV to 13.5 MeV. This data show that the Barkas effect can be significant and more theoretical and experimental work must be undertaken to better understand polarization effects during the ion-matter interaction. The energy straggling of protons in SiO_2 has been measured in the range 30 – 1500 keV using transmission, RBS and NRA. There is a good agreement between experimental results and previous theoretical calculations up to 100 keV. Above this, the experimental results are higher. Including the bunching effect in the theoretical calculations results in a much-improved agreement with experiment.

REFERENCES

[1] BEHAR, M., DIAS, J.F., GRANDE, P.L., DOS SANTOS, J.H.R., Electronic energy loss of H_3^+ ion clusters in SiO_2 films, Phys. Rev. A64 (2001) 22904.

[2] DE SOUZA, J.P., BEHAR, M., DIAS J.F., DOS SANTOS, J.H.R., Range parameters of ^{18}O implanted into Si and SiO_2, Nucl. Instr. Meth. B175 (2001) 46.

[3] DOS SANTOS, J.H.R., BEHAR, M., GRANDE, P.L., BOUDINOV, H., STOLL, R., KLATT, CHR., KALBITZER, S., Electronic stopping power of ^{10}B in Si in random and <100> channeling directions. Phys. Rev. B55 (1997) 13651.

[4] BASBAS, G., Inner-shell ionization and the Z13 and barkas effects in stopping power, Nucl. Instr. Meth. B4 (1984) 227.

[5] AZEVEDO, G. DE M., GRANDE, P.L., BEHAR, M., DIAS, J.F., SCHIWIETZ, G., Giant Barkas Effect Observed for Light Ions Channeling in Si, Phys. Rev. Lett. 86, 8 (2001) 1482.

[6] ABRIL, I., GARCIA-MOLINA, R., ARISTA N.R., SANZ-NAVARRO, C.F., Electronic energy loss of swift protons in the oxides Al_2O_3, SiO_2 and ZrO_2, Nucl. Instr. Meth. B190 (2002) 89.

[7] AZEVEDO, G. DE M., BEHAR, M., DIAS, J.F., GRANDE, P.L., DA SILVA, D.L., SCHIWIETZ G., Random and channeling stopping powers of He and Li ions in Si, Phys. Rev. B65 (2002) 75203.

[8] JIANG W., GRÖTZSCHEL, R., PILZ, W., SCHMIDT, B., MÖLLER W., Random and channeling stopping powers and charge-state distributions in silicon for 0.2–1.2 MeV/u positive heavy ions, Phys. Rev. B59 (1999) 226.

[9] ARAUJO, L.L., GRANDE, P.L., BEHAR, M., DOS SANTOS, J.H.R., Random stopping power and energy straggling of ^{16}O ions into amorphous Si target, Nucl. Instr. Meth. B190 (2002) 79.

[10] ARAUJO, L.L., GRANDE, P.L., BEHAR, M., DIAS, J.F., DOS SANTOS, J.H.R., SCHIWIETZ, G., Channeling energy loss of O ions in Si: The Barkas effect, Nucl. Instr. Meth. B193 (2002) 172.

[11] BEHAR, M., COHEN, C., DOS SANTOS, J.H.R., GRANDE, P.L., Energy loss measurements of H_2 and H_3 molecular beams along random and <110> directions of Si, Nucl. Instr. Meth. B190 (2002) 74.

DEPTH PROFILING OF LIGHT ELEMENTS IN CVD AND PECVD Si_3N_4 FILMS AND ANODICALLY OXIDIZED TANTALUM WITH HEAVY ION TIME-OF-FLIGHT ELASTIC RECOIL DETECTION

A. Markwitz, V.J. Kennedy
Institute of Geological and Nuclear Sciences, Lower Hutt, New Zealand

N. Dytlewski
Australian Nuclear Science and Technology Organization, Sydney, Australia

P. Pelicon
Institute "Jozef Stefan", Ljubljana, Slovenia

I.C. Vickridge
Groupe de Physique des Solides, Université de Paris, France

Abstract

Heavy ion time-of-flight elastic recoil detection analysis (TOF-HI-ERDA) technique was used to measure near-surface elemental depth profiles of light and mid-Z elements in thin films of CVD and PECVD Si_3N_4 deposited on silicon and anodically oxidised tantalum. These films are often used as reference materials in ion beam analysis. The great advantage of HI-ERDA is the ability to measure mass-separated elemental depth profiles simultaneously. However, for some materials it is not certain, whether HI-ERDA can be used successfully since significant sputtering or other beam-induced damage may occur. The damage to the surfaces by a 77 MeV iodine beam was assessed with RBS, AFM and profilometry. The results show that for some of the reference films, HI-ERDA gave excellent depth profile information of light elements, including hydrogen, without significantly modifying the material. However, for PECVD Si_3N_4 deposited on silicon a significant modification of the near-surface region is caused by the high-energy iodine bombardment. The investigation showed that reference measurements with additional techniques, such as RBS and profilometry, have to be performed to ascertain sample integrity before HI-ERDA data can be used.

1. INTRODUCTION

Near-surface elemental depth profiles of light and mid-Z elements were measured in a variety of different materials using TOF-HI-ERDA [1–3]. Materials under investigation were thin films of chemical vapour deposition (CVD) and plasma-enhanced CVD (PECVD) silicon nitride (Si_3N_4) deposited on silicon and anodically oxidised tantalum. These specimens often serve as reference standards in ion beam analysis measurements. We examined these films after HI-ERDA measurements to probe for signs of sputtering caused by the high energy heavy-ion beam. HI-ERDA was chosen as analytical technique due to its increasing popularity in becoming a key analytical tool for advanced materials research.

Typically, near-surface alterations are measured with RBS and elastic recoil detection (ERD), resonant and non-resonant nuclear reaction analysis (RNRA and NRA) and particle-induced

gamma ray and X-ray analysis (PIGE and PIXE) [2]. Due to the properties of the elements investigated, often use of one of these techniques alone is not sufficient to describe elemental changes. Therefore, quite complicated procedures have to be developed to amalgamate results obtained with different nuclear techniques. TOF-HI-ERDA offers a solution to this problem. By using a low intensity high-energy heavy particle beam, the depth profiles of a large number of different elements covering a wide mass range can be obtained in a single experiment. Unfortunately, this method comes with the compromise that the near-surface structures may be altered significantly by the impact of the probing beam during the analysis. This may be devastating for some materials. The aim of this paper is to measure quantitatively the influence of a 77 MeV iodine ion beam impinging on surfaces at 22.5º. After the HI-ERDA depth profile measurements, the specimens were analysed non-destructively with RBS using a 1.5 MeV $^4He^+$ ion beam. Profilometry was used as an additional independent method of analysis to determine the material removed by the iodine beam on the nanometre scale. Selected results are presented.

2. RESULTS AND DISCUSSION

2.1. Anodically oxidized tantalum

A set of samples was prepared by anodic oxidation of tantalum in 4% ammonium citrate solution prepared with water of natural ^{16}O isotopic composition. A constant current density of 4 mA cm^{-2} was maintained during the anodic oxidation. After oxidation, an areal density of oxygen of 707×10^{15} cm^{-2} (statistical error 5%) was determined by NRA by comparison with a primary anodic Ta_2O_5 standard. Using a bulk density of 8.2 g/cm^3 for Ta_2O_5, the film thickness is calculated to be 91 nm. Figure 1 shows the resulting HI-ERDA elemental depth profiles of O, N and C of this Ta_2O_5 film. These measurements resulted in a film composition of 27.1% Ta, 71.3 % O, 0.7% N and 0.8% C (statistical and common error of 5%).

Tantalum depth profiles in the near-surface region in the areas inside and outside the HI-ERDA irradiation area were measured with RBS, with results shown in Figure 2. Both these results and those from profilometry confirmed that no significant material removal occurred during the HI-ERDA analysis (limit of detection 5 nm).

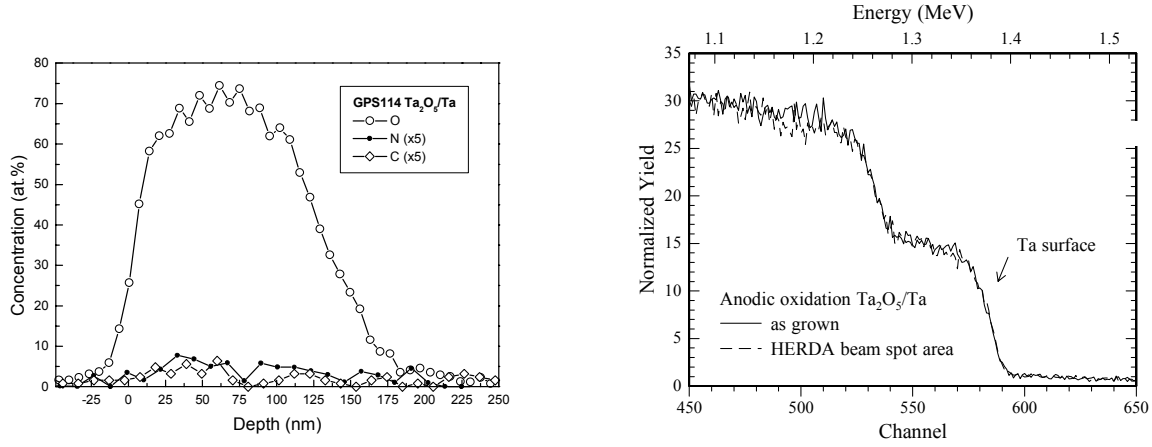

Figures 1 and 2: (1 – left) Oxygen, nitrogen and carbon depth profiles of anodically oxidised tantalum measured with HI-ERDA. (2 – right) RBS tantalum depth profiles in the near-surface region in the areas inside and outside the HI-ERDA irradiation area. The data show that no detectable sputtering of the Ta_2O_5 film occurred by the HI-ERDA measurements.

2.2. CVD Si_3N_4 films on silicon

Thin films of amorphous Si_3N_4 were deposited on Si using standard CVD deposition techniques. For these films, the aim was to optimise the production parameters in such way that nearly oxygen-free films were deposited at low temperature. This is a difficult challenge considering the increased likelihood of forming SiO_2 instead of Si_3N_4 in the presence of nitrogen and oxygen gas impurities. In addition, a certain amount of hydrogen in the films of up to a few percent is desired to saturate dangling bonds. The combination of very low oxygen and moderate hydrogen concentrations in the films result in the outstanding chemical and physical properties of thin Si_3N_4 films. Figure 3 shows the HI-ERDA spectrum of a 250 nm Si_3N_4 film produced with the CVD technique. The film composition is almost uniform with a constant stoichiometric N/Si ratio of 1.3 ± 0.2, a moderate hydrogen concentration of 1.4 ± 0.2 at.% and an oxygen concentration of 0.6 ± 0.2 at.%. However at the surface and the film/substrate interface, oxygen was found to be enriched up to 2.4 ± 0.2 at.%. With HI-ERDA, all four depth profiles are measured simultaneously.

Figure 4 shows the RBS spectrum in the region inside and outside the HI-ERDA irradiation area. A material removal of (120 ± 20) x 10^{15} atoms cm^{-2} corresponding to 13 ± 3 nm was calculated. Using the charge of 1.8 μC for the HI-ERDA measurement, it was calculated from the reduction of film thickness that 2150 atoms were sputtered per incident iodine ion. Similar sputtering yields have been reported for highly charged high-energy iodine bombardment of other advanced materials [4].

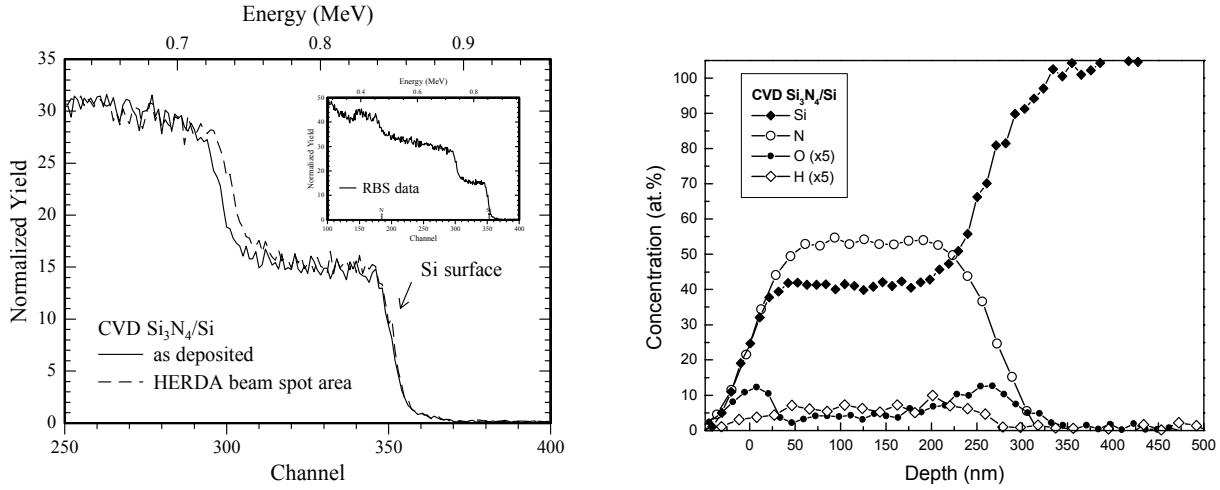

Figures 3 and 4: (3 – left) Silicon, oxygen, nitrogen and hydrogen depth profiles of a CVD Si_3N_4 film measured with HI-ERDA. (4 – right) Reduction in film thickness of 13 ± 3 nm of a CVD Si_3N_4 film after 1.8 μC HI-ERDA measurement. For comparison, the complete RBS spectrum of the as deposited films is shown in the inset.

Profilometry measurements confirmed a reduction in film thickness by showing a step in the line scan from the outside to the inside of the HI-ERDA irradiation area. Surprisingly, the profilometry measurement revealed a reduction in film thickness of 70 ± 10 nm, which is higher than the value measured with RBS by a factor of 5.4. This can be explained by preferential sputtering of nitrogen.

2.3. PECVD Si_3N_4 films on silicon

Plasma enhanced CVD was used to fabricate thin silicon nitride films. Films were produced at 300°C with an operating reactor frequency of 100 kHz under a chamber pressure of 210 mTorr in a radial flow reactor with reactant gases SiH_4 and NH_3 using nitrogen as carrier gas. Figure 6 shows the corresponding HI-ERDA depth profiles of Si, O, N, and H for a film deposited with a NH_3/SiH_4 gas flow ratio of 3.45. As can be seen from these depth profiles, a uniform and equal concentration of Si and N was achieved over the depth of 460 nm. Again, an increased amount of oxygen (5.0 at.%) was measured at the surface. However no significant oxygen concentration was measured in the film and at the interface to the substrate. Figure 5 shows increased hydrogen concentrations, both at the surface and the film/substrate interface. Overall, the hydrogen level in the PECVD film was much higher than in the CVD film. These results, especially the lower than expected nitrogen concentration and the high hydrogen concentration are very useful for understanding the performance of the films.

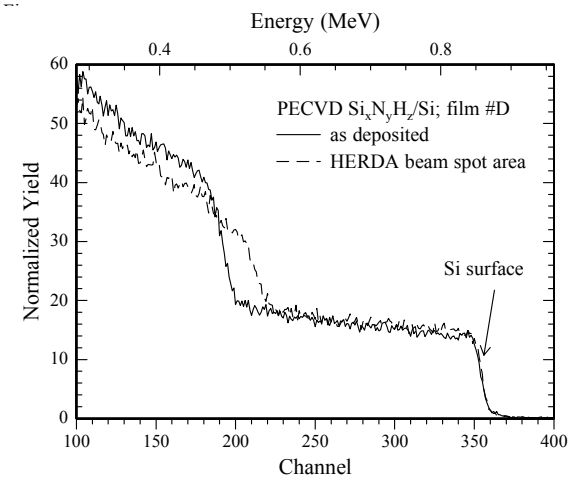

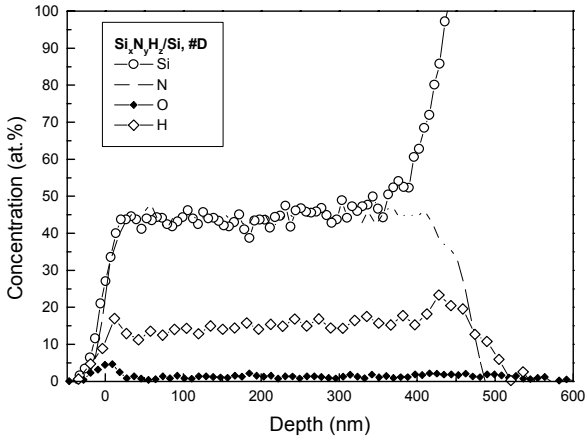

Figures 5 and 6: (5 – left) Silicon, oxygen, nitrogen and carbon depth profiles of a PECVD Si_3N_4 film measured with HI-ERDA. (6 – right) Reduction in film thickness of 37 ± 3 nm of a PECVD Si_3N_4 film measured for 1.8 μC using the silicon signals in the RBS spectra.

The RBS spectrum in Figure 6 shows that the HI-ERDA analysis caused a material removal of (350 ± 20) x 10^{15} atoms cm^{-2} corresponding to 37 ± 3 nm in the HI-ERDA beam spot area. Considering the charge of 1.8 μC for the HI-ERDA measurement, 6200 atoms were calculated to be sputtered per incident iodine ion. This increased factor of 2.9 in sputtering yield over the previous film could be caused by the reduced nitrogen and increased hydrogen concentrations in the PECVD film. Si-H has a bond strength of only 299 kJ/mol, whereas Si-N has a much higher bond strength of 470 kJ/mol.

As in the CVD films, profilometry also confirmed a material removal by the HI-ERDA analysis (160 nm). The increased factor of 4.3 is close to the factor determined for the CVD film suggesting a similar reason for the discrepancy, i.e. preferential sputtering of nitrogen. Atomic force microscopy (AFM) was used to image the surface topology of the as-deposited film and inside the HI-ERDA beam spot. The average surface roughness was calculated to 2.0 ± 0.1 nm. Occasionally, some structure appeared at the surface (typically 10 nm high) that can be attributed to artefacts caused by dust grains sitting on the surface of un-cleaned specimens.

The surface topology changes significantly in the HI-ERDA beam spot. The surface roughness decreased to 0.5 ± 0.1 nm. Furthermore, spike-like structures appeared on the surface. Their average height is determined to 20 – 30 nm, which can be related to the original level of the as-deposited specimen. Both topological effects support the RBS and profilometry measurements showing a partial removal of the film by the HI-ERDA beam resulting in a principally improved surface roughness interspersed with remains of the original surfaces in the form of spikes.

The RBS results indicate that the high-energy iodine beam modifies the nitride films. As a consequence, the information advantage gained by the HI-ERDA analysis is limited. To assure reliable RBS measurements of the silicon nitride films investigated here, a series of spectra was obtained for each RBS measurement; the spectra did not change with charge.

3. CONCLUSIONS

The results show that for anodically oxidised tantalum and some Si_3N_4 films, HI-ERDA gave excellent depth profile information without significantly altering the specimens using a short time of analysis. For PECVD silicon nitride, a significant modification of the near-surface region was caused by the high-energy iodine bombardment. The investigation shows that reference measurements with additional techniques, such as RBS and profilometry, have to be performed before HI-ERDA data can be interpreted. The resulting information can then be used to improve the processes for producing and modifying new near-surface materials.

In materials that are more stable under heavy ion bombardment, such as CVD silicon nitride, HI-ERDA alone can provide valuable information for tailoring materials for particular applications based on the measurement of elemental depth profiles and profile shapes. The HI-ERDA technique is fast — it takes typically less than 15 minutes to measure the elemental depth profiles with reasonable statistics. No sample preparation is required. Large numbers of specimens can be investigated in reasonable time.

ACKNOWLEDGEMENTS

This work was performed under research contracts to the New Zealand Foundation for Research, Science and Technology and research grants from the Australian Institute of Nuclear Science and Engineering (AINSE).

REFERENCES

[1] TESMER, J.R., NASTASI, M., Handbook of Modern Ion Beam Materials Analysis, Materials Research Society, Pittsburgh, PA, USA (1995).

[2] MARTIN, J.W., COHEN, D.D., DYTLEWSKI, N., GARTON, D.B., WHITLOW, H.J., RUSSELL, G.R., Materials characterisation using heavy ion elastic recoil time of flight spectrometry, Nucl. Instr. Meth. B94 (1994) 277.

[3] MARKWITZ, A., WHITE, G.V., Nitridation of silicon oxide layers studied with ion beam analysis on the nanometer scale, Advanced Materials 13 (2001) 1027.

[4] MATSUNAMI, N., SATAKA M., IWASE, A., Sputtering of high T_c superconductor $YBa_2Cu_3O_7$- by high energy heavy ions, Nucl. Instr. Meth. B175–177 (2001) 56.

MICROPROBE ANALYSIS OF LIGHT ELEMENTS IN NANOPOROUS SURFACES PRODUCED BY HELIUM ION IMPLANTATION

V.J. Kennedy, A. Markwitz
Institute of Geological and Nuclear Sciences, Lower Hutt, New Zealand

P.B. Johnson, C.R. Varoy
University of Wellington, New Zealand

K.T. Short
Australian Nuclear Science and Technology Organization, Sydney, Australia

Abstract

Helium ion implantation into surfaces can be used to form nanoporous cavity structures with unique features of interest for applications. The ingress of desired dopant atoms into the material could be enhanced by producing cavity layers that extend to the surface. Ti and Co targets were implanted with He using pulsed Plasma-Immersion Ion-Implantation ($PI^{3\ TM}$) and monoenergetic accelerator ion implantations. Spatially resolved elemental mapping of C, N and O, using microprobe NRA was done with a scanned 20 μm diameter deuteron beam. This spatial resolution has enabled several important new results to be obtained. It is demonstrated for the two materials that He implanted surfaces take up more O from the atmosphere than unimplanted surfaces. In Ti, the nanoporous surface exposed by heavy ion damage in a prior HI-ERDA measurement takes up twice as much O and over ten times as much N as the immediately adjacent undisturbed He implanted surface.

1. INTRODUCTION

For many materials, nanoporous layers with unique features can be formed near the surface by energetic He-ion bombardment to high fluence [1–4]. The implanted He gathers into small gas bubbles which grow and coalesce to form the nanoporous structure. Such layers are attracting interest in relation to applications, either directly or through the compounds that can be formed on them by diffusing desired dopant atoms into the highly cavitated layer. The modified layer is formed as an integral part of the material with the potential for a smooth change in composition and structure over a relatively broad depth region spanning a few hundred atomic layers between the implanted layer and the unmodified material beneath.

In this case the nanoporous layer is formed as a buried layer below the surface and further processing, such as ion beam milling, will probably be needed to remove the overlying material to allow the ingress of the selected dopant atoms. An alternative approach being considered is to use an implantation protocol, employing a combination of He energies and doses that produces a nanoporous layer that intersects the surface, so dopant atoms can be diffused directly into the ‘as-implanted’ surface without further processing.

In investigating the relative merits of these two approaches [3–5] a number of complicating factors have been encountered. These include: (i) The degradation of the nanoporous layers

under study resulting from the heavy-ion bombardment involved in light atom depth-profiling using HI-ERDA (heavy ion elastic recoil detection analysis) [7]. (ii) The casual loading of O, C and N from the local environment into the structures during subsequent storage, analysis and processing of the implanted foils. (iii) The differences in the uptake of light atoms resulting from differences in the chemical reactivity of the substrate material. (iv) The differences in response between different foils of the same material. Recent studies aimed at clarifying these factors have measured light atom depth-profiles using IBA (RBS, HI-ERDA and NRA) employing broad probing ion beams several millimetres in extent [3–5]. In the present work we investigate the information that can be gained by using microprobe NRA techniques initiated with a scanned 20 μm diameter deuteron beam to provide spatially resolved elemental mapping of C, N and O.

2. EXPERIMENTAL

In the course of these studies Ti and Co targets have been implanted with He using pulsed Plasma-Immersion Ion-Implantation, PI^3 [2–7]. The metal targets were in the form of polished, annealed, high purity polycrystalline foils. The PI^3 implantations were at several different dose levels and at several different energies up to 40 keV. Also implantations employing several different energies in sequence have been investigated. Some additional He implantations to greater depth were carried out using an ion-accelerator. The helium energy was 160 keV with an oblique angle of incidence of the helium beam (60° to the surface normal) to increase the thickness of the modified layer.

Nuclear Reaction Analysis (NRA) measurements were carried out in the nuclear microprobe facility at Institute of Geological and Nuclear Sciences (GNS) using 0.920 MeV deuteron beam focused down to 20 μm and scanned over 1 x 1 mm^2. Target chamber vacuum during the microprobe analysis was $2x10^{-6}$ Torr. The beam current at the target was 2-3 nA. The nuclear reactions $^{16}O(d,p_1)^{17}O$ (E_p = 1.39 MeV, $d\sigma/d\Omega$ = 4.6 mb/sr), $^{14}N(d,\alpha_1)^{12}C$ (E_α = 5.63 MeV, $d\sigma/d\Omega$ = 0.9 mb/sr) and $^{12}C(d,p_o)^{13}C$ (E_p = 2.7 MeV, $d\sigma/d\Omega$ = 55 mb/sr) were used to determine the concentrations of C, N and O. The relative cross-section values of C, N and O mentioned above were used to calculate the normalised yields in Figs. 2 and 3. Standard samples of Ta_2O_5 and TiN were used for calibration purposes.

3. RESULTS

The levels of C, N and O have been determined in three areas of each target examined: an unimplanted region masked during the implantation, the implanted area and the part of the implanted area exposed to the heavy ion beam (77 MeV iodine beam, current 2.5 pA) during HI-ERDA analysis (beam spot size 0.5 cm^2). Elemental maps for these three elements are obtained for selected areas spanning each of the two boundaries unimplanted/implanted and implanted/HI-ERDA spot in turn. From the elemental maps, representative lines normal to each boundary are chosen and higher sensitivity line scans for the three elements of interest are taken.

In Co foils eighteen months after implantation with He in a charged particle accelerator, patches of lighter contrast, approximately 100 μm across, could be seen on the surface with the aid of an optical microscope. These patches were visible well beyond the implanted region. The microprobe measurements described here were undertaken to measure the spatial

uniformity of the C, N and O distributions on the surface and examine whether the patches of lighter contrast correlated with enhanced levels of one or more of these three elements.

Elemental maps for C and O, taken spanning the boundary between the implanted and unimplanted regions, are shown in Fig. 1. The position of the boundary (as identified from an optical micrograph) is indicated on this figure.

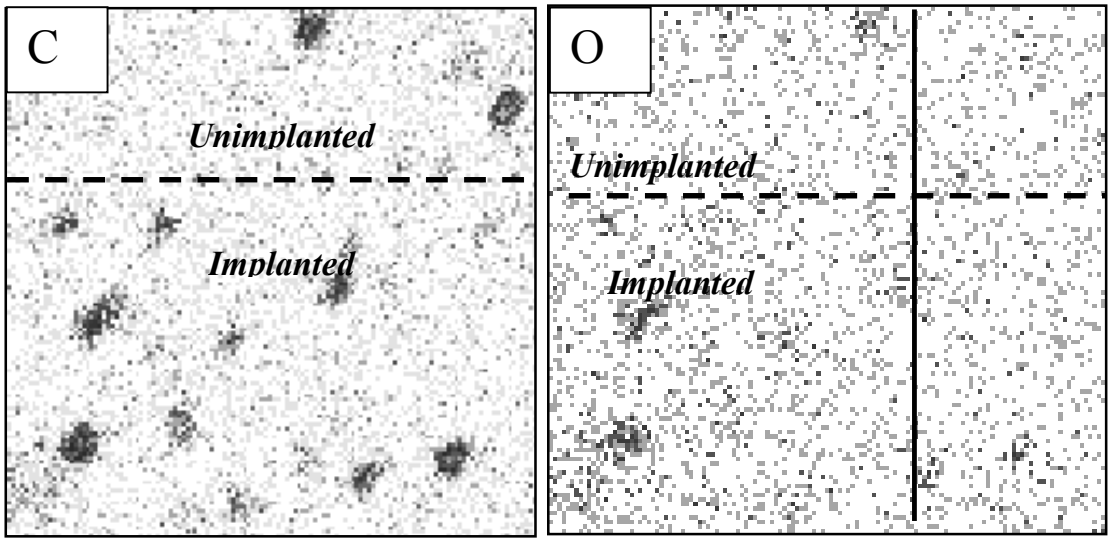

Figure 1. NRA microprobe elemental maps for C and O in a Co foil. Scan size is 1 x 1 mm^2. Increase in concentrations from white to black. The dashed line indicates the boundary between the unimplanted and He implanted areas. The line in the O map indicates the typical line scan axis.

The levels of nitrogen on either side of the boundary were found to be negligible. Close inspection of these maps showed that there was no correlation between the patches of light contrast seen optically and elevated levels of these three elements. Notice also that the boundary is not delineated in these light element maps. A feature of these maps is the isolated small spots, < 50 μm across, distributed randomly on the surface. They are at similar concentrations in the implanted and unimplanted regions but are more evident in the carbon maps than in the oxygen maps. These spots are attributed to carbon contamination during storage and handling. Only some of these spots (~ 30 %) are evident in the oxygen map. This suggests the deposits giving rise to the spots in the oxygen map may result from subsequent oxidation of some of the carbon deposits. A line scan (not shown) taken through one of these oxygen containing deposits showed the presence of approximately equal concentrations of carbon and oxygen.

To obtain line scans that are truly representative of the helium-implanted surface, sites were chosen in featureless areas of the maps so as to avoid any obvious contaminant spots. Such a representative line scan across the boundary is shown in Fig. 2.

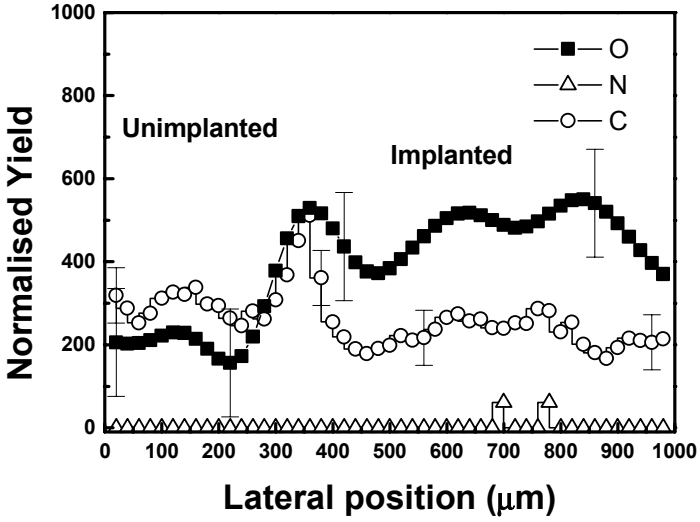

Figure 2. NRA microprobe line scan for a Co foil across the boundary between the unimplanted and He implanted areas. The error bars are calculated based on one standard deviation line scan axis.

Line scans are approximately fifty times more sensitive than maps taken over the same time period and so can reveal much smaller variations in composition. Outside the implanted region the levels of carbon and oxygen are comparable. In the implanted region, away from the boundary, whereas the carbon level is slightly lower than in the unimplanted region, the oxygen level is greater by a factor of approximately three. There is also a peak in the oxygen near the boundary, which corresponds to the peak in the carbon. At the peak there are approximately equal concentrations of carbon and oxygen, although the absolute levels are very low compared with those in the spots identified in the oxygen map above.

Many of our previous studies e.g. [1–5] have included Ti because of the interest in this metal for biomedical applications. Titanium dioxide is recognised as a bio-compatible material and so the oxidation behaviour of Ti is of particular interest. Analysis using broad-beam IBA techniques has shown Ti, even when highly polished, readily forms an oxide [2–4]. This results in it being more difficult to clearly identify the effects of He implantation than is the case for the less reactive substrates such as Mo, Co and Si [4].

The microprobe examinations reported here are for a particular Ti target that was treated in a sequence of single-energy PI^3 implantations to high fluence at three different energies: 40 keV, 20 keV and 6 keV to produce a highly cavitated surface layer. The fluences were respectively (in units of 10^{17} He/cm^2) 8, 6 and 4. The aim of the microprobe measurements reported here was to measure with better spatial resolution the light atom loadings in the three differently treated areas of this target after six months exposure to the laboratory environment at ambient temperature. A line scan taken across the boundary between the implanted region and the unimplanted (masked) area is shown in Fig. 3(a). Whereas the O loading in the implanted region is approximately twice that in the unimplanted region, there is little change in the C level between the two areas. This result for C supports an earlier conclusion [4] that the source of the C is not the result of unintended co-implantation from the plasma during the PI^3 He implantation. A line scan across the boundary between the implanted region and the HI-ERDA spot is given in Fig. 3(b). Here the O loading in the HI-ERDA spot is twice that in the He implanted area.

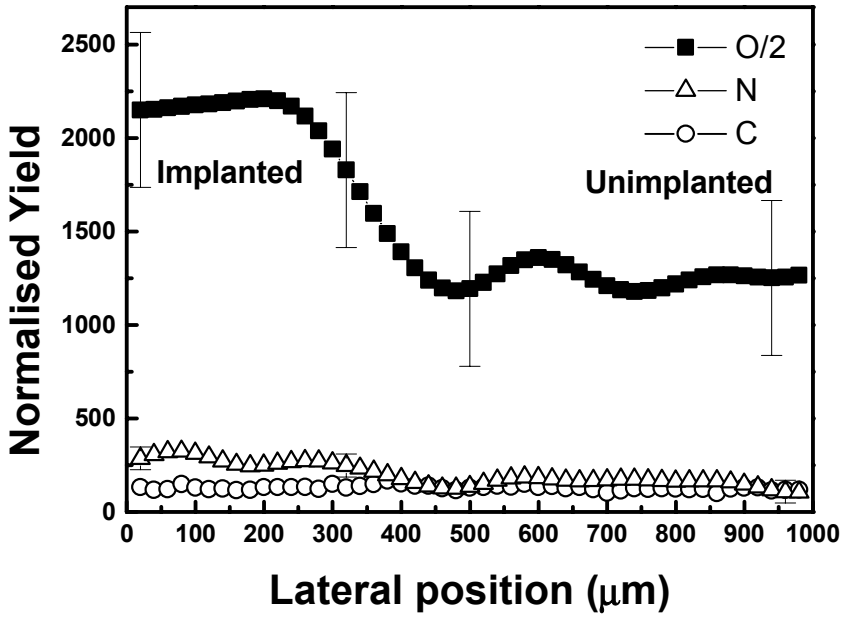

Figure 3(a). NRA microprobe line scans for a Ti foil across the boundary between the unimplanted and He implanted regions. The oxygen data are divided by a factor of two. The error bars are calculated based on one standard deviation.

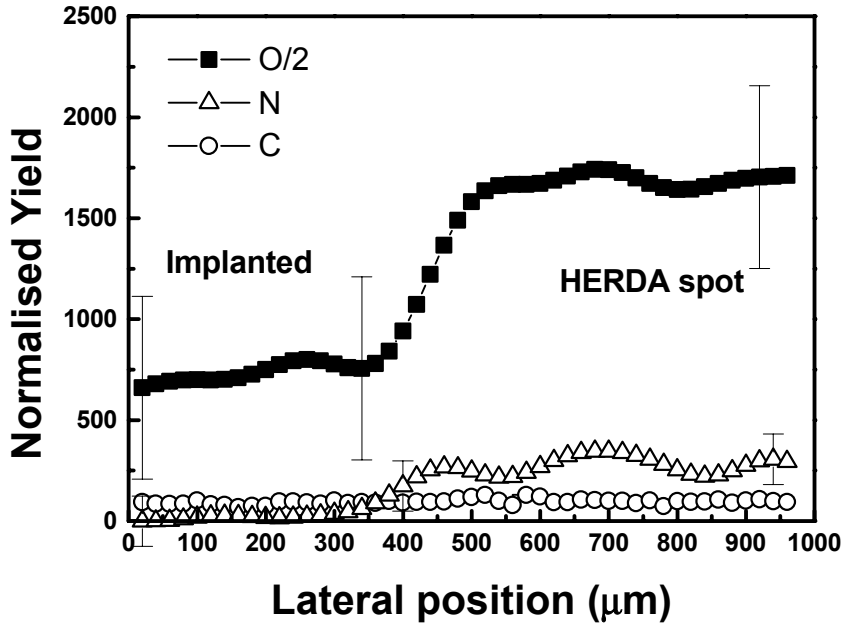

Figure 3(b). NRA microprobe line scans for a Ti foil across the boundary between the He implanted region and the HI-ERDA beam spot. The oxygen data are divided by a factor of two. The error bars are calculated based on one standard deviation.

Again there is little difference in C levels. The level of N in all three areas is low. A SEM micrograph taken at the perimeter of the HI-ERDA spot on the surface of the heavily implanted Ti foil, shows that the entire HI-ERDA spot is essentially a flat bottomed crater. The crater edge consists of a relatively undamaged surface plate (~ 230 nm thick) overlying a highly damaged buried layer beneath. The crater floor revealed that the surface plate has been removed by the HI-ERDA beam and has a highly damaged appearance consistent with the surface plate separating from the substrate approximately through the middle of the buried nanoporous layer. It is presumed that this separation leaves behind an exposed nanoporous layer. Other Ti foils give the same response provided the helium implantation protocol used is the same. The NRA microprobe results of Fig. 3. show this exposed surface has about twice the O loading of the He implanted surface and approximately four times the loading of the unimplanted surface. This contrasts with the negligible levels of O found in the HI-ERDA spot six months earlier and shows that the O in this region has been taken up from the atmosphere at ambient temperature. In between IBA measurements, samples were stored in a clean sealed compartmentalised box with normal laboratory atmosphere.

4. CONCLUSIONS

It is clear from these results that the He implantation protocol used here is producing a buried nanoporous layer separated from the surface by a plate of less damaged Ti. It is evident that this surface plate is limiting the diffusion of O into the nanoporous layer below. Whereas SEM examination shows the crater edge is very sharply defined, the microprobe results show that the O loading changes relatively slowly at the boundary over a transition region ~ 200 μm. The width of this region suggests that O may be diffusing laterally into the nanoporous layer covered by the surface plate outside the HI-ERDA spot.

In the study of He implanted surfaces, microprobe IBA techniques provide valuable information that cannot be obtained using broad-beam techniques. The advantages are readily apparent when examining, on the same foil, different areas that have received different treatments. By making measurements on a single foil, uncertainties associated with possible differences in foil characteristics can be eliminated. The relative uptake of light atoms such as O in the different areas can be determined with improved reliability by obtaining spatially resolved elemental maps and line scans across boundaries between the areas. The maps allow representative sites to be selected for the higher sensitivity line scans. Since the analyzing ion beam samples both areas in the same analysis, uncertainties arising from possible variations in beam analyzing parameters are avoided.

ACKNOWLEDGEMENTS

This work was performed under research contracts to the New Zealand Foundation for Research Science and Technology (CO5X0008 and VICX0001) and research grants from the Australian Institute of Nuclear Science and Engineering (AINSE). We thank Dr George Collins and Dr Nick Dytlewski of ANSTO for many useful discussions and research assistance.

REFERENCES

[1] JOHNSON, P.B. MARKWITZ, A., GILBERD, P.W., Shallow nanoporous surface layers produced by helium ion implantation, Advanced Materials, 13 (2001) 997.

[2] JOHNSON, P.B. MARKWITZ, A., GILBERD, P.W., TROMPETTER, W.J., COLLINS, G.A., SHORT, K.T., COHEN, D.D., DYTLEWSKI, N., Oxygen and hydrogen profiles in metal surfaces following plasma immersion ion implantation of helium, Surface and Coatings Technology, 136 (2001) 217.

[3] MARKWITZ, A., JOHNSON, P.B., GILBERD, P.W., COLLINS, G.A., Ion beam analysis of light elements in nanoporous surfaces produced by single- and multiple-energy helium ion implantation, Nucl. Instr. Meth. B190 (2002) 718.

[4] JOHNSON, P.B., KENNEDY, V.J., MARKWITZ, A., VAROY, C.R., DYTLEWSKI, N., SHORT K.T., Uptake of light elements of nanoporous layers formed by helium ion implantation, Nucl. Instr. Meth. B206 (2003) 1056.

[5] MARKWITZ, A., JOHNSON, P.B., GILBERD, P.W., COLLINS, G.A., COHEN, D.D., DYTLEWSKI, N., Ion beam analysis of nanoporous surfaces produced by He-implantation and oxidised by plasma-immersion ion-implantation, Nucl. Instr. Meth. B161-163 (2000) 1048.

[6] MARTIN, J.W., COHEN, D.D., DYTLEWSKI, N., GARTON, D.B., WHITLOW, H.J., RUSSELL, G.J., Materials characterisation using heavy ion elastic recoil time of flight spectrometry, Nucl. Instr. Meth. B94 (1994) 277.

[7] COLLINS, G.A., HUTCHINGS, R., SHORT, K.T., TENDYS, J., Ion-assisted surface modification by plasma immersion ion implantation, Surface and Coatings Technology 104 (1998) 212.

LIGHT ELEMENT CONCENTRATIONS AND DEPTH PROFILES IN SILICON NITRIDE AND ALUMINIUM OXYNITRIDE THIN FILMS

P. Pelicon, A. Razpet, M. Budnar, I. Čadež, Z. Rupnik, J. Simčič
Institute 'Jožef Stefan', Ljubljana, Slovenia

M. Klanjšek Gunde
National Institute of Chemistry, Ljubljana, Slovenia

M. Maček
University of Ljubljana, Ljubljana, Slovenia

Abstract

RBS and conventional and heavy ion ERD have been used to evaluate their potential for determining the stoichiometry of Si:N:H thin films. These techniques have been applied to measure the thickness and stoichiometry of thin aluminium oxynitride films as part of an intercomparison exercise. Time-of-flight ERD has been developed as an additional analytical tool.

1. INTRODUCTION

The ability of quantitative depth profiling of light elements with fast ions has a very important advantage compared to other analytical methods. It is a demanding issue for each Ion Beam Analysis laboratory to provide calibrated methods for depth profiling of light elements. The participation in the CRP stimulated us to improve already existing analytical techniques in the laboratory and encouraged us during the development of the Time-Of-Flight ERDA (TOF-ERDA) telescope.

Areas of Institute 'Jožef Stefan' (IJS) engagement within the CRP

1. Silicon nitride thin films: production, characterization, distribution of sets containing six samples to other laboratories for the round-robin measurements, final data evaluation.
2. Development of a TOF-ERDA telescope.
3. Testing the impact ion dose measurement methods and construction of the mesh integrator.
4. Measurements on the samples obtained from other laboratories.

2. DESIGN AND DEVELOPMENT OF TOF-ERDA METHOD AT IJS

Time-of-flight (TOF) telescopes are successfully used for ion identification in elastic recoil detection analysis (ERDA) [1–3]. Few TOF setups are operating at accelerators with terminal voltages around 2 MeV, although it was shown that this is the only efficient ERDA method that enables ion separation with the beams available from low energy ion accelerators [4]. The beam usually used at the accelerators with terminal voltages of 2 MeV is 10 MeV Cl^{5+}. The

main disadvantages of TOF-ERDA analysis under these conditions are smaller penetration depths and lower detection efficiency for light elements.

The TOF-ERDA telescopes usually consist of start and stop time detectors and an energy detector. Time detectors often follow an electrostatic mirror design by Bush et al. [5] that includes three tungsten grid electrodes, a carbon foil as a secondary electron source and a microchannel plate producing a fast timing signal. The grids that reflect secondary electrons to the microchannel plate lowers the ion transmission through the telescope, and increases the number of false timing signals, causing a degradation of the time resolution. Within this project, a time detector in annular geometry was designed and optimized for operation with 10 MeV Cl^{5+} beam [6].

A carbon foil with a thickness of 10 μg/cm^2 was set perpendicular to the ion path in order to minimize energy spread due to differences in flight distance. Secondary electrons emitted from the foil at ground potential are then accelerated by voltage applied between the foil and the extraction electrode [6]. After passing through the central hole (8 mm diameter for the start detector), they are reflected on the active surface of an electron detector (microsphere plate) by the mirror electrode biased at a negative voltage.

The stop detector of our TOF telescope is identical to the start detector, but instead of an additional carbon foil, the gold entrance window of surface barrier detector is used for secondary electron production. The central hole through the stop detector has a diameter of 16 mm. An advantage of using only one carbon foil is an improvement of the system energy resolution that is influenced by the energy straggling and variations of energy loss due to non-uniform thickness of the carbon foils. It was also shown that the detection efficiency for the stop detector was improved since the secondary emission from gold is higher than from carbon.

The TOF telescope is mounted on the experimental chamber at an angle of 38.6° relative to the primary beam. The flight distance between the timing stations is 75 cm, the distance between the sample and the start detector is 30 cm and the solid angle is defined by the diameter of the central hole of the stop detector is 0.2 msr. Signals from the time detectors are led first to the constant fraction discriminators. As is common in other set-ups, the signal from the start detector is delayed for a constant time t_0 and the difference t_0-t, instead of t, is measured to avoid triggering due to signals from the start detector without corresponding stop event. A signal, proportional to the time difference is created by a time-to-amplitude converter. The data acquisition system includes two analog-to-digital converters and a coincidence unit built in-house. Events that are simultaneously recorded by the TOF telescope and the energy detector are recorded in a 2D histogram.

The time resolution of the TOF telescope consists of two contributions:

$$\Delta t^2=(l\,\Delta E)^2/8\,(m/E)^3 + (\Delta t_{\mathrm{int}})^2,$$

where E and m are the energy and mass of the ion, t_{int} is the intrinsic time resolution of the entire spectrometer, and ΔE the energy spread of ions entering the start detector. The intrinsic resolution was estimated to 300 ps, but the main factors increasing Δt were found to be the geometric energy spread and the energy spread due to non-uniform foil thickness [6]. The smallest mass difference that can be separated in the region of oxygen calculated from the above expression, is approximately 0.5 amu.

The TOF-ERDA performance was tested in experiments with a 9.6 MeV Cl^{5+} beam. The sample was a 200 nm thin layer of SiO_2, enriched by ^{18}O on a silicon backing. The isotopes of oxygen were completely separated and the background in the 2D spectrum is low [6]. The detection efficiency for surface oxygen is approximately 0.40.

The main goal of the present construction of the timing stations was to avoid acceleration grids in the time detector. The 'fountain' geometry enabled us to use of gold layer of the surface barrier detector as the secondary electron source. The results of these improvements are higher detection efficiency, higher energy resolution, low background, and excellent mass resolution of the system.

3. THE CONSTRUCTION OF THE IN-BEAM CHARGE COLLECTOR

The device constructed as part of this work belongs to the in-beam charge collection type of devices. A fine tungsten mesh (wire diameter of 38 microns, density 3.2 lines/mm) on an annular holder, enclosed by two negatively biased apertures, is used to collect the amount of charge proportional to the total charge of the transmitted beam. The transmitted beam has to be released without further obstructions to the target. Due to the fine structure of the mesh, it permits the intensity variations of the beam across its cross-section to be accounted for. The beam-shaping slit is added as the first aperture in the stack of electrodes to define the shape and position of the beam at the target. We performed a series of measurements to define the optimal bias voltage and to check for the charge collection stability. We routinely operate this charge collector device at bias voltage of -900 V. The reproducibility of the measurements with 4.2 MeV $^{7}Li^{2+}$ ions is better than 2 %. This in-beam charge collector was used to measure the impact dose in experiments described in the following sections of this report.

4. SILICON NITRIDE THIN FILMS

The electrical properties of thin silicon nitride layers are strongly affected by presence of hydrogen. Large amounts of hydrogen are introduced during the Plasma-Enhanced Chemical Vapour Deposition (PECVD), the standard production process for silicon nitride films [7].

For the analysis of silicon nitride thin films, RBS and hydrogen ERDA with Al absorber foils have been applied simultaneously. The stoichiometry ratio between Si and N could be well determined by fitting the RBS spectra, whereas H concentration could be obtained from ERDA spectra. Due to the low sensitivity of RBS analysis for elements with low Z (N, O, C) we were able to determine the absolute stoichiometry of the films only, if we assume the exclusive presence of Si, N and H in the film. As demonstrated in the measurements with Heavy Ion ERDA, the assumption is correct for all the films distributed in the round-robin measurements.

4.1. The RBS/ERDA set-up

Samples were attached to the goniometer and put into the RBS/ERDA chamber. For the simultaneous RBS and ERDA measurements, targets were rotated with respect to the beam direction. The orientations of the sample and the two ion detectors are presented in Fig. 1.

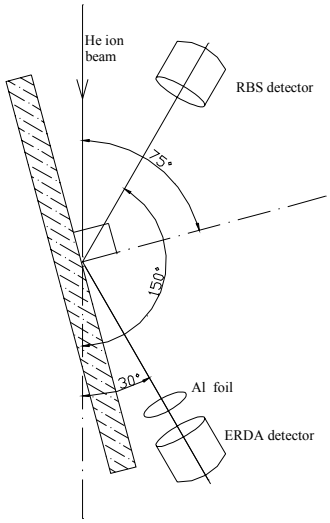

Figure 1. RBS/ERDA setup. Al foil thickness: 14 μm for measurements with 3.3 MeV He beam, 11 μm for measurements with 4.2 MeV $^{7}Li^{2+}$ beam. Target tilt as well as the detector angles could be varied from the air side of the chamber with precision of 1 angular degree.

4.2. RBS/ERDA data evaluation

4.2.1. RBS/Hydrogen ERDA with 3.3 MeV He beam

Measured spectra were evaluated using the SIMNRA [8] code (Fig. 2). Three layers have been used for the target description:

1. Thick Si:N:H layer,
2. Thin Si:N:H layer with the same Si:N atomic ratio, but with reduced H concentration,
3. Bulk Si layer.

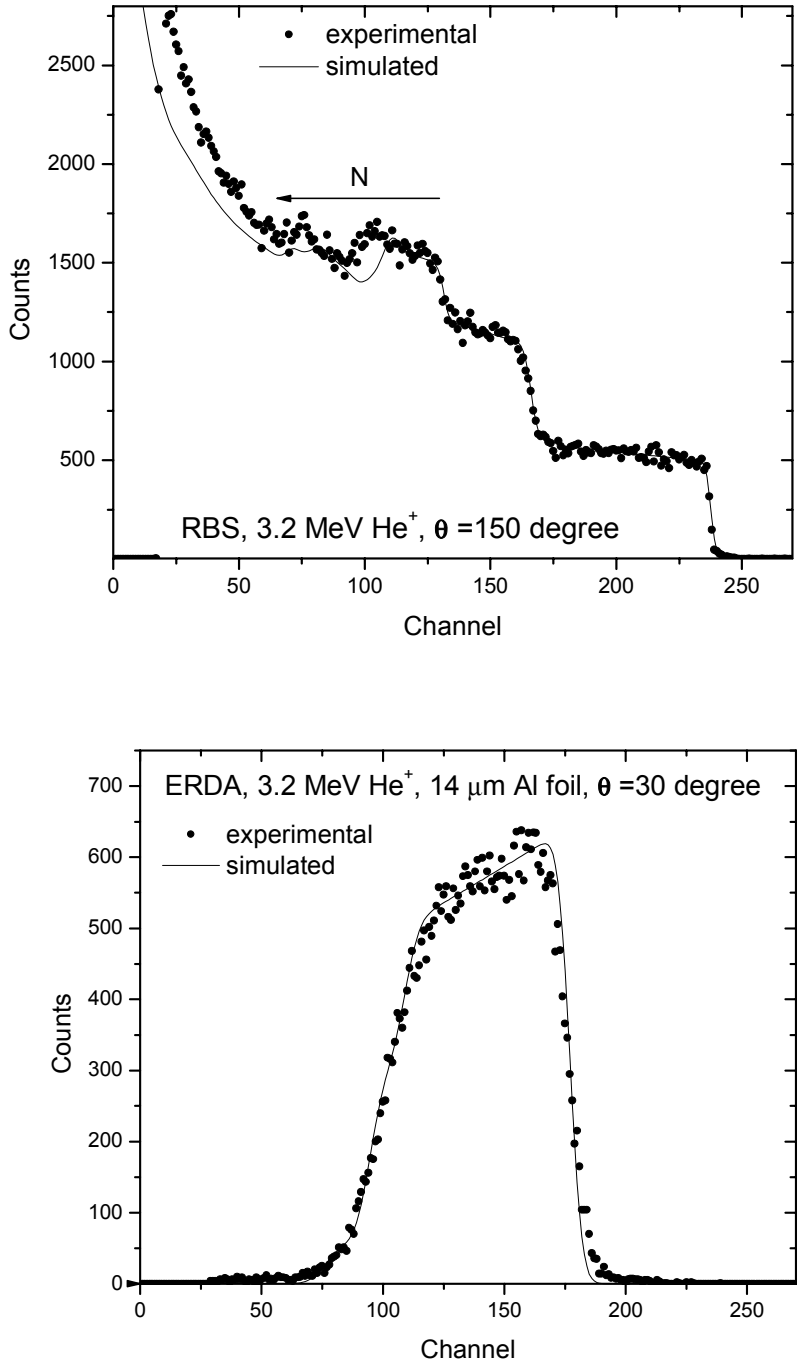

Figure 2. RBS and ERDA spectrum measured by a 3.2 MeV He beam on the sample E distributed by IJS within the round-robin measurements on silicon nitrides. The nitrogen contribution in the RBS spectrum could not be well simulated due to unavailable scattering cross section at 150 degree. See the results of round-robin tests for the composition of the simulated layers.

The impact ion dose has been determined by fitting the Si plateau in RBS spectra originating from the substrate.

For the reaction H(α,p)α at the recoil angle of 30°, the following cross-sections were compared:

1. Baglin, 1992, [9] energy range 1000-3000 keV,
2. Quillet, 1994, [10] energy range 1000-2500 keV,
3. CRSDA.DAT, No. 3, compiled experimental cross sections, best fit, IPP Garching [8], energy range 2000-7000 keV.

The difference in the cross-section data between the first two references is significant, i.e. at the energy of 2500 keV, values 343 and 278 mb/sr are given, correspondingly, which result in a systematic error of 20 % in the determination of hydrogen concentration. The third reference gives a cross-section of 320 mb/sr. For the evaluation we use the following values: energy range 0-999 keV- Rutherford cross section, energy range 1000 keV-1999 keV- Baglin values [9], energy range 2000 keV-7000 keV- values from the file CRSDA.DAT, IPP Garching [8].

Both silicon and hydrogen concentration profiles show, that the stoichiometry of the Si:N:H layers remains quite constant within entire thickness of the films excluding interfaces. The results are given in the report of the round-robin measurements on SiN thin films [the following report in this TECDOC].

4.2.2. RBS/Hydrogen ERDA with a 4.2 MeV ^{7}Li beam

In the last year of the CRP, the RBS/ERDA measuring chamber has been equipped with a mesh charge collector positioned in the beam after the shaping slit and 0.5 m before the target. Impact ion dose is measured with a precision better than 2 % (Section 3). The cross-section H(^{7}Li,p)^{7}Li at a detection angle of 30° is not given in any experimental database. To overcome this serious problem, we evaluated measured spectra using polyimide (Kapton™) correction. The method uses a thick hydrogen-containing standard sample for the evaluation of the hydrogen depth concentration profiles from the spectra measured on unknown samples. RBS/Hydrogen ERDA by 4.2 MeV $^{7}Li^{2+}$ ions has been calibrated and applied to the samples exchanged within the framework of CRP (Fig. 3 and 5).

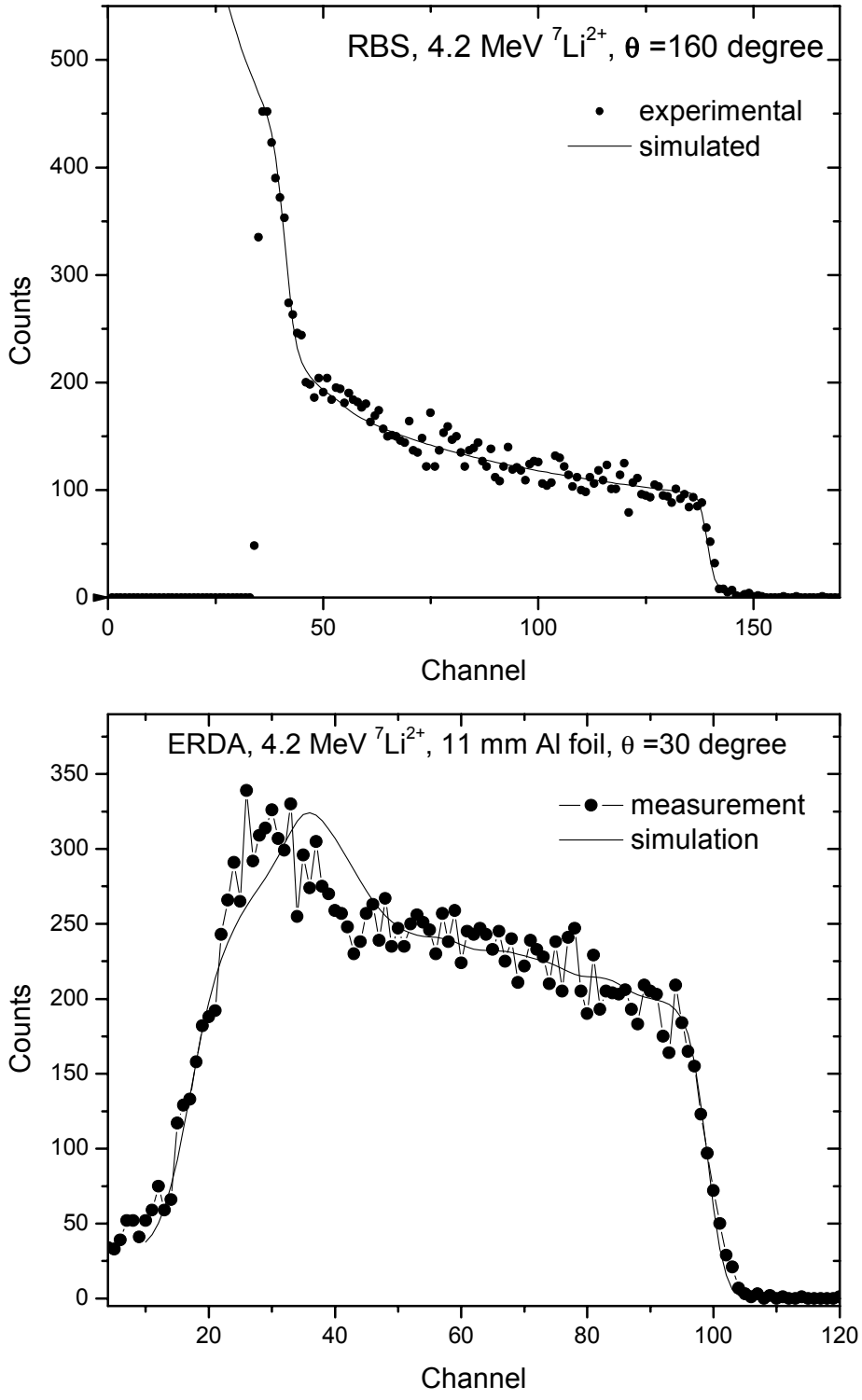

Figure 3. RBS and ERDA spectrum measured by 4.2 MeV ^{7}Li beam on sample E distributed by IJS within the round-robin measurements on silicon nitrides. Simulated sample composition as obtained by He RBS/ERDA, ion dose as measured by mesh charge collector. ERDA simulation is obtained by polyimide (Kapton™) correction.

4.2.3. Additional characterization of the SiN samples

The hydrogen concentration in the distributed set of PECVD SiN samples has been measured by NRA using the $^{15}N(p,\alpha\gamma)^{12}C$ resonant reaction at 6.385 MeV. Measurements have been carried out in the Research Centre Rossendorf, Germany, on the instrumental set-up described in [11]. The depth concentration profiles are shown in Fig. 4. Results show constant depth concentration profile of hydrogen in the samples distributed. The atomic concentration of hydrogen is not dependent on the gas flow ratio during the PECVD process.

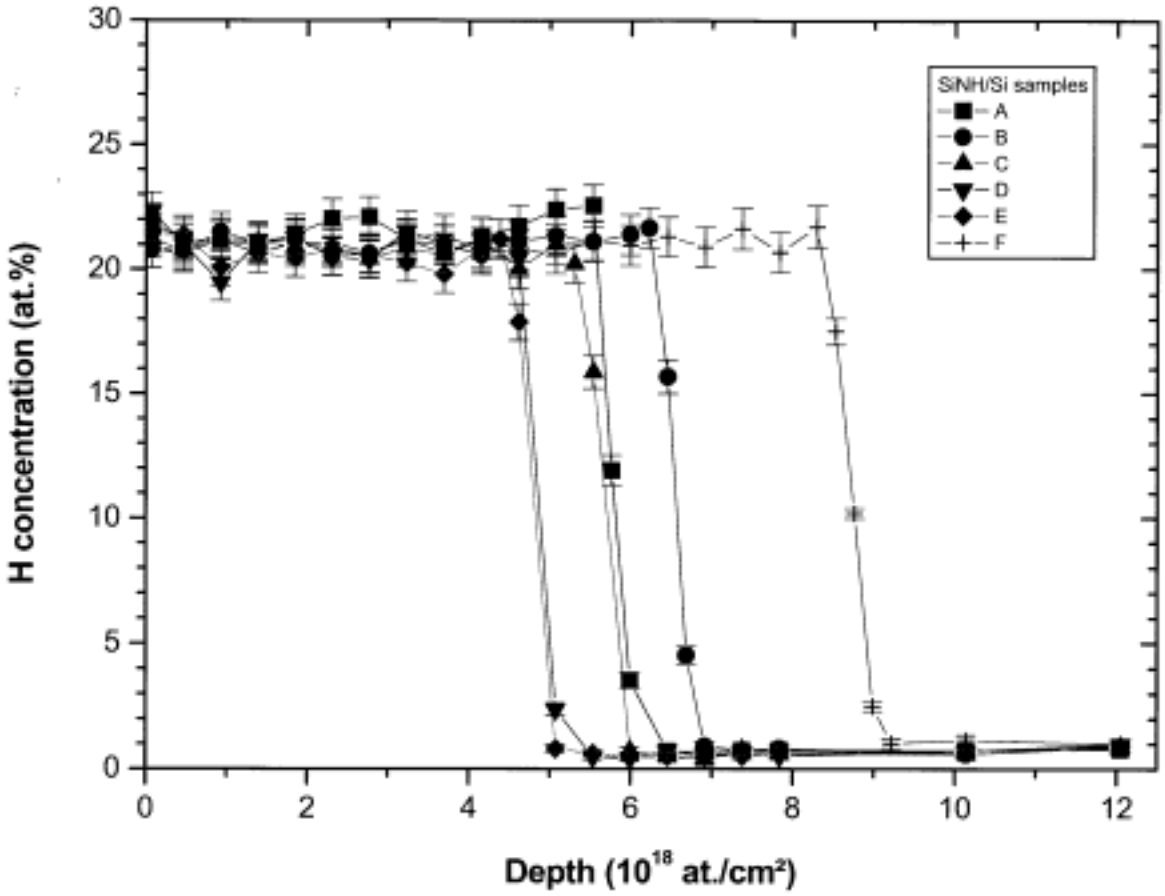

Figure 4. Hydrogen depth concentration profiles in the set of six SiN samples, distributed within the CRP, obtained with ^{15}N NRA method in Research Centre Rossendorf, Germany.

5. MEASUREMENTS ON THE SAMPLES OBTAINED FROM OTHER LABORATORIES

RBS/ERDA method using 4.2 MeV $^{7}Li^{2+}$ has been applied to analyze aluminium oxinitride samples, obtained from N. Barradas, ITN, Portugal. The conventional RBS/ERDA method was able to deliver the contents of Al and contaminants H, Ar and Xe in the 100 nm thick layer. Measured RBS and ERDA spectra are shown in Fig. 5. The same method has been applied to measure hydrogen depth profiles in SiC thin films, obtained from I. Bogdanović Radović from IRB, Croatia.

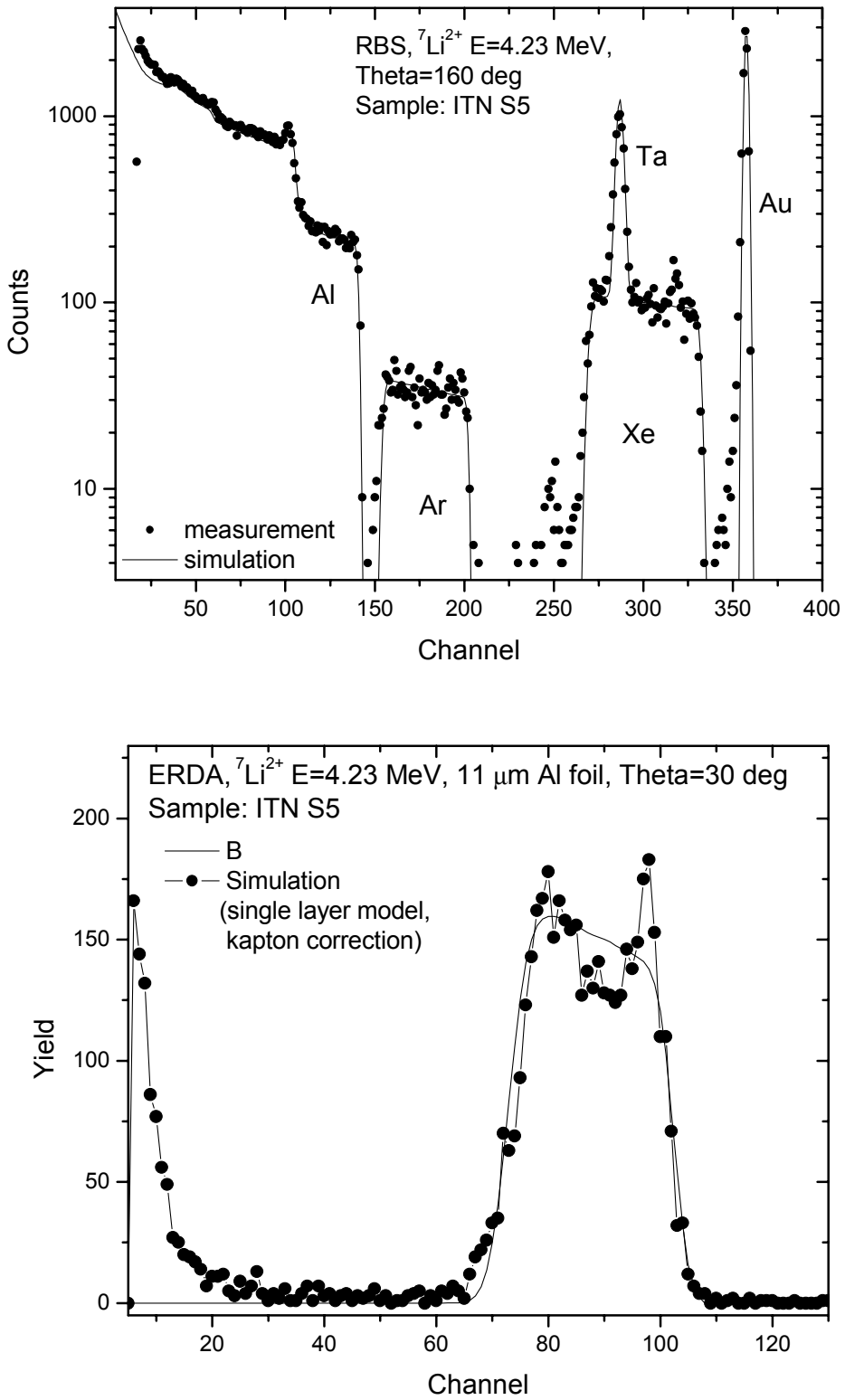

Figure 5. RBS and ERDA spectra measured on the 100 nm thick aluminum oxynitride sample, obtained from ITN, Portugal (sample labeled S5) within round-robin measurements on thin aluminum oxynitryde thin films.

6. Conclusions

A Time-of-Flight ERDA system and an in-beam charge collector have been successfully developed at the Institute 'Jožef Stefan'. They have been used to measure the thickness and stoichiometry of thin aluminium oxynitride films as part of an intercomparison exercise. RBS and Time-of-Flight ERD have been used in conjunction to characterize thin SiN films, and to determine the concentration of hydrogen incorporated during the manufacturing process. It was found that the hydrogen depth concentration profile was uniform in all samples and independent of the gas flow ratios used.

ACKNOWLEDGMENT

The stay of one of us (A.R.) in the Research Centre Rossendorf, Germany, supported by a Marie Curie fellowship is gratefully acknowledged.

REFERENCES

[1] WHITLOW, H.J., POSSNERT, G., PETERSSON, C.S., Quantitative mass and energy dispersive elastic recoil spectrometry: Resolution and efficiency considerations, Nucl. Instr. Meth. B27 (1987) 448.

[2] KEINONEN, J., TIKKANEN, J., KURONEN, A., AHLGREN, T., NORDLUND, K., Comparison of TOF-ERDA and nuclear resonance reaction techniques for range profile measurements of keV energy implants, Nucl. Instr. Meth B119 (1996) 533.

[3] BOHNE, W., RÖHLICH, J., RÖSCHERT, G., The Berlin time-of-flight ERDA setupe, Nucl. Instr. Meth. B136 (1998) 633.

[4] GRIGULL, S., KREISSIG, U., HUBER, H., ASSMANN, W., Element-dependent ERDA probing depths using different detection systems, Nucl. Instr. Meth. B132 (1997) 709.

[5] BUSH, F., PFEFFER, W., KOHLMEYER, B., SCHÜLL, D., PÜHLHIFFER, F., A position-sensitive transmission time detector, Nucl. Instr. Meth. 171 (1980) 71.

[6] RAZPET, A., PELICON, P., RUPNIK, Z., BUDNAR, M., Development of a time-of-flight telescope for ERDA at the Joef Stefan Institute, Nucl. Instr. Meth. B201 (2003) 535.

[7] KLANJŠEK GUNDE, M., MAČEK, M., The relationship between the macroscopic properties of PECVD silicon nitride and oxynitride layers and the characteristics of their networks, Appl. Phys A74 (2002) 181.

[8] MAYER, M., SIMNRA User's Guide, Technical Report IPP 9/113, Max-Planck-Institut Fuer Plasmaphysik, Garching, Germany, 1997.

[9] BAGLIN, J.E.E., KELLOCK, A.J., CROCKETT, M.A., SHIH, A.H., Absolute cross section for hydrogen forward scattering, Nucl. Instr. Meth. B64, (1992) 469.

[10] QUILLET, V., Report Group de Physique des Solides, Universite Paris VII, 1994.

[11] Rudolph, W., Bauer, C., Brankoff, K., Grambole, D., Grötzschel, R., Heiser, C., Herrmann, F., Plastic foils as primary hydrogen standards for nuclear reaction analysis, Nucl. Instr. Meth. B15 (1-6): (1986) 508.

ROUND ROBIN CHARACTERIZATION OF SILICON NITRIDE THIN FILMS PRODUCED BY PLASMA-ENHANCED CHEMICAL VAPOUR DEPOSITION

P. Pelicon
Institute Jožef Stefan, Ljubljana, Slovenia

Lu Xiuqin
China Institute of Atomic Energy, Beijing, China

E.I. Andrade
Universidad Autonoma de Mexico, Mexico

Abstract

A round robin exercise was conducted to assess the potential of three different analytical techniques for characterizing silicon nitride thin films: RBS/ERDA, ΔE(gas) - E(PSD) ERDA and Forward Elastic Scattering. No single technique was found superior in obtaining all information. A complete characterization requires information from complementary techniques.

1. SAMPLE PRODUCTION PARAMETERS

Films of amorphous hydrogenated silicon nitride were deposited on 4-inch diameter single-side polished silicon wafers (n-type, <100> crystal plane, dc resistivity 3–5 Ωcm, thickness 525 ± 25 μm) in a radial flow reactor. Other production parameters were:

- Reactant gasses: SiH_4 and NH_3.
- Carrier gas: Nitrogen.
- Operating reactor frequency 100 kHz.
- Chamber pressure: 210 mTorr.
- Substrate temperature during deposition: 300°C.

Deposition has been performed by varying the NH_3/SiH_4 gas flow ratio while keeping the net flow of both reactant gasses constant. The gas flow ratios are given in Table 1.

Table 1. Gas flow parameters

Sample Label:	**NH_3/SiH_4 flow ratio:**
A	1.75
B	2.35
C	2.91
D	3.45
E	3.92
F	5.21

2. ANALYTICAL METHODS AND DETAILS USED

Analytical methods and conditions used in the round robin test are given in the Table 2. The incident angle is given as the angle between primary beam and sample surface. The outgoing angle is the angle between sample surface and direction of detection. The scattering angle is the angle between primary beam and the direction of detection.

Table 2. Experimental methods, beam parameters, geometries and accelerators used

	Method	Beam used	Energy [MeV]	Remarks
1	Forward Elastic Scattering	$^{12}C^{3+}$	10 MeV	Scattering angle 45º Ion current 3.3 particle nA Measured at 6 MV EN Tandem
2	ΔE(gas) - E(PSD) ERDA Q3D magnetic spectrometer system (for H surface conc.)	^{127}I	140 MeV	Incident angle 15º Outgoing angle 15º Scattering angle 30º Ion current ≈ 1 particle nA Solid angle 1.95 mSr Measured at HI-13 Tandem
3	RBS/ERDA	He+, $^{7}Li^{2+}$	3.2 MeV, 4.2 MeV	Incident angle 15º Outgoing angle 15º Scattering angle 30º ERDA detector: 11 μm (^{7}Li) Al foil Ion current: ≈. 2 particle nA Beam profile 1mm (X) × 4mm (Y) Measured at 2 MV Tandetron

3. RESULTS

The results are reported in Table 3. All three methods produced similar results for thickness and stoichiometry for the films (A — F). Method 2 was also able to determine surface contaminants on the samples.

Table 3. Thin film parameters.

Sample label	Method	Film stoichiometry $Si_x:N_y:H_z$ x+y+z=1			Total concentration				Remarks
					Constituents [10^{18} at/cm^2]		Contaminants [10^{15} at/cm^2]		
		Si	N	H	N	H	O	C	
A	1	0.31 (3)	0.42 (4)	0.27 (2)	2.85 (26)	1.83 (16)			
	2	0.38 (3)	0.40 (2)	0.22 (2)	2.59 (29)	1.37 (15)	9	9	O and C on surface
	3	0.42 (2)	0.36 (2)	0.22 (2)	2.28 (22)	1.33 (13)			
B	1	0.33 (3)	0.41 (4)	0.26 (2)	3.24 (29)	2.05 (18)			
	2	0.40 (3)	0.40 (2)	0.20 (2)	2.86 (32)	1.28 (14)	24	24	O and C on surface
	3	0.39 (2)	0.38 (2)	0.22 (2)	2.65 (26)	1.44 (14)			
C	1	0.29 (2)	0.43 (4)	0.28 (2)	2.83 (25)	1.84 (17)			
	2	0.38 (3)	0.40 (2)	0.22 (2)	2.59 (29)	1.37 (15)	12	16	O and C on surface
	3	0.38 (2)	0.40 (2)	0.22 (2)	2.51 (25)	1.32 (13)			
D	1	0.28 (2)	0.40 (4)	0.32 (3)	2.28 (21)	1.82 (16)			
	2	0.35 (3)	0.41 (2)	0.24 (2)	2.37 (26)	1.24 (14)	8	20	O and C on surface
	3	0.36 (2)	0.42 (2)	0.21 (2)	2.28 (23)	1.09 (11)			
E	1	0.27 (2)	0.41 (4)	0.32 (3)	2.39 (21)	1.86 (17)			
	2	0.35 (3)	0.42 (2)	0.23 (2)	2.33 (26)	1.19 (13)	8	16	O and C on surface
	3	0.36 (2)	0.41 (2)	0.22 (2)	2.079 (21)	1.04 (10)			
F	1	0.30 (3)	0.39 (3)	0.31 (3)	4.29 (38)	3.41 (31)			
	2	0.35 (3)	0.43 (2)	0.22 (2)	4.70 (70)	>1.41	8	16	O and C on surface Range too low
	3	0.35 (2)	0.43 (2)	0.22 (2)	>2.7	>1.70			Range too low

Note: Stoichiometry parameters x:y:z of the $Si_x:N_y:H_z$ film is taken from the homogeneous region of the film, away from the interface and surface Total thickness of a particular element is given in number of atoms/cm^2, which includes both the interface and surface region. Errors are given in parenthesis and mean error at the last digit.

4. CONCLUSIONS

While all three methods produced similar results, the differences in the applicability of the analytical techniques are different. Method 1 was able to measure the contributions from all the elements simultaneously. However a single experimental spectrum is obtained that is a convolution of the spectra of all the individual elements. A deconvolution technique must be used to obtain the stoichiometry, which may produce unreliable results in certain situations.

Method 2 gives element-separated spectra enabling a relatively easy determination of the film stoichiometry. The added advantage is the complete detection of all light elements in the target, from hydrogen up to silicon, enabling contaminants to be readily identified. The disadvantage of Method 2 is that the heavy ion beam modifies the target during the experiment, which affects the light element composition, especially hydrogen.

Method 3 uses two detectors; one to determine the Si:N ratio, the other to determine the hydrogen content. The H, N and Si stoichiometry is obtained by combining the data from both detectors. The disadvantage of this method is that if oxygen is also present in the sample, it cannot be adequately resolved from the nitrogen. Therefore, Method 3 would be unsuitable for a complete elemental analysis of silicon oxynitride films.

A complete characterization requires information from complementary techniques, taking into account the possible stoichiometry of the sample and the information required.

ION BEAM ANALYSIS OF LIGHT ELEMENTS IN THIN FILMS, MATERIALS FOR COATINGS AND SOLAR CELLS

I. Bogdanović Radović, Z. Medunić, N Skukan, Ž. Pastuović, M. Jakšić
Ruđer Bošković Institute, Department of Experimental Physics, Croatia

Abstract

The work undertaken within the project can be divided into three activities. Firstly, work done to improve experimental capabilities at the Zagreb nuclear microprobe beam line for light element analysis that includes setup of new ERDA system is described. Secondly, work done to extend cross sections database needed for light element analysis is presented. Thirdly, different applications of RBS, ERDA and NRA techniques for analysis of light elements in thin films, materials for coatings and solar cells, are discussed.

1. EXPERIMENTAL SETUP

For ERDA analysis, the system for particle identification based on IEE (ion induced electron emission) was mounted on the nuclear microprobe chamber. O. Benka and co-workers at the University of Linz, Austria originally developed the system for broad-beam ERDA. A novel feature of our system is that it is mounted at the nuclear microprobe. IEE ERDA comprises of two detectors, a particle detector for the energy determination of recoiled and scattered particles and a microchannel plate system for particle identification. A new stainless steel spherical chamber installed at the microprobe line is equipped with two microscopes, seven detector ports in backward direction, a xyz manipulator, and sample holder with heating/cooling possibility. In order to maintain the high vacuum in the chamber during the sample exchange, a load-lock system was designed. By rotating the ERDA system main flange through 180 degrees, an analysis at two different recoil angles 30° and 45° can be done. Fine positioning of the sample tilt in respect to the beam direction still needs to be improved by constructing an appropriate rotational stage for the sample holder. Easy and reliable adjustment of this angle is essential for ERDA in order to provide the highest possible depth resolution and sensitivity.

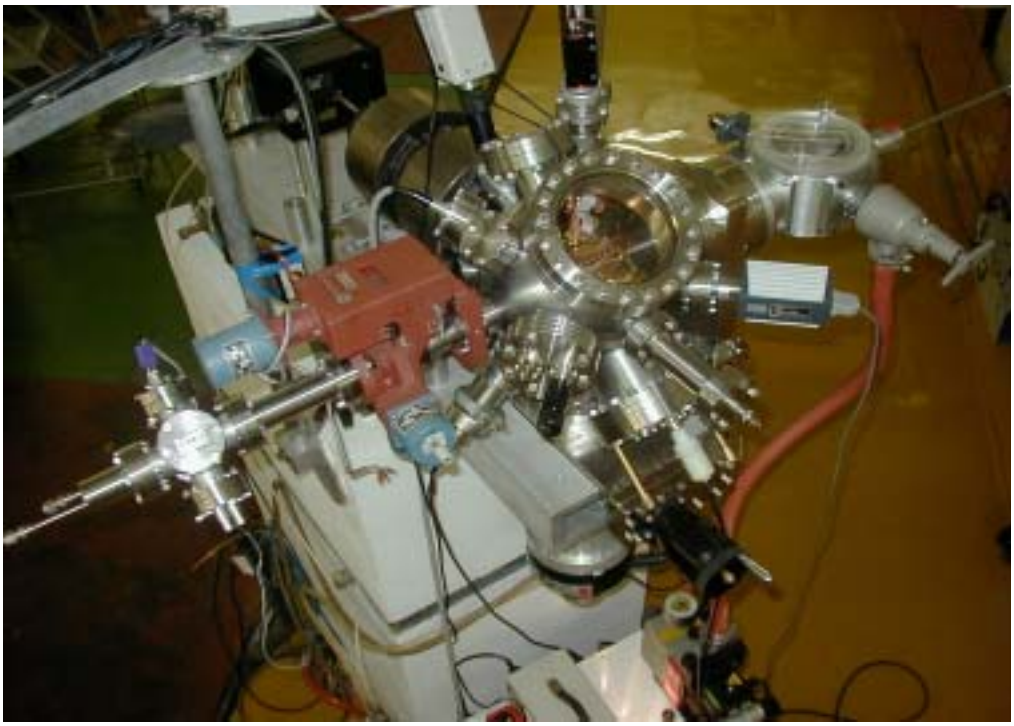

Figure 1. The new scattering chamber of the proton microprobe includes a load-lock system, a xyz translator, two microscopes, seven detector ports, and an IEE ERDA system.

2. CROSS SECTION DATABASE

2.1. H recoil cross-sections for He ions

Proton differential recoil cross-sections were measured for the impact of He ions in the energy range from 2.5 to 4.5 MeV and for recoil angles from 30º to 60º. For the first time, H recoil cross-sections at angles from 45º to 60º are reported.

Thin melamine foils (~ 50 μg/cm^2) evaporated on ~ 50 μg/cm^2 thick Cu where prepared as targets. Two surface barrier detectors positioned at forward angles were used to detect recoiled and scattered atoms. One detector was kept all the time at 40º and was used to measure loss of H due to irradiation. The other detector could be moved without breaking the vacuum to measure at scattering angles between 0° and 160°.

All measured cross sections, except that for 60°, deviate from Rutherford cross-sections. The angular dependence of the H recoil cross-sections at energies from 2.5 to 4.5 MeV is shown in Figs. 2(a)-(e). The experimental results were compared with the other available experimental data for lower recoil angles and good agreement was found. A comparison was also made with theoretical calculations obtained by fitting the phase shifts of the kinematic inverse reaction using the principle of detailed balance. Again agreement was found for low recoil angles, but for 55° and 60° the experimental cross sections were significantly smaller than the theoretical values.

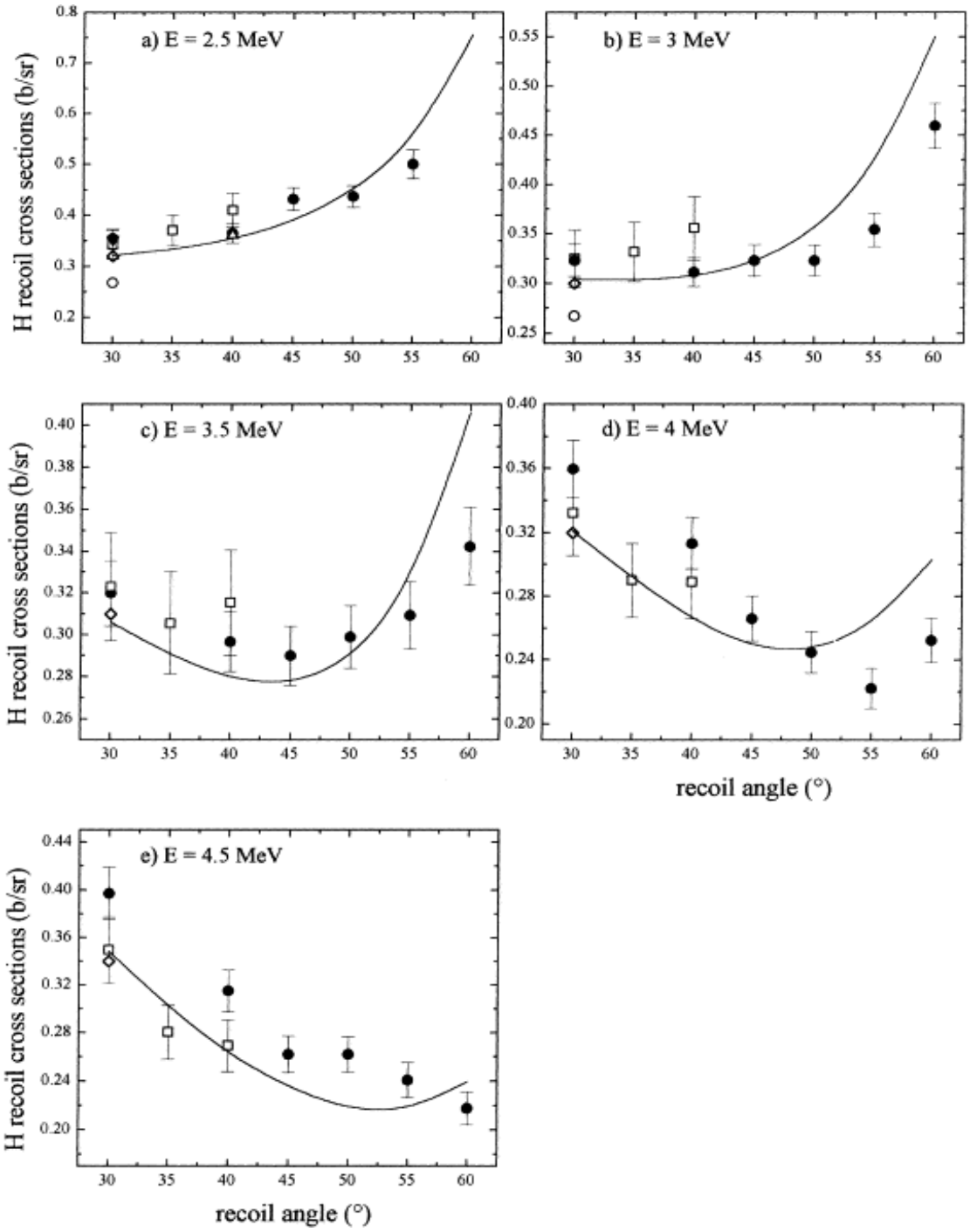

Figure 2. Angular dependence of the H recoil cross-sections (b/sr) for (a) 2.5 MeV; (b) 3 MeV; (c) 3.5 MeV; (d) 4 MeV; (e) 4.5 MeV He incidence. ● present measurements, □ [1], △ [2], ○ [3], ▼ [4], ◇ [5] and — [6].

2.2. Helium elastic scattering from carbon

The differential cross-sections for elastic scattering of ^{4}He ions by carbon atoms were measured at scattering angles of 30°, 45°, 60°, 135° and 150° in the energy range from 2 to 4.8 MeV. The possibility to use forward scattered projectiles in our ERDA setup for the

normalization purposes, motivated us to measure cross sections at forward angles. Up to now mostly data for angles larger than 150° were published in the literature.

Instead of using thin carbon target and point-by-point measurements we decided to extract the cross-sections from a thick target yield. Using this method, only a few discrete measurements have to be done to obtain the whole excitation curve. A thick carbon target with a thin evaporated Cu layer on the surface was used for the measurement. The number of impinging projectiles was obtained from the He ions scattered by the Cu layer assuming Rutherford cross-sections.

The carbon scattering cross-sections were then obtained from a comparison of measured He energy spectra with simulated ones using the ion beam analysis software SIMNRA. The comparison between measured spectra and spectra calculated using Rutherford cross-section is shown in Fig. 3.

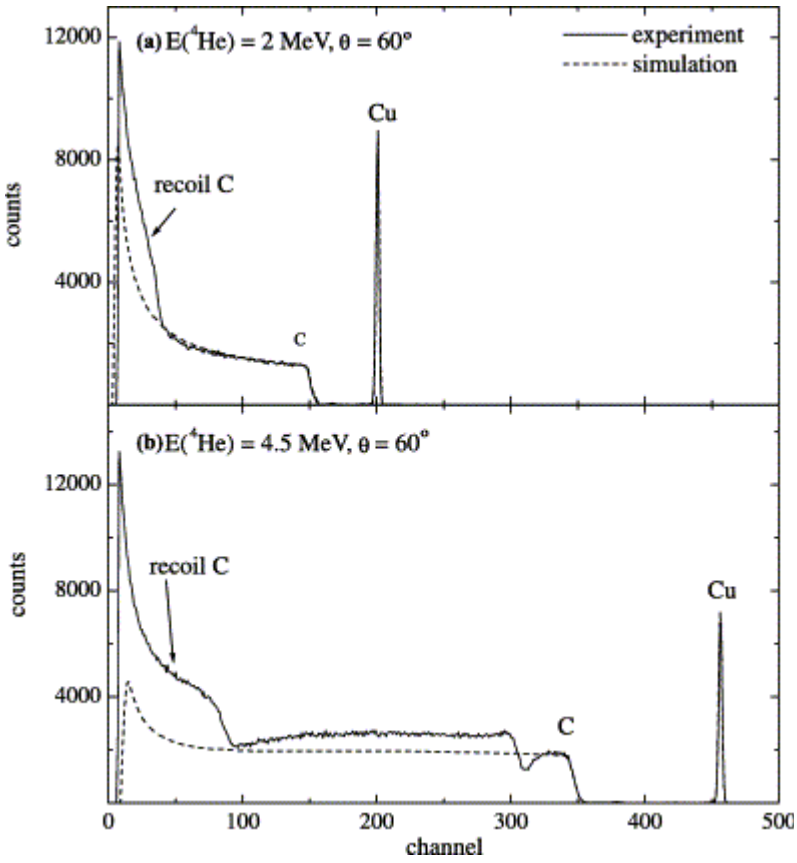

Figure 3. Comparison between measured (—) and calculated (- - -) spectra at 60° for two different 4He energies: (a) 2 MeV and (b) 4.5 MeV.

Above 2 MeV, all evaluated cross-sections become non-Rutherford. Deviations from Rutherford cross-sections are about 50% for 30° scattering angle and amount up to a factor 30 for 150° scattering angle. The measured experimental cross-sections were compared with the calculated theoretical cross-sections which are described in detail in [1] and already published data [2]. Satisfactory agreement was obtained for all measured scattering angles and energies.

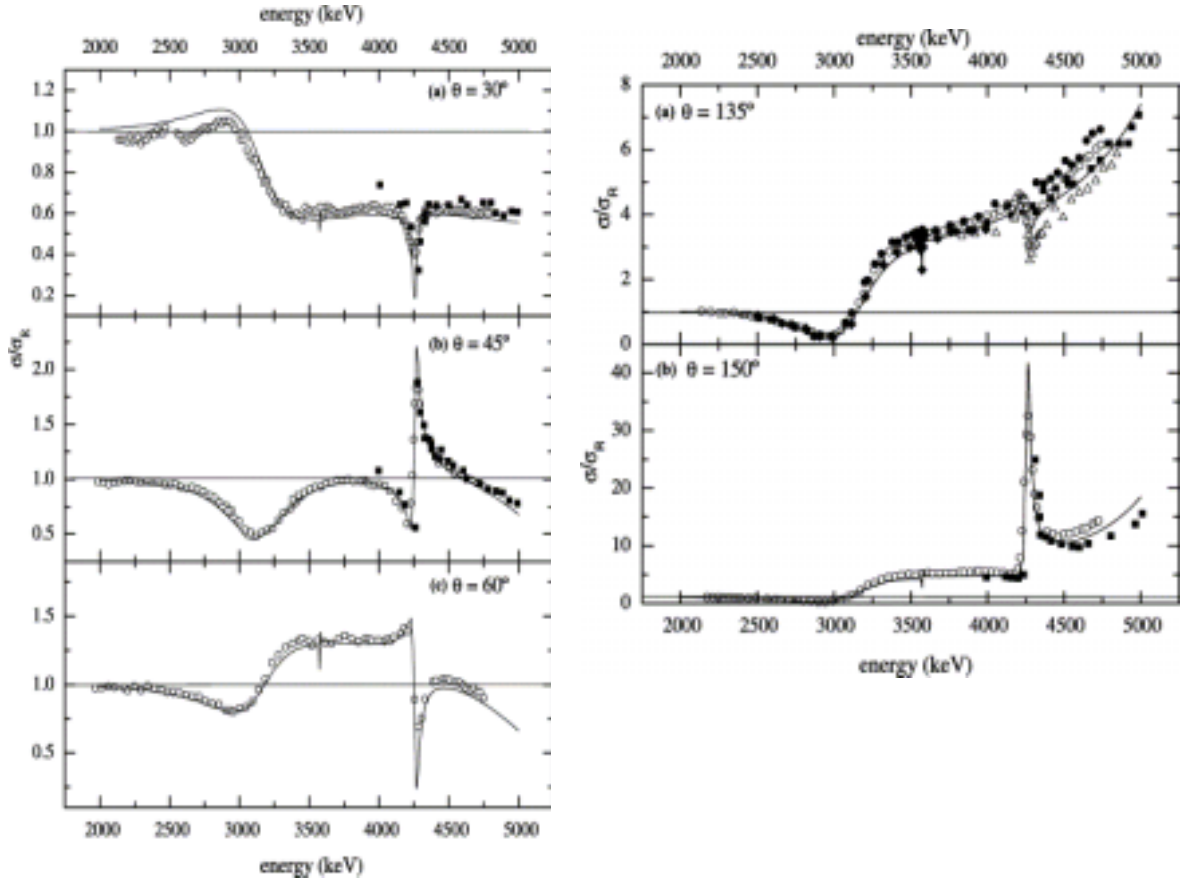

Figure 4. Ratios of ^{4}He–C cross-sections to Rutherford cross-sections for different scattering angles. (o) are present measurements, —- theory, - [8], ● - [9], Δ - [10], ♦ -[11].

3. APPLICATIONS OF RBS, ERDA AND NRA TECHNIQUES FOR ANALYSIS OF LIGHT ELEMENTS IN THIN FILMS, MATERIALS FOR COATINGS AND SOLAR CELLS

3.1. Characterization of amorphous silicon solar cells by IBA methods

Amorphous silicon solar cells were produced in a single junction structure, deposited on a glass substrate. As a first contact, a transparent and conductive tin oxide layer (SnO_2) was deposited by atmospheric pressure chemical vapour deposition (CVD). The active layer consists of an amorphous silicon p–i–n structure deposited by plasma enhanced CVD. The back contact, a thin aluminum film, was made by evaporation in high vacuum.

IBA measurements were performed in a RBS/ERDA scattering chamber using Li and C beams. The composition of the solar cells was studied by RBS analysis using a collimated (3 mm) 5.1 MeV Li^{2+} ion beam. The incident angle was $\alpha = 0°$. A silicon particle detector with a 3 mm collimator was positioned 67 mm away (solid angle 1.57 msr) from the sample at $\theta = 170°$. A typical spectrum obtained for a solar cell exhibiting high electrical conversion efficiency together with the SIMNRA simulation is shown on Fig. 5.

The hydrogen concentration was determined by simultaneous collection of RBS and ERDA spectra using a 9 MeV C^{3+} ion beam. Data from the RBS spectra served only for ERDA charge evaluation. The incident angle was $\alpha = 67.5°$, while the RBS scattering angle was $\theta =$

150°. The ERDA solid angle was 0.617 msr with a recoil angle θ = 45°. An aluminum foil of 6 μm was placed in front of the ERDA detector in order to stop the forward scattered ions. A typical ERDA spectrum together with a simulation is plotted in Fig.6. Two hydrogen peaks are clearly distinguishable: a surface contaminant peak and the peak originating from the a-Si:H layer. The hydrogen content for both high and low efficiency solar cells was determined from the ERDA data, using the theoretical Rutherford cross-sections in SIMNRA. The reliability of using the theoretical cross-sections for hydrogen was tested using a TiH_2 sample. The energy straggling was taken into account in all simulations.

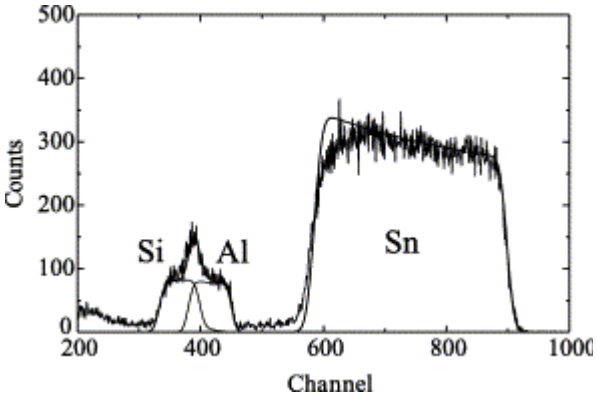

Figure 5. RBS spectrum of a high efficiency solar cell (5.4%) obtained by using a 5.1 MeV Li^{2+} ion beam.

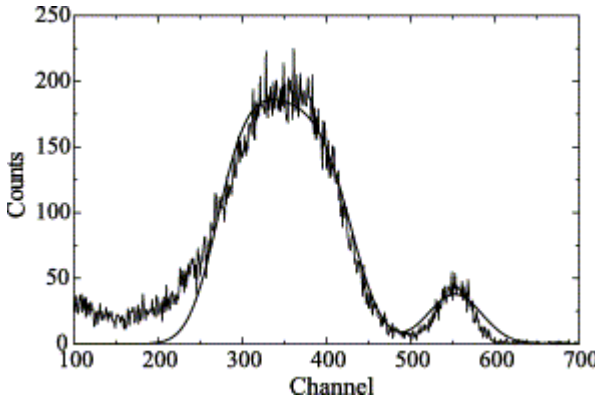

Figure 6. Two hydrogen peaks in ERDA spectrum obtained with C^{3+} ion beam: surface contaminant peak and the peak originating from a-Si layer. The smooth line represents the simulated spectrum.

The quantitative results for the low and high efficiency solar cells obtained from the simulation of 5.1 MeV Li^{2+} ion beam RBS are given in Table 1. A thin organic contaminant was assumed to be present on the sample surface. For the high efficiency solar cells, the a-Si;H and SnO_2 layers are about 10% thinner than the low efficiency solar cells. This indicates that for high efficiency solar cells, the a-Si:H layer thickness is close to optimal for a single junction cell. For the low efficiency cells however, the ratio between the thicknesses of the a-Si:H layer and the collection length seems to be too high.

Table 1. The layers thickness of a-Si: H solar cell determined from RBS spectra for two types of solar cells (assumed densities: 2.7 g/cm^3 for Al, 2.3 g/cm^3 for a-Si and 6.95 g/cm^3 for SnO_2)

Layer	*d* (nm)	
	5.4% efficiency	3.2% efficiency
Al	370	280
a-Si	350	380
SnO_2	1980	2380
SiO_2	Substrate	Substrate

3.2. Characterization of amorphous hydrogenated SiC films by IBA methods

Contrary to crystalline SiC samples, where composition would be well defined, thin films of hydrogenated amorphous SiC films (a-$Si_{1-x}C_x$:H) exhibit different degrees of structural ordering so their stoichiometry can be variable. This has to be determined by suitable techniques. In addition to the determination of different bonds in samples by IR spectroscopy (for hetero-polar bonds) and Raman spectroscopy (homo-polar bonds), ion beam scattering techniques (ERDA and RBS) can be used for a determination of the total Si, C and H concentrations and their depth profiles. RBS and ERDA measurements were done with ^{4}He ions using the 1.6 MV tandem accelerator at the Johannes Kepler University in Linz, Austria, and ^{12}C ions using the EN Tandem accelerator at the Ruđer Bošković Institute in Zagreb, Croatia.

In Fig. 7, RBS and ERDA spectra obtained by using 4 and 2.5 MeV ^{4}He ions, on inhomogeneous, 0.6 μm thick a-$Si_{1-x}C_x$: H layer are shown. The layer is deposited as 'double' with about 20% difference in C concentration in order to check the possibility of depth analysis. This difference in concentration should produce well-distinguished steps in the spectrum, which is clearly visible in the shape of the signal for C and Si atoms.

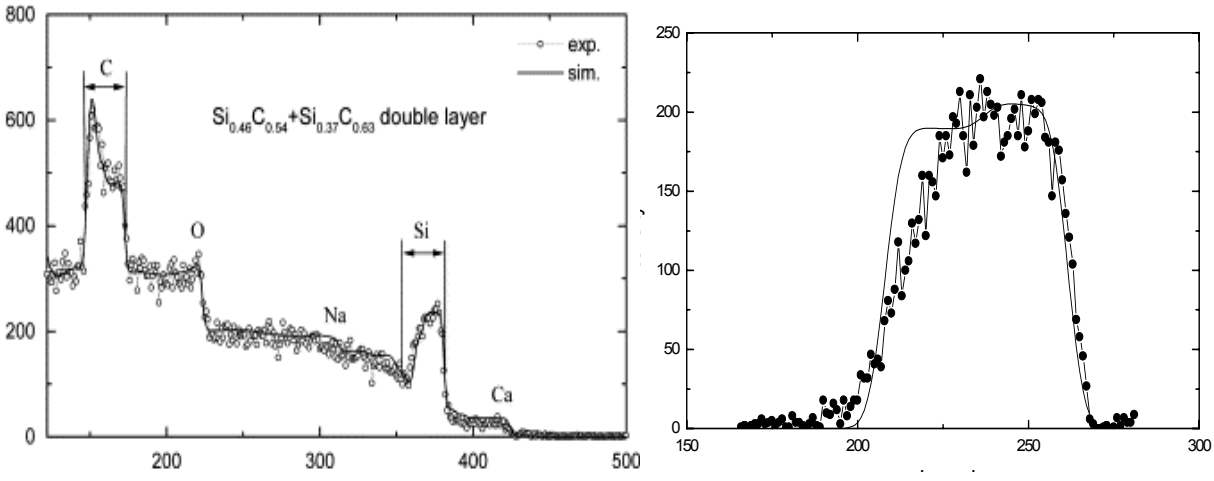

Figure 7. The simulated (full line) and experimental (open circles) RBS spectrum of 4 MeV ^{4}He ions on a inhomogeneous 0.6 μm a-$Si_{1-x}C_x$:H 'double layer', thin film consisting of two, 0.3 μm thick parts, with different carbon to silicon ratio (left graph). The corresponding H depth profile obtained by 2.5 MeV He ions is shown (right graph).

In Fig. 8, the C concentration estimated by IR spectroscopy (C in Si-C and C-H bonds) is plotted versus the C concentration obtained by RBS. The unit slope is plotted as a guide for the eye. Up to 1×10^{18} atoms/cm^2, the whole carbon is detected by IR; this means that the whole carbon is in hetero-polar bonds. Above 1×10^{18} atoms/cm^2, there is an off-set between IR and RBS concentrations, which coincides with the appearance of C–C related features in Raman spectra, corresponding mostly to amorphous and micro-crystalline graphite. Moreover, the difference between the carbon concentration in hetero-polar bonds and the total amount of carbon in the layer is proportional to the surface under the C–C related peaks in Raman spectra.

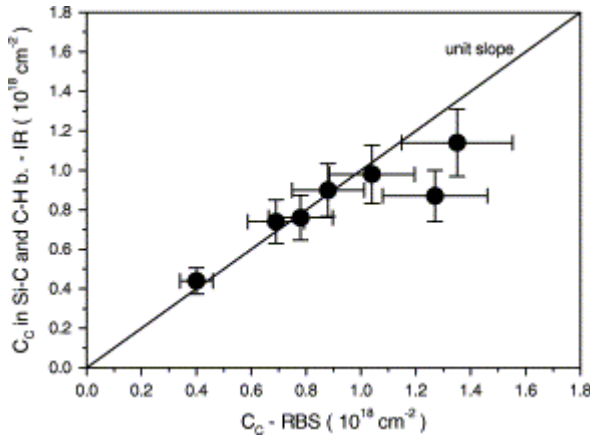

Figure 8. Comparison of the carbon concentrations estimated by FTIR and RBS.

Fig. 9 shows an example where a broad beam was used to record a spectrum of forward scattered and recoil particles. 9 MeV ^{12}C ions were used with the particle detector positioned at a 45° angle. Suitable detection limits for all significant elements in a-$Si_{1-x}C_x$:H can be obtained. A typical experimental spectrum, accompanied by a SIMNRA simulation indicating H and C contribution, in a 0.3 μm thick sample, is presented in Fig. 9.

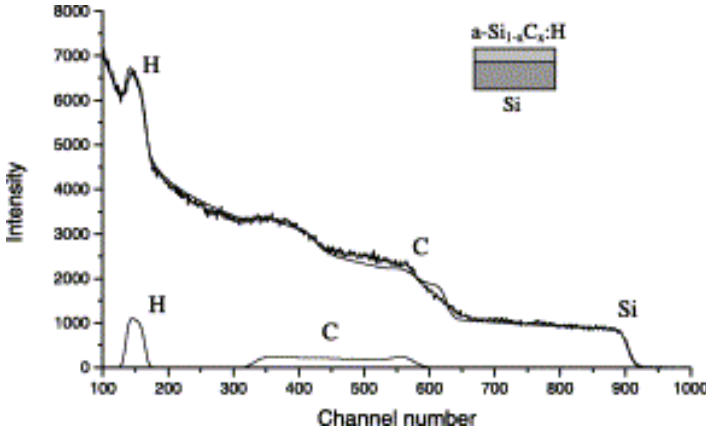

Figure 9. Experimental and simulated spectrum of forward scattered 9 MeV C ions from a thin a-$Si_{1-x}C_x$:H layer of $2.7\cdot10^{18}$ at/cm^2 thickness on a mono-crystalline Si substrate. Contributions of H and C to the simulated spectrum are indicated at the bottom. Estimated composition is $Si_{0.4}C_{0.4}H_{0.2}$.

3.3. PIXE and NRA analysis of light elements in multilayer films designed for optical applications

In the field of doped-silica thin film deposition for optical applications, a quantitative analysis of the composition is needed in order to correlate the chemical and physical properties of the material to dopant concentration. Particularly, the composition is connected to photosensitivity, which is a property exhibited by some materials that change their refractive index upon irradiation with UV light of suitable frequency. Materials like BPSG and BGSG (Boron-Phosphorus and Boron-Germanium Silica Glass) are strongly photosensitive and allow the achievement of index matching with silica. The amount of boron influences both the original refractive index (depressing it) and the photosensitivity (enhancing it). Due to the thermal treatment that sometimes occurs in the deposition process, boron could even migrate causing gradients in film properties. The typical thickness of such layers is several micrometers.

Lateral measurements of the sample surface were performed by focused 0.9 MeV protons. Beam spot size in the horizontal dimension was 2.0 μm. Two detectors were used simultaneously: silicon X-ray detector for characteristic X-rays (PIXE spectroscopy) and a PIPS particle detector for the detection of backscattered particles (RBS spectroscopy) and nuclear reactions products (NRA spectroscopy).

In the use of nuclear microprobe nuclear reaction analysis, only a limited number of reactions are suitable for the analysis due to the limitations in beam current and current density. For boron analysis we found the $^{11}B(p,\alpha)^{8}Be$ reaction the most appropriate. The experimental determination of reaction yield showed, as expected from the literature, the highest efficiency for the 850 keV. PIXE analysis using 900 keV provides excellent sensitivity for the Si-K and Ge-L line as well. Samples with two or three silica layers that have been deposited on silicon wafers have been prepared with different contents of B_2O_3 and/or GeO_2. The layer thicknesses ranged from 3 to 10 μm. The beam spot size in the horizontal plane for the 0.9 MeV proton beam was 1.5 μm. After performing linear scans over the lateral surface of the sample, the beam was positioned in the middle of each layer under study, where quantitative analysis was performed. The boron content was determined by calibration with several glass standards.

During the scanning of the proton microbeam over the sample lateral cross section, and collecting the counts of elemental 'lines' in corresponding files, 'qualitative' images of elemental distributions were obtained and shown in fig. 10. The full horizontal scale (0.00 to 0.10) represents about 90 μm. By projection of all events onto the x-axis, semi-quantitative elemental distributions in layers are obtained. By positioning the beam to the middle of each layer (points A, B, C on Fig. 10); spectra for a quantitative analysis were obtained.

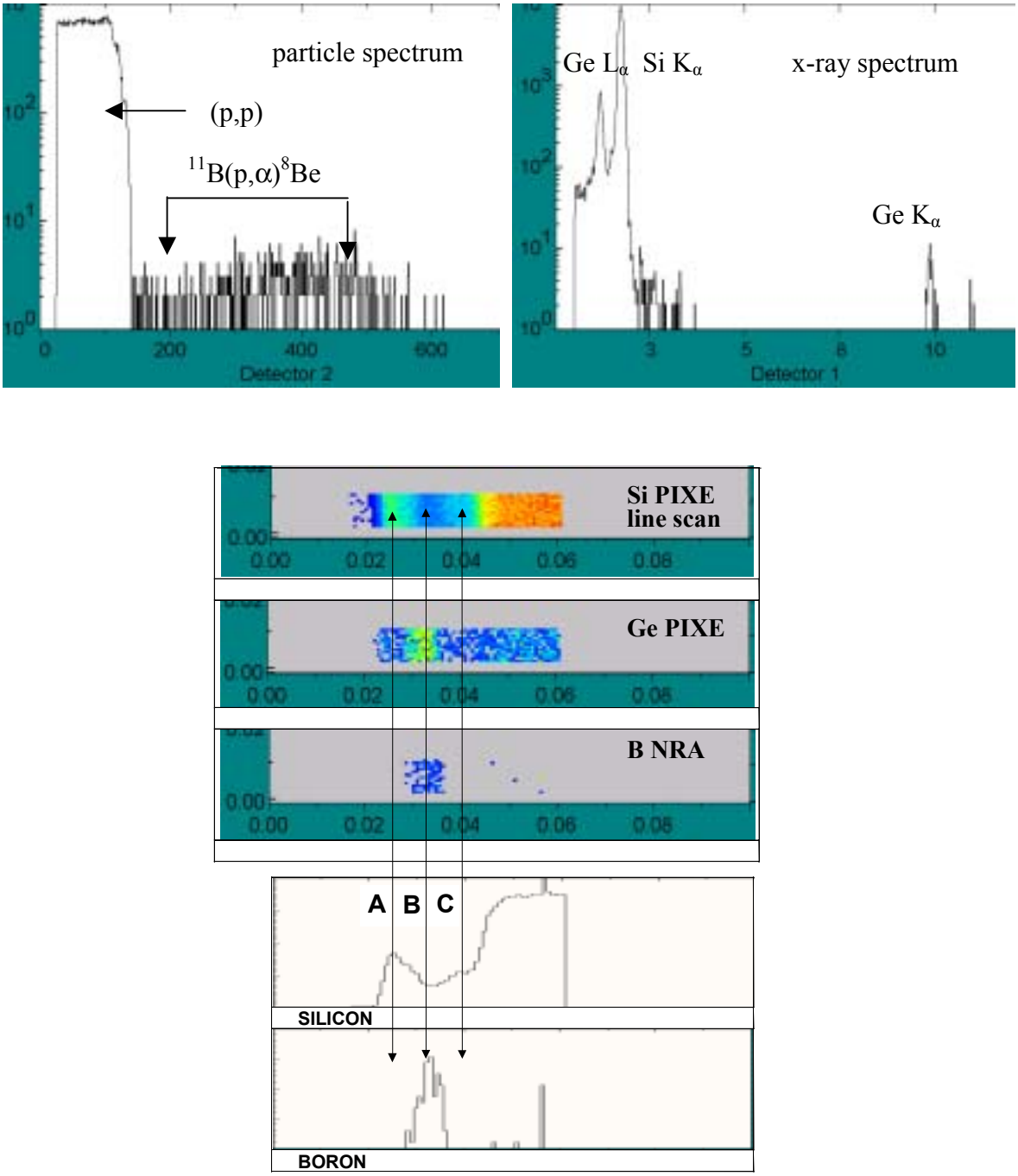

Figure 10. Typical particle and x-ray spectra are shown on the top. Below, line scans together with projections on x-axis are displayed.

3.4. Analysis of oxygen amount in WO_x thin films using RBS and NRA

Thin WO_x films were prepared by magnetron sputtering of W ions in an Ar atmosphere. Oxygen was unintentionally introduced as an impurity to the system through the vacuum system. Due to different pressure of the working gas in the chamber during the preparation, W atoms were deposited on the Si surface with different energies. High energy (low gas pressure) W atoms crystallize in a stable α phase while low energy (high gas pressure) W ions crystallize in an unstable β phase. It is believed that the stability of the β phase is influenced

by O present as a interstitial defect in the film. The β phase exhibits one order of magnitude better wear resistance compared to the α phase, but has at the same time a poorer electrical conductivity. Therefore, for practical applications of WO_x films in electronics, it is interesting to find experimental conditions (gas pressure), where films with best characteristics concerning electrical conductivity and wear resistance are deposited.

Two types of ions were used for the measurements: 2.9 MeV H for RBS at 165º and 0.85 MeV ^{2}H for NRA using the $^{16}O(d,p)^{17}O$ reaction. To stop ^{2}H ions scattered from the target, a 12 μm thick Mylar™ foil was put in front of the solid state detector. From Fig. 11, it can be seen that RBS using a 2.9 MeV H beam is not adequate enough to measure low amounts of O due to the high Si signal. This is in spite of the fact that the Si elastic scattering cross section has a minimum around 2.9 MeV, and the cross-section for O is smooth and about 10 times higher than Rutherford. Therefore, O concentrations were determined using the $^{16}O(d,p)^{17}O$ reaction. Unknown concentrations of O were determined using a ^{16}O thin film reference for NRA prepared for this CRP. A correlation between gas pressure in the chamber and oxygen concentration in the film was established.

a) RBS spectrum, E_p = 2.9 MeV

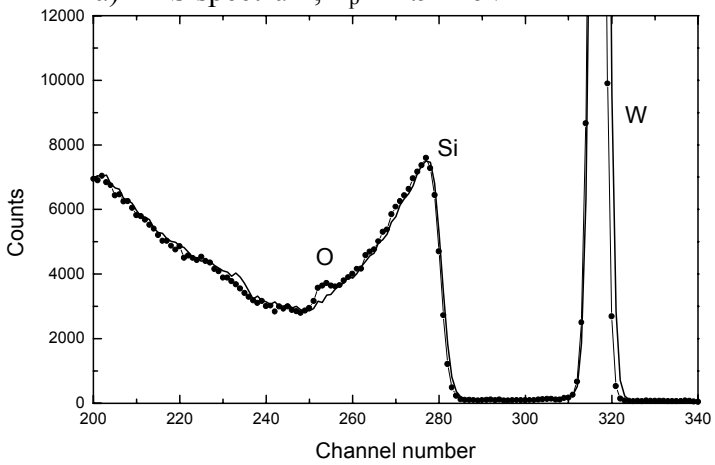

b) NRA spectrum, E_d = 0.85 MeV

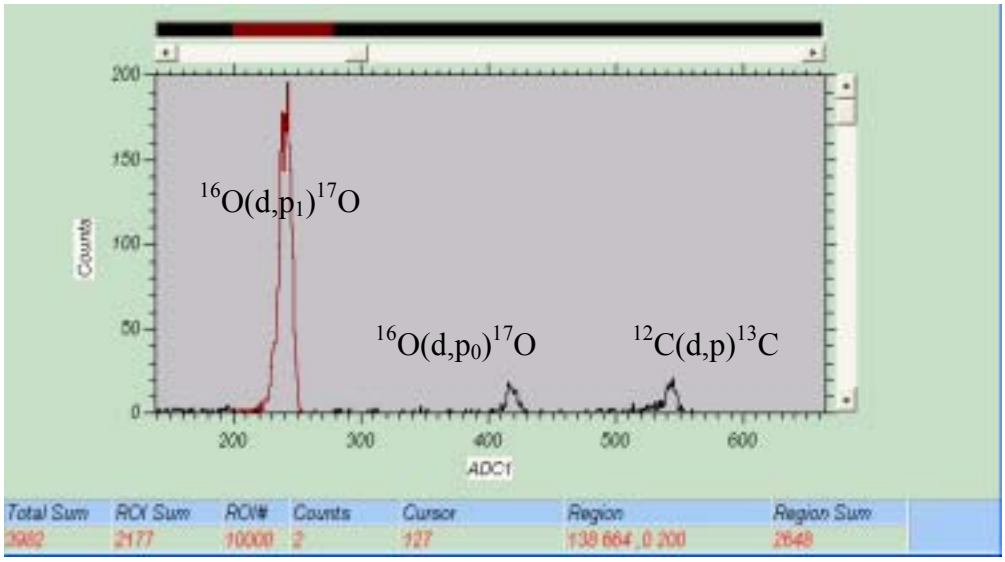

Figure 11. (a) Typical RBS spectrum of WOx sample measured by 2.9 MeV protons and (b) NRA spectrum measured with 0.85 MeV deuterium.

3.5. Hydrogen analysis in thin films by IEE ERDA

With the current capabilities of our switching magnet power supply it was not possible to bend O^{3+} ions with energy higher than 4.5 MeV into the microprobe scattering chamber. With this ion energy and with experimental geometry of ($\alpha = 15°$, $\beta = 15°$, $\theta = 30°$), up to 500 nm thick Si layers can be analysed. To test the depth resolution and sensitivity of our ERDA system, we have prepared samples by implanting 6.3×10^{16} at/cm^2 H ions into a Si wafer. In order to achieve a small implantation depth, 25.2 keV H^+ ions were used for implantation. The projected range and the implanted profile were calculated using the Monte Carlo simulation code SRIM2003. The yield in each channel in the experimental spectrum was related to the detected energy of the recoiled H ions through an energy calibration. Detected energies were then correlated with the corresponding depths by taking into account ion energy loss on the way in, the kinematic factor, and H recoil energy loss in the way out from the sample. Experimentally obtained depth profiles were then compared with SRIM profiles. According to the simulation, the maximum concentration of implanted H is expected at a depth of ~ 280 nm. Since the surface peak is very narrow, it was used to estimate depth resolution close to the surface. The calculated FWHM was 20 nm. Fig. 12(a) shows a two dimensional map, where recoiled H atoms are well separated from O ions scattered by Si. Generally, spectra of the forward scattered projectiles were used to calculate the total number of impinging projectiles, as well as to monitor H stability during the irradiation.

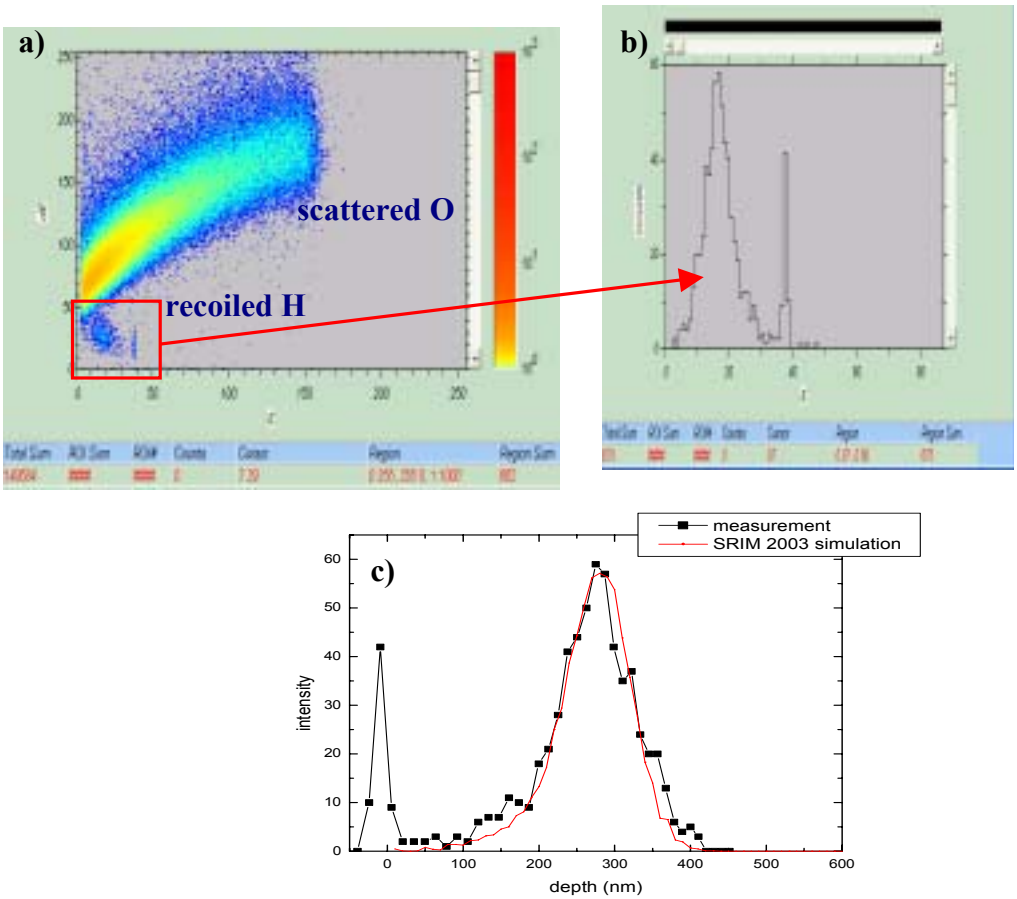

Figure 12. (a) IEE ERDA two dimensional map where forward scattered O ions are well separated from H recoils, (b) part of spectrum belonging to H recoils projected on x-axis, (c) comparison between experimentally obtained depth profile and profile calculated by SRIM2003.

The same experimental setup was used to analyse three different samples of amorphous Si on Si [100]. A typical two dimensional map of forward scattered O ions and H recoils is shown in Fig. 13. As both ion types are collected into the same solid state detector, the product NΩ (number of incident particles·× solid angle of detector) in SIMNRA was determined from normalization to the forward scattered spectrum. The amount of H, as well as the thickness of the amorphous Si layer, were found by comparing experimental data with SIMNRA simulations. Knowledge of hydrogen depth profiles in amorphous silicon thin films in the thickness range up to 500 nm is important in the development of higher efficiency a-Si:H films. The proceses of hydrogen diffusion between different p-i-n layers and contact layers of solar cells are planned to be studied by the IEE system.

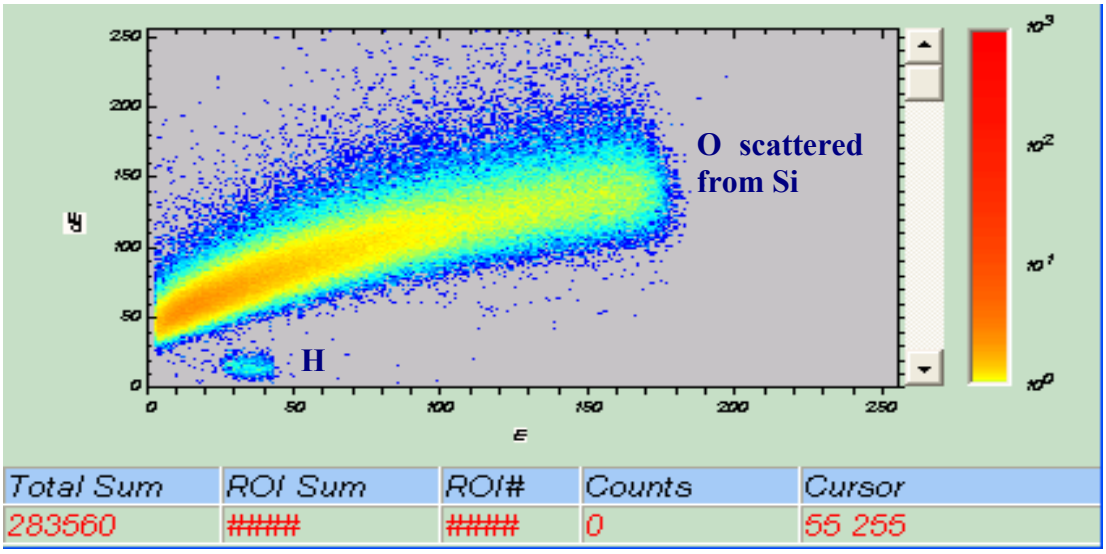

Figure 13. Two dimensional map displaying the well separated recoil H from the spectrum of O ions scattered from Si.

The final results for the thickness and stoichiometry of the three different amorphous Si films on Si [100] is shown in Table 2.

Table 2. Measured thickness and stoichiometry of a-Si:H solar cells

Sample Number	Thickness (10^{15} at/cm^2)	H (at. %)	Si (at. %)
1	1250	0.18	0.82
2	1616	0.16	0.84
3	1359	0.13	0.87

4. CONCLUSIONS

To improve capabilities for light element analysis, a new scatering chamber was installed at the proton microprobe beamline at the Ruđer Bošković Institute in Zagreb. For 3D profiling of H, ion induced electron emission ERDA can be done at two scattering angles, 30° and 45°.

H recoil cross sections for He ions were measured for recoil angles from 30° to 60°. Deviations from Rutherford values were found at all investigated energies and for all angles except 60°. ^{4}He-C scattering cross-sections were measured at five different scattering angles

in the energy span from 2.5 to 4.8 MeV. The results are in satisfactory agreement with the theoretical calculations and already published experimental data [2].

For characterization of amorphous silicon solar cells, RBS with a 5.1 MeV Li beam was sufficient to distinguish Al and Si layers few hundred nm thick. To enhance the depth resolution, C ions were used for depth profiling of H.

Thicknesses and amounts of all elements in the amorphous SiC films can be obtained with a 4 MeV He beam. The C signal in the RBS spectrum can be well distinguished from Si and other elements coming from the substrate due to the fact that cross-sections for He scattering from C are somewhat higher than Rutherford cross-sections. Results obtained with RBS are in good agreement with results obtained by IR spectroscopy.

Oxygen in thin WO_x films and boron in multilayer films designed for optical applications were determined using the $^{16}O(d,p)^{17}O$ and $^{11}B(p,\alpha)^{8}Be$ reactions respectively. The RBS method with 2.9 MeV protons was not adequate enough to measure low amounts of O, due to the high Si signal.

IEE ERDA with 4.5 O ions can be used to obtain depth distribution and amounts of H in thin films. The depth resolution was estimated to be about 20 nm near to the sample surface.

REFERENCES

[1] GURBICH, A.F., Evaluation of the cross-section for elastic scattering of ^{4}He from carbon, Nucl. Instr. Meth. B161–163 (2000) 125.

[2] BOGDANOVIĆ RADOVIĆ, I., JAKŠIĆ. M., BENKA, O., GURBICH, A.F., Helium elastic scattering from carbon for 30º to 150º in the energy region from 2 to 4.8 MeV, Nucl. Instr. Meth. B190 (2002) 100.

CONCENTRATION PROFILES OF LIGHT ELEMENTS BY ELASTIC RECOIL DETECTION

Lu Xiuqin, Fu Changbo, Guo Jiyu, Zhao Kui
China Institute of Atomic Energy, Department of Nuclear Physics, China

Abstract

An Elastic Recoil Detection Analysis (ERDA) system using a ΔE-E telescope, position sensitive detection and Q3D magnetic spectrometer has been developed for the determination of light elements in semiconductor materials. This instrument is a new analytical tool for China. It has been successfully applied to characterize SiNH and SiC:H thin films.

1. INTRODUCTION

Concentration depth profiles of the components and contaminations of H, C and O are important in the development of various semiconductor materials. Normally the peaks of C, N, and O cannot be separated from the background of heavy elements by Rutherford back-scattering (RBS) measurements. ERDA from heavy ions as projectiles directly measures the recoil elements themselves. Therefore it enables to measure the individual elemental spectra with high sensitivity, good depth resolution, and simultaneous multi-element profiling by using element identification technique. The scope of this project was to develop ERDA technique with ΔE-E telescope and position sensitive detection, which have never been used for materials analysis in our country, and use this technique in the analysis of new foil materials.

In this project we developed a HI-ERDA technique with Q3D momentum analysis and ΔE-E particle identification in the CIAE laboratory (China Institute of Atomic Energy). Two ΔE(gas)-E telescopes were built for the specific requirements of this technique. A position sensitive detector is included in one of the telescopes as its residual energy detector, which has the ability to correct kinematics energy broadening. Measurements were performed for concentration depth profiles of H, C, N, O, Si, etc. in samples from our own and other laboratories. About 2 nm of H contamination on the surface was separated from the interior H contents in foils by the Q3D magnetic spectrometer and the following focal plane detector. Components and contaminants of H and other elements in the foils were simultaneous determined by the ΔE(gas)-E(PSD) telescope.

2. EXPERIMENTAL METHOD

The experimental configuration of the first measurement is shown schematically in Fig. 1.

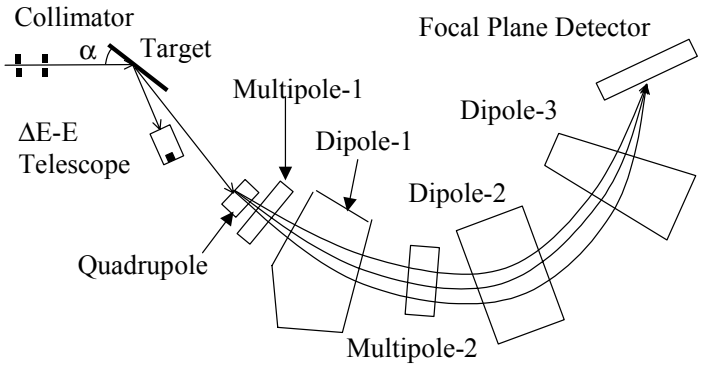

Figure 1. Schematic diagram of the experimental arrangement for the first measurement.

A heavy ion beam 100 MeV ^{127}I provided by the HI-13 tandem accelerator of CIAE bombards the target materials. The beam was collimated to a rectangle of 1mm × 4mm incident at 10° with respect to the surface of the target. The elastic recoil ions from the target were simultaneously measured by two detector systems. The recoiled H ions were analyzed by the Beijing Q3D magnetic spectrometer (G120L) at 15° with respect to the beam direction and detected by the following gas filled focal plane detector, which consists of a position sensitive counter. The position sensitive wire of the counter, which is located along the focal plane of the spectrometer, supplying position information, gives the energy spectrum of H with high resolution. The magnetic field setting allowed only H ions to enter the detector. The recoils were also detected at 35° with respect to the beam direction by a ΔE(gas)-E(solid) telescope, which consists of a thin gas detector for energy loss and a Au-Si surface barrier detector for residual energy measurement. The ΔE-E particle identification enables us to get individual elemental spectra.

In the second measurement, a single ΔE(gas)-E(Position Sensitive Detector) telescope, developed for the specific requirements of this technique, was used instead of the two sets of detector system in the first measurement. The detector was positioned at a scattering angle of 30°. The incident energy of the ^{127}I beam was 140 MeV. The beam was incident at 15° with respect to the surface of the target. The position information of the PSD provides kinematics correction to the energy spectra. The energy resolution was improved. Hydrogen and other heavy elements were simultaneously measured by respective constructing the coincidence and non-coincidence spectra of Er and ΔE from the single telescope.

Energy calibrations were performed at 140, 115, 90, 65 and 40 MeV of the ^{127}I beam bombarding $C_3H_6N_6$ and SiO_2 targets with the same detection geometry. The data were recorded by a Micro-VAX on-line data acquisition system. The spectra were reconstructed after the experiment for getting the individual spectrum of each element. The measured spectra were evaluated using the SIMNRA ion beam analysis code for obtaining the components. The target samples we have measured are listed in Table 1.

Table 1. Target samples we have measured

Samples	Made by
C/LiF multilayer fiols	Our target making group
Al/CHN multilayer fiols	Our target making group
$Si_xN_yH_z$/Si (6 pieces)	P. Pelicon, Slovenia
SiC:H/glass (4 pieces)	I. B. Radovic, Croatia
^{16}O (reference) (1 pieces)	I. C. Vickridge, France
Organic film (2pieces)	Beijing Institute of Graphic Communication
Diamond-like foil (5 pieces)	Peking University
GaN (3 pieces)	Tsinghua University
Superconductor foil (2 pieces)	Institute of Physics, China Academy of Sciences

3. RESULTS

The hydrogen spectrum of SiNH(D) film measured by the Q3D spectrometer and the following focal plane detector is shown in Fig. 2. Hydrogen contamination of 12×10^{15} at/cm^2 (~ 2.5 nm) at the surface was well separated from the bulk H. This expresses a level of nanometer depth resolution of the Q3D spectrometer system. The beam energy of 100 MeV was not high enough to profile through the full depth of the films.

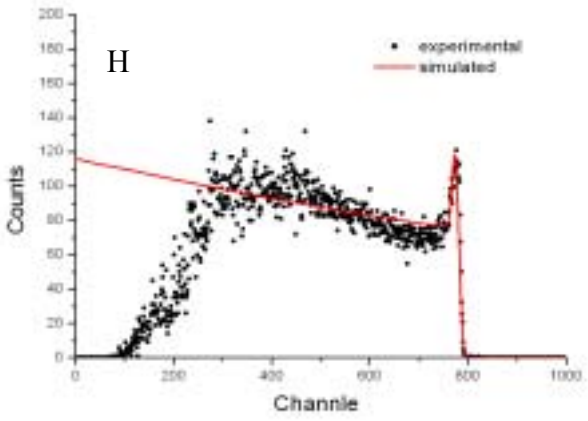

Figure 2. Hydrogen spectrum of SiNH(D) film measured by the Q3D spectrometer system.

Spectra of H, N, C, Si, and the contaminants for SiNH(D) and SiC:H films measured by the ΔE(gas)-E(PSD) telescope are given in Fig. 3 and Fig. 4 respectively. The results obtained from the simulation with the SIMNRA code for these samples are given in Table 2 and Table 3. The thickness determined for the ^{16}O reference film is about 30% higher than the nominal values provided. This may be due to the stopping powers for heavy ions being not well known. To normalize our data against the reference values, the values of the thickness in the tables should be lowered by 10 – 30%.

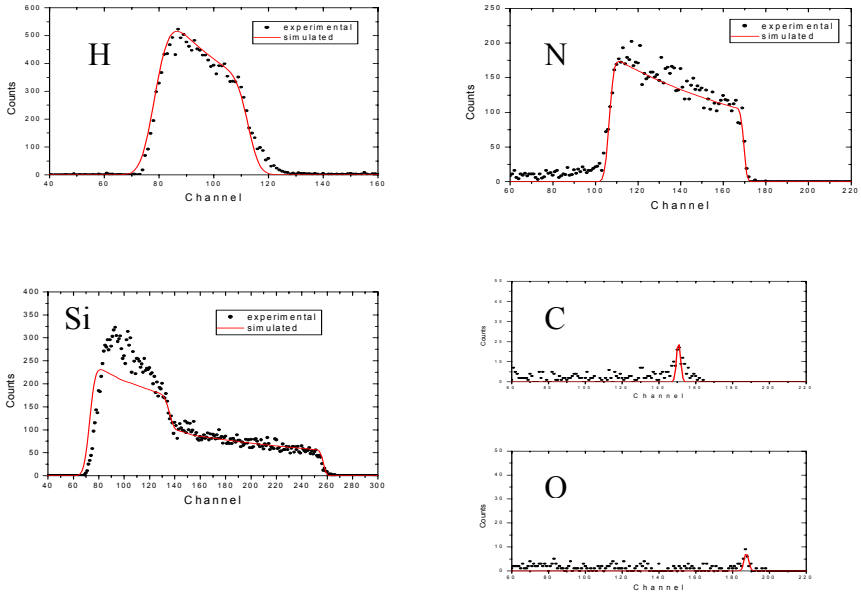

Figure 3. Spectra of H, N, Si and C, O contaminants in $Si_xN_yH_z$ (D) foil measured by ΔE(gas)-E(PSD) detector.

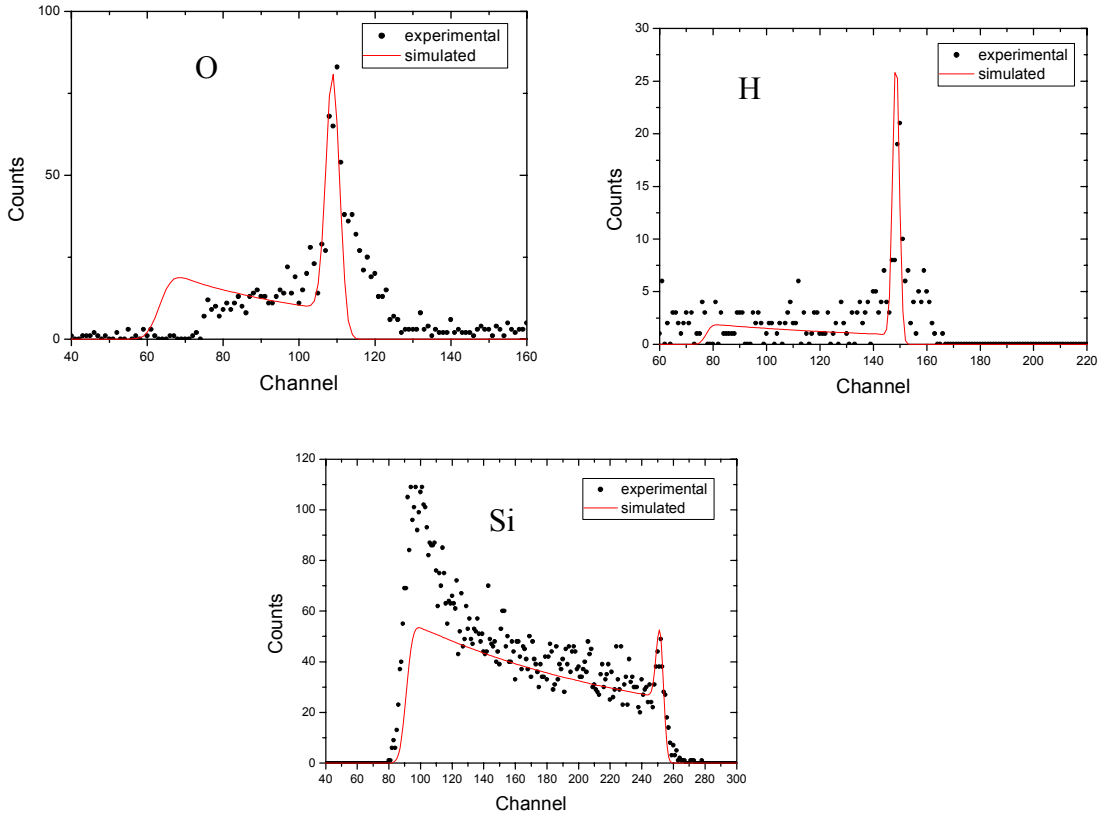

Figure 4. Spectra of H.C, and Si in SiC:H film measured by ΔE(gas)-E(PSD) detector.

Table 2. Components and contaminations for $Si_xN_yH_z$ films

Samples	Layer	Thickness $\times 10^{15}$ at./cm^2	Components			Contaminants		
			Si	N	H	O	C	H
A	1	30				0.3	0.3	0.4
	2	5800	0.38	0.40	0.22			
	3	600	0.40	0.45	0.15			
B	1	60				0.4	0.4	0.2
	2	5800	0.40	0.40	0.20			
	3	800	0.45	0.45	0.10			
	4	600	0.60	0.30	0.10			
C	1	40				0.3	0.4	0.3
	2	5800	0.38	0.40	0.22			
	3	600	0.40	0.45	0.15			
D	1	40				0.2	0.5	0.3
	2	5000	0.35	0.41	0.24			
	3	600	0.40	0.45	0.15			
E	1	40				0.2	0.4	0.4
	2	4900	0.35	0.42	0.23			
	3	500	0.40	0.45	0.15			
F	1	40				0.2	0.4	0.4
	2	6400	0.35	0.43	0.22			
	3	4300	?	0.45	?			

Table 3. Components and contaminations for $Si_xN_yH_z$ films

Samples	Thickness $\times 10^{15}$ at./cm^2	Components			Contaminants
		Si	H	C	O
1	200	0.55	0.25	0.2	
2	2300	0.80	0.14	0.02	0.04
3	200	0.58	0.27	0.15	
4	2100	0.83	0.13	0.02	0.02

4. CONCLUSIONS

The technique of simultaneously measuring the profiles of light elements by HI-ERDA has been established at the HI-13 tandem accelerator at CIAE. Using the Q3D magnetic spectrometer system, multi-element quantitative analysis with depth resolutions of a few nanometers have been demonstrated. The ΔE-E telescope with position-sensitive detection enables kinematical corrections to be applied to the data, producing much improved depth resolution.

The components and the contaminants of SiNH, SiC:H and other films have been determined. About a 10 – 30% correction may need in the measured thickness because of uncertainties in the stopping powers for heavy ions. We need to do more work on stopping power and depth calibration.

APPENDIX

^{16}O THIN FILM REFERENCE MATERIALS FOR NUCLEAR REACTION ANALYSIS

I. Vickridge
Groupe de Physique des Solides, Université de Paris, France

G. Battistig
Research Institute for Technical Physics and Materials Science, Department of Ion Beam Analysis, Hungary

Thin film Ta_2O_5 samples were distributed to CRP participants for use in the round-robin exercise. This appendix describes how these samples were prepared and characterized.

Preparation was made using anodic oxidation of tantalum using an electrolyte solution of 4% ammonium citrate prepared with water of natural ^{16}O isotopic composition. A constant anodising current of 4 mA/cm^2 was maintained until the desired electrolysis voltage was reached, then stopped immediately. The areal density of ^{16}O in these thin Ta_2O_5 films was determined by NRA using the method described in [1] and comparing the data with that from a primary anodic Ta_2O_5 standard kindly made available to us by Dr C. Ortega of GPS, Paris. The $^{16}O(d,p_1)^{14}N$ reaction at 850 keV was used with the protons detected with a 300 mm^2 silicon detector located at an angle of 150°. A 12 μm Mylar™ foil covered the detector. Detector count rates were kept sufficiently low so that deadtime corrections are negligible.

There are various sources of uncertainty which when compounded, produce the final uncertainty in the ^{16}O areal density of the thin film samples. The major sources of uncertainty are:

1. The primary reference standard is estimated to have an absolute value that is within ± 3% of the true value.
2. There is a small low energy tail on the p_1 peak in the NRA spectrum, most likely due to oxygen dissolved in the bulk tantalum. The counts in this tailing are less than 2% of the gross counts recorded in the spectrum peak, and similar in magnitude from sample to sample. We assign a systematic error of 0.5% to the background correction for all samples. There is negligible change in the total sample uncertainty when this systematic error is added in quadrature to the uncertainty of the primary reference standard.
3. The reproducibility of peak areas from several measurements was better than 1%. This indicates that sample homogeneity and current integration were both sufficiently good that their contributions to the total uncertainty are negligible.

The random errors due to counting statistics and the error common to all of the samples are quoted separately. This means that comparisons between samples from the same series should agree within the random error, and comparisons between these samples and others not derived from the primary reference standard should agree within the common and random errors, added together in quadrature.

[1] AMSEL, G., NADAI, J.P., ORTEGA, C., RIGO, S., SIEJKA, J., Precision absolute thin film standard reference targets for nuclear reaction microanalysis of oxygen isotopes, Nucl. Instr. Meth 149 (1978) 705.

PUBLICATIONS ARISING FROM THIS CRP

ANDRADE E., CHROMIK S., JERGEL MI, JERGEL MA, FALCONY C., STRIBK V., ZAVALA E.P., ROCHA M.F., Study of the Superconducting MgB_2 Films by Ion Beam Analysis Methods, Thin Solid films, 433 (2003) 103.

ARAUJO, L.L., GRANDE, P.L., BEHAR, M., DIAS, J.F., DOS SANTOS, J.H.R., SCHIEWITZ, G., Channelling loss of O ions in Si: the Barkas effect, Nucl. Instr. Meth. B193 (2002) 172.

AZEVEDO, G.M., BEHAR, M., DIAS, J.F., GRANDE P.L., da SILVA, D.L., Random and channelling stopping powers of He and Li ions in Si, Phys. Rev. B65 (2002) 75203.

BARRADAS, N.P., Advanced data analysis techniques for Ion Beam Analysis, Surface and Interface Analysis 35 (2003) 760.

BARRADAS, N.P., da SILVA, M.F., SOARES, J.C., KREISSIG, U., CARDOSO, S., FREITAS, P.P., High resolution IBA analysis of spin dependent tunnel junctions, Modern Phys. Lett. B15 (2001) 1288.

BARRADAS, N.P., JEYNES, C., WEBB, R.P., WENDLER, E., Accurate determination of the stopping power of ^{4}He in Si using Bayesian inference, Nucl. Instr. Meth. B194 (2002) 15.

BATTISTIG, G., GARCIA LOPEZ, F.J., KHANH, N.Q., MORILLA, Y., RESPALDIZA, M.A., SZILAGYI, E., High sensitivity ion beam analytical method for studying ion implanted SiC, Materials Science Forum 433–436 (2003) 625.

BATTISTIG, G., GARCIA LOPEZ, J., MORILLA, Y., KHANH, N.Q., LOHNER, T., PETRIK, P., RAMOS, A.R., Effect of ion current density on damage in Al ion implanted SiC, Nucl. Inst. Meth. B219 (2004) 652.

BEHAR, M., DIAS, J.F., GRANDE, P.L., dos SANTOS, J.H.R., Electronic energy loss of H_3^+ ion clusters in SiO_2 films, Phys. Rev. A64 (2001) 022904.

BOGDANOVIĆ RADOVIĆ, I., BENKA, O., Determination of H recoil cross-sections for He ions incident at 2.5 – 4.5 MeV and recoil angles from 30° to 60°, Nucl. Instr. Meth. B174 (2001) 25.

BOGDANOVIĆ RADOVIĆ, I., JAKSIC, M., BENKA, O., GURBICH, A.F., Helium elastic scattering from carbon for 30º to 150º in the energy region from 2 to 4.8 MeV, Nucl. Instr. Meth. B190 (2002) 100.

ČADEŽ, I., ČERČEK, M., PELICON, P., RAZPET, A., Neutral molecules in tokamak edge plasma — role of vibrationally excited hydrogen molecules, Proceedings of the International Conference Nuclear Energy in Central Europe 2003, September 8-11 2003, Portorož, Slovenia.

DE SOUZA, J.P., BEHAR, M., DIAS J.F., DOS SANTOS, J.H.R, Range parameters of ^{18}O implanted into Si and SiO_2, Nucl. Instr. Meth. B175 (2001) 46.

DOS SANTOS, J.H.R., GRANDE, P.L., BEHAR, M., DIAS, J.F., ARISTA, N.R., ECKAR, J.C., LANTSCHNER, G.H., Experimental energy straggling of protons in SiO_2, Phys.Rev. A68 (2003) 042903

FLORES M., MUHL S., ANDRADE E., The Relation Between Plasma Characteristic and the Corrosion Properties of TiN/Ti Multilayers Deposited by Unbalanced Magnetron Sputtering, Thin Solid Films 433 (2003) 217.

FLORES, M., MUHL S., ANDRADE, E., The relation between the plasma characteristic and the corrosion properties of TiN/Ti multilayers deposited by unbalanced magnetron sputtering, Thin Solid Films 433 (2003) 217.

GRACIN, D., JAKSIC, M., DUBCEK, P., MEDUNIC, Z., Investigation of the nano-structural properties of amorphous SiC alloys by IBA technique, optical spectroscopy and GISAXS, Vacuum 71 (2003) 47.

JAKSIC, M., BOSNJAK, Z., GRACIN, D., MEDUNIC, Z., PASTUOVIC, Z., VITTONE, E., NAVA, F., Characterisation of SiC by IBIC and other IBA techniques, Nucl. Instr. Meth. B188 (2002) 130.

JERGEL MI, ANDRADE E**,** CHROMIK S, JERGEL MA, FALCONY C, STRIBIK S, ROCHA M.F., ZAVALA E.P., Composition Depth Profiles of Superconducting MgB_2 Thin Films Determined by Ion Beam Analysis Methods, Physica C383 (2003) 287.

KENNEDY, V.J., JOHNSON, P.B., MARKWITZ, A., VAROY, C.R., SHORT, K.T., Microprobe analysis of light elements in nanoporous surfaces produced by He ion implantation, Nucl. Instr. Meth. B210 (2003) 543.

LU XIUQUIN, et al, Elastic recoil detection with high resolution, Chinese Journal of Physics Vol. 30, 6 (2001) 368.

MARKWITZ, A., DYTLEWSKI, N., KENNEDY, V.J., PELICON P., VICKRIDGE, I.C., Use of heavy ion time of flight elastic recoil detection for depth profiling of light elements, Nuclear Techniques of Analysis Conference, Sydney, Australia, November 2003.

MATIAS, V., ÖHL, G., SOARES, J.C., BARRADAS, N.P., VIEIRA, A., CARDOSO, S., FREITAS, P.P., Determination of the composition of light thin films with artificial neural network analysis of Rutherford backscattering analysis, Phys. Rev. E67 (2003) 046705.

MEDUNIC, Z., GRACIN, D., BOGDANOVIĆ RADOVIĆ, I., JAKSIC, M., Characterisation of amorphous silicon solar cells by IBA methods, Nucl. Instr. Meth. B190 (2002) 611.

ÖHL, G., MATIAS, V., VIEIRA, A., N. BARRADAS, N.P., Artificial neural network analysis of RBS data with roughness: Application to $Ti_{0.4}Al_{0.6}N$/Mo multilayers, Nucl. Instr. Meth. B211 (2003) 265.

PASCUAL-IZARRA, C., BIANCONI, M., BARRADAS, N.P., CLIMENT-FONT, A., GARCIA, G., GONZALO, J., AFONSO, C.N., Continuous stopping power curves of Al_2O_3 for 0.2-0.5 MeV He ions, Nucl. Instr. Meth B219. (2004) 232.

RAZPET, A., PELICON, P., RUPNIK, Z., BUDNAR, Development of a time-of-flight telescope for ERDA at Josef Stefan Institute, Nucl. Instr. Meth. B201 (2003) 535.

VICKRIDGE, I.C., TROMSON, D., TRIMAILLA, I., GANEM, J.J., SZILAGYI, E., BATTISTIG, G., Oxygen isotopic exchange occurring during dry oxidation of 6H-SiC, Nucl. Inst. Meth. B190 (2002) 574.

VIEIRA, A., BARRADAS, N.P., A training algorithm for classification of high dimensional data, Neurocomputing 50 (2003) 461.

WEI, P., BARRADAS, N.P., SOARES, J.C., da SILVA, M.F., KREISSIG, U., CARDOSO, S., FREITAS, P.P., Composition analysis of the insulating barrier in magnetic tunnel junctions by high resolution RBS, Nucl. Instr. Meth. B190 (2002) 684.

ABBREVIATIONS

AES	Auger Emission Spectrometry
AFM	Atomic Force Microscopy
CVD	Chemical Vapour Deposition
ERDA	Elastic Recoil Detection Analysis
FS	Forward Scattering
FTIR	Fourier Transform Infrared Spectrometry
FWHM	Full Width at Half Maximum
HI-ERDA	Heavy Ion Elastic Recoil Detection Analysis
HI-RBS	Heavy Ion Rutherford Backscattering
IBA	Ion Beam Analysis
IEE	Ion Induced Electron Emission
LEIS	Low Energy Ion Scattering
MEIS	Medium Energy Ion Scattering
NRA	Nuclear Reaction Analysis
PECVD	Plasma Enhanced Chemical Vapour Deposition
PIGE	Particle Induced Gamma ray Emission
PIPS	Passivated Implanted Planar Silicon
PIXE	Particle Induced X ray Emission
PI^3	Plasma Immersion Ion Implantation
PSD	Position Sensitive Detector
PVD	Physical Vapour Deposition
RBS	Rutherford Backscattering
RBX	Ion Beam Analysis Software Package (www.kfki.hu/~ionhp/doc/prog/mdepth.htm)
RUMP	Ion Beam Analysis Software Package (www.genplot.com)
sccm	Standard Cubic Centimeters Per Minute

SIMNRA	Ion Beam Analysis Software Package (www.rzg.mpg.de/~mam/)
SIMOX	Separation by Implantation of Oxygen
SIMS	Secondary Ion Mass Spectrometry
SRIM	Software Package for Stopping and Range of Ions in Matter (www.srim.org)
SRIM2000	Software Package For Stopping and Range of Ions in Matter (www.srim.org)
SRIM2003	Software Package for Stopping and Range of Ions in Matter (www.srim.org)
TOF	Time of Flight
TRIM	Software Package for Stopping and Range of Ions in Matter (www.srim.org)
UHV	Ultra High Vacuum
WINDF	Ion Beam Analysis Software Package (www.ee.surrey.ac.uk/SCRIBA/ibc/ndf/)
XPS	X ray Photoelectron Spectrometry
XRD	X ray Diffraction
XRF	X ray Fluorescence
ZBL	ZIEGLER, J.F., BIERSACK, J.P., LITTMARK, U. (www.srim.org)
ΔE-E	Differential Energy-Residual Energy

LIST OF PARTICIPANTS

Andrade, E.I.
Universidad Nacional Autonoma de Mexico,
Instituto de Fisica,
Apartdo Postal 20-364,
Mexico, D.F. C.P. 01000, Mexico
Email: Andrade@fisica.unam.mx

Barradas, N.P.
Instituto Technológico e Nuclear,
Estrada Nacional 10, Apartado 21,
P-2686-953 Sacavém, Portugal
Email: nononi@itn.pt

Battistig, G.
Research Institute for Technical Physics and Materials Science,
Department of Ion Beam Analysis,
P.O. Box 49,
H-1525 Budapest, Hungary
Email: battisti@mfa.kfki.hu

Behar, M.
Universidade Federal do Rio Grande do Sul,
Instituto de Fisica,
Laboratory de Implantacao Ionica,
Av. Bento Gonçalves, 9500,
Caixa Postal 15051, Porto Alegre, Brazil
Email: behar@if.ufrgs.br

Dias, J.F.
Universidade Federal do Rio Grande do Sul,
Instituto de Fisica,
Laboratory de Implantacao Ionica,
Av. Bento Gonçalves, 9500,
Caixa Postal 15051, Porto Alegre, Brazil
Email: jfdias@if.ufrgs.br

Dytlewski, N.
Physics Section, Division of Physical and Chemical Sciences,
International Atomic Energy Agency,
Wagramer Strasse 5, P.O. Box 100,
A-1400 Vienna, Austria
Email: N.Dytlewski@iaea.org

Fazinic, S.
Physics Section, Division of Physical and Chemical Sciences,
International Atomic Energy Agency,
Wagramer Strasse 5, P.O. Box 100,
A-1400 Vienna, Austria
Email: S.Fazinic@iaea.org

Lu, X.
China Institute of Atomic Energy,
P.O. Box 275-10,
Beijing 102413, China
Email: xqlu@iris.ciae.ac.cn

Markwitz, A.
Institute of Geological and Nuclear Sciences,
P.O. Box 313-12,
Lower Hutt, New Zealand
Email: a.markwitz@gns.cri.nz

Pelicon, P.
Institut 'Jožef Stefan',
Jamova 39, P.O. Box 3000,
SI-1001 Ljubljana, Slovenia
Email: primoz.pelicon@ijs.si

Radović, I.B.
Ruđer Bošković Institute,
Bijenička 54,
P.O. Box 180,
10002 Zagreb, Croatia
Email: iva@rudjer.irb.hr

Rauhala, E.
University of Helsinki,
Accelerator Laboratory,
P.O. Box 43,
FIN-00014, Finland
Email: eero.rauhala@helsinki.fi

Vickridge, I.
Groupe de Physique des Solides,
UMR 7588 du CNRS, Université de Paris 6 et 7,
Tour 23, 2 Place Jussieu,
75251 Paris, France
Email: vickridge@gps.jussieu.fr